

AD-A281 384

1

**PRETEST PREDICTIONS OF LONG-ROD
INTERACTIONS WITH ARMOR
TECHNOLOGY TARGETS**

Charles E. Anderson, Jr.
David L. Littlefield

DTIC
ELECTE
JUL 12 1994
S F D

**TECHNICAL REPORT
SwRI Project No. 07-5117**

Prepared for

U.S. Army Research Office
P.O. Box 12211
Research Triangle Park, NC 27709-2211

This document has been approved
for public release and sale; its
distribution is unlimited.

April 1994

"Original contains color
plates: All DTIC reproductions
will be in black and
white."

10308 94-21152



SOUTHWEST RESEARCH INSTITUTE
SAN ANTONIO
DETROIT

HOUSTON
WASHINGTON, DC

94 7 11 164

REPORT DOCUMENTATION PAGE

Form Approved
OMB No. 0704-0188

Public reporting burden for this collection of information is estimated to average 1 hour per response, including the time for reviewing instructions, searching existing data sources, gathering and maintaining the data needed, and completing and reviewing the collection of information. Send comments regarding this burden estimate or any other aspect of this collection of information, including suggestions for reducing this burden, to Washington Headquarters Services, Directorate for Information Operations and Reports, 1215 Jefferson Davis Highway, Suite 1204, Arlington, VA 22202-4302, and to the Office of Management and Budget, Paperwork Reduction Project (0704-0188) Washington, DC 20503.

1. AGENCY USE ONLY (Leave blank)	2. REPORT DATE	3. REPORT TYPE AND DATES COVERED	
	April 1994	Technical Report 11/92 - 4/94	
4. TITLE AND SUBTITLE		5. FUNDING NUMBERS	
Pretest Predictions of Long-Rod Interactions with Armor Technology Targets		① AAL03-92-k-0001	
6. AUTHOR(S)		8. PERFORMING ORGANIZATION REPORT NUMBER	
Charles E. Anderson, Jr. DAvid L. Littlefield		SwRI Report 5117/001	
7. PERFORMING ORGANIZATION NAME(S) AND ADDRESS(ES)		9. SPONSORING/MONITORING AGENCY NAME(S) AND ADDRESS(ES)	
Southwest Research Institute Structural Systems and Technology Division P.O. Drawer 28510 San Antonio, TX 78228-0510		U.S. Army Research Office P.O. Box 12211 Research Triangle Park, NC 27709-2211	
10. SPONSORING/MONITORING AGENCY REPORT NUMBER		11. SUPPLEMENTARY NOTES	
ARO 29788.7-M5		The view, opinions and/or findings contained in this report are those of the author(s) and should not be construed as an official Department of the Army position, policy, or decision, unless so designated by other documentation.	
12a. DISTRIBUTION/AVAILABILITY STATEMENT		12b. DISTRIBUTION CODE	
Approved for public release; distribution unlimited.			
13. ABSTRACT (Maximum 200 words)			
<p>The results from pretest predictions for penetration experiments of tungsten alloy projectiles into three generic target types have been documented. Predictions were made using two analytical models (the Walker-Anderson model and the MITI model) and with numerical simulation (using the wave propagation computer code CTH). The targets—a finite-thick RHA target; oblique, high-hard steel, spaced-plate target; and a ceramic laminate target—were purposely designed to be defeated, and penetration of the residual projectile into an RHA witness pack was designated as the metric for comparison. The purpose of this study can be regarded as twofold. First, a pretest prediction of any experiment is always desirable. For these targets, the predictions provide an estimate of the residual projectile length and velocity, as well as the resulting penetration of the residual rod into an RHA witness pack. Furthermore, specific details of the experiment can more readily be analyzed with modeling; for example, some quantities cannot easily be measured in an experiment, such as penetration velocity or projectile erosion rate. Second, a subsequent comparison of these predictions to the actual experimental outcomes provides a quantitative measure of the state-of-the-art predictive capability for these generic target types using hydrocodes and analytical models. Analysis of discrepancies then suggests the most prudent areas for improvement in both the analytical and numerical models.</p>			
14. SUBJECT TERMS		15. NUMBER OF PAGES	
armor technology target, RHA, spaced-plate target, ceramic laminate target, CTH, Walker-Anderson model, long-rod penetration, hypervelocity impact, penetration mechanics, witness pack		112	
16. PRICE CODE			
17. SECURITY CLASSIFICATION OF REPORT	18. SECURITY CLASSIFICATION OF THIS PAGE	19. SECURITY CLASSIFICATION OF ABSTRACT	20. LIMITATION OF ABSTRACT
UNCLASSIFIED	UNCLASSIFIED	UNCLASSIFIED	UL

Table of Contents

1.0 INTRODUCTION	1
2.0 ANALYSIS APPROACH	5
2.1 Introduction	5
2.2 Constitutive Treatment	5
2.3 Treatment of Target Breakout	6
2.3.1 Numerical Modeling	6
2.3.2 Analytic Modeling	7
2.4 Baseline Response	9
3.0 FINITE-THICKNESS RHA TARGET	13
3.1 Target Description	13
3.2 Numerical Simulations	13
3.3 Analytical Predictions	22
3.4 Experimental Results and Summary	22
4.0 PENETRATION OF SHORT <i>L/D</i> PROJECTILES	27
4.1 Introduction	27
4.2 Nondimensionalized Semi-Infinite Penetration	27
4.3 Analysis	33
4.4 Summary	34
5.0 HIGH-HARD STEEL SPACED-PLATE TARGET	37
5.1 Target Description	37
5.2 Numerical Simulations	37
5.3 Analytical Predictions	57
5.4 Corrections to the 3-D Computations	59
5.5 Experimental Results and Summary	61
6.0 CERAMIC LAMINATE TARGET	65
6.1 Target Description	65
6.2 Ceramic Model	65
6.3 Parametric Studies with Ceramic Model	67
6.3.1 Depth-of-Penetration Tests: CTH	68
6.3.2 PHERMEX Experiments: CTH	71
6.3.3 Calibration of the Walker-Anderson Model	72
6.4 Numerical Simulations	73

Table of Contents (Cont'd)

6.5 Analytical Predictions	76
6.6 Experimental Results and Summary	81
7.0 CERAMIC LAMINATE TARGET REVISITED	85
7.1 Further Analytical Modeling	85
7.1.1 Summary of Main Features of Walker-Anderson Model	85
7.1.2 Modifications of the Model for Ceramics	86
7.1.3 Determination of α	87
7.2 Parametric Studies with Ceramic Model	88
7.3 Analytical Predictions	88
7.4 Experimental Results and Summary	91
8.0 SUMMARY AND CONCLUSIONS	93
9.0 ACKNOWLEDGEMENTS	95
10.0 REFERENCES	97

Accession For	
NTIS	CRA&I
DTIC	LAB
Unannounced	
Justification	
By	
Distribution /	
Availability Codes	
Dist	Avail and/or Special
A-1	

List of Figures

Figure 1.	Normalized depth of penetration versus impact velocity	2
Figure 2.	Depth of penetration for constant energy long-rod projectiles	3
Figure 3.	Schematic of experimental arrangement	4
Figure 4.	Variation of α with x/T	9
Figure 5.	RHA target and witness pack dimensions	13
Figure 6.	Penetration and tail velocities versus time, RHA target—CTH results	14
Figure 7.	Penetration and tail velocities versus depth of penetration, RHA target—CTH results	14
Figure 8.	Pressure versus position, RHA target—CTH results	16
Figure 9.	Nose and tail positions versus time, RHA target—CTH results	16
Figure 10.	Material interface plots of perforation of the RHA target, $V_p = 1.775$ km/s: a.) Near breakout ($t = 540$ μ s) b.) After perforation ($t = 560$ μ s)	18
Figure 11.	Material interface plots of perforation of the RHA target, $V_p = 2.600$ km/s: a.) Near breakout ($t = 320$ μ s) b.) After perforation ($t = 340$ μ s)	19
Figure 12.	Normalized length of the projectiles versus depth of penetration, RHA target—CTH results	20
Figure 13.	Material interface plots of final crater in witness pack: a.) $V_p = 1.775$ km/s b.) $V_p = 2.600$ km/s	21
Figure 14.	Nose and tail position versus time, RHA target—Walker-Anderson results	23
Figure 15.	Projectile lengths versus depth of penetration, RHA target—Walker-Anderson results	23
Figure 16.	Normalized length of the projectiles versus depth of penetration, RHA target—Walker-Anderson results	24
Figure 17.	Schematic of experimental arrangement without witness pack	25
Figure 18.	P/L for $L/D = 1$ rods versus impact velocity	28
Figure 19.	P/L for $L/D = 3$ rods versus impact velocity	28
Figure 20.	P/L for $L/D = 5$ and 6 rods versus impact velocity	29
Figure 21.	$P\alpha/L$ for $L/D = 1$ rods versus impact velocity	29

List of Figures (Cont'd)

Figure 22.	$P\alpha/L$ for $L/D = 1$ rods versus $\pi_1^{1/3}$	31
Figure 23.	$P\alpha/L$ for $L/D = 1$ rods versus $\pi_1^{1/3} \pi_2^{-0.15}$	31
Figure 24.	$P\alpha/L$ for $L/D = 3$ rods versus $\pi_1^{1/3} \pi_2^{-0.15}$	32
Figure 25.	$P\alpha/L$ for $L/D = 5 \& 6$ rods versus $\pi_1^{1/3} \pi_2^{-0.15}$	32
Figure 26.	Comparison of computations and experiments with regression analyses	35
Figure 27.	Schematic of the high-hard spaced-plate target array	37
Figure 28.	Nose and tail positions versus time, spaced-plate target—CTH results	39
Figure 29.	Centerline penetration pressure versus penetration position, spaced-plate target—CTH results (solid line represents the 2.600-km/s impact; dashed line represents the 1.775-km/s impact)	39
Figure 30.	Nose (penetration) and tail velocities versus penetration position, spaced-plate target, $V_p = 1.775$ km/s—CTH results	40
Figure 31.	Nose (penetration) and tail velocities versus penetration position, spaced-plate target, $V_p = 2.600$ km/s—CTH results	40
Figure 32.	Nose (penetration) and tail velocities versus time, spaced-plate target, $V_p = 1.775$ km/s—CTH results	41
Figure 33.	Material boundaries and pressure contours, spaced-plate target: $V_p = 1.775$ km/s	42
	a) $t = 100 \mu s$	42
	b) $t = 200 \mu s$	42
	c) $t = 300 \mu s$	43
	d) $t = 400 \mu s$	43
	e) $t = 500 \mu s$	43
	f) $t = 562 \mu s$	43
	g) $t = 600 \mu s$	43
	h) $t = 700 \mu s$	43
Figure 34.	Nose (penetration) and tail velocities versus time, spaced-plate target, $V_p = 2.600$ km/s—CTH results	44
Figure 35.	Material boundaries and pressure contours, spaced-plate target: $V_p = 2.600$ km/s	44
	a) $t = 20 \mu s$	45
	b) $t = 100 \mu s$	45
	c) $t = 200 \mu s$	45
	d) $t = 300 \mu s$	45
	e) $t = 400 \mu s$	45
	f) $t = 474 \mu s$	45

List of Figures (Cont'd)

Figure 36.	3-D views of projectile-target interaction: $V_p = 1.775$ km/s	46
a)	$t = 0 \mu\text{s}$	46
b)	$t = 200 \mu\text{s}$	47
c)	$t = 400 \mu\text{s}$	47
d)	$t = 561 \mu\text{s}$	48
e)	$t = 561 \mu\text{s}$ (enlarged view)	49
f)	$t = 742 \mu\text{s}$	50
		51
Figure 37.	3-D views of projectile-target interaction: $V_p = 2.600$ km/s	52
a)	$t = 200 \mu\text{s}$	52
b)	$t = 400 \mu\text{s}$	53
c)	$t = 550 \mu\text{s}$	54
Figure 38.	XY-plane, $Z = 0$; and YZ-plane, $X = 0$, view of plates and witness pack, spaced-plate target, $V_p = 2.600$ km/s	55
Figure 39.	YZ-plane, various X 's, view of plates and witness pack, spaced-plate target, $V_p = 2.600$ km/s	56
Figure 40.	Normalized projectile length versus penetration position, spaced-plate target—CTH results	58
Figure 41.	Nose and tail positions versus time, spaced-plate target—Walker-Anderson results	60
Figure 42.	Normalized projectile length versus depth of penetration, spaced-plate target—Walker-Anderson results	60
Figure 43.	Schematic of ceramic laminate target	65
Figure 44a.	Pressure-dependent strength of ceramics—Johnson-Holmquist ceramics model	66
Figure 44b.	Maximum allowed plastic strain—Johnson-Holmquist ceramics model	66
Figure 44c.	ΔP increase in equation of state at failure—Johnson-Holmquist ceramics model	66
Figure 45.	Experimental arrangement for depth-of-penetration studies (from Woolsey, <i>et al.</i> [34-36])	69
Figure 46.	Summary of experimental and computational results for DOP tests	70
Figure 47.	Penetration velocity versus depth of penetration for CTH simulation of DOP tests, tile thickness = 2.0 cm	70
Figure 48.	Penetration velocity versus depth of penetration for CTH simulation of DOP tests, tile thickness = 4.0 cm	71

List of Figures (Cont'd)

Figure 49.	PHERMEX results, and CTH computations, for 99.5% Al_2O_3	72
Figure 50.	Comparison of the depth of penetration from the Walker-Anderson model for DOP experiments, tile thickness = 3.0 cm	74
Figure 51.	Parametric study for the effective flow stress in the Walker-Anderson model, PHERMEX experiments	74
Figure 52.	Time-dependent effective flow stress in the Walker-Anderson model, PHERMEX experiments	75
Figure 53.	Comparison of the Walker-Anderson model, effective flow stress of 1.2 GPa, with the PHERMEX experiments	75
Figure 54.	Nose and tail positions versus time, ceramic laminate target—CTH results	77
Figure 55.	Penetration and tail velocities versus depth of penetration, ceramic laminate target—CTH results	77
Figure 56.	Pressure versus position, ceramic laminate target—CTH results	78
Figure 57.	Normalized length of the projectiles versus depth of penetration, ceramic laminate target—CTH results	78
Figure 58.	Material interface plot at perforation of the ceramic laminate target, $V_p = 2.600 \text{ km/s}$	79
Figure 59.	Nose and tail positions versus time, ceramic laminate target—Walker-Anderson results using 2.4 GPa as the effective flow stress for the ceramic	79
Figure 60.	Normalized length of the projectiles versus depth of penetration, ceramic laminate target—Walker-Anderson results using 2.4 GPa as the effective flow stress for the ceramic	80
Figure 61.	Nose and tail positions versus time, ceramic laminate target—Walker-Anderson results using 1.2 GPa as the effective flow stress for the ceramic	80
Figure 62.	Normalized length of the projectiles versus depth of penetration, ceramic laminate target—Walker-Anderson results using 1.2 GPa as the effective flow stress for the ceramic	81
Figure 63.	Nose and tail positions versus time and comparison of the final depth of penetration with DOP tests for a 3.0-cm thick, 99.5 Al_2O_3 tile using the pressure-dependent yield function in the Walker-Anderson model	89
Figure 64.	Comparison of the Walker-Anderson model using the pressure-dependent yield function to PHERMEX data for a 99.5 Al_2O_3 ceramic target	89

List of Figures (Cont'd)

Figure 65.	Nose and tail positions versus time for $V_p = 1.775$ km/s, ceramic laminate target—Walker-Anderson model using the pressure-dependent yield function	90
Figure 66.	Nose and tail positions versus time for $V_p = 2.600$ km/s, ceramic laminate target—Walker-Anderson model using the pressure-dependent yield function	90

List of Tables

Table 1.	Projectile Dimensions	3
Table 2.	Constitutive Parameters	6
Table 3.	Baseline Penetration into Semi-Infinite RHA	10
Table 4.	Depths of Penetration into Witness Pack: RHA Target	24
Table 5.	Residual Length and Velocity After Perforation of RHA Target	26
Table 6.	Parameters for Regression Analysis for Penetration by Small <i>L/D</i> Projectiles	33
Table 7.	Summary of Computational Results for Small <i>L/D</i> Calculations	34
Table 8.	Depths of Penetration into Witness Pack: Spaced-Plate Target	62
Table 9.	Parameters for the Johnson-Holmquist Ceramics Model	67
Table 10.	Depths of Penetration into Witness Pack: Ceramic Laminate Target	82
Table 11.	Depths of Penetration into Witness Pack: Ceramic Laminate Target Revisited	91

1.0 INTRODUCTION

The issue of the penetration performance of super-ordnance velocity and hypervelocity projectiles is under investigation at the Institute for Advanced Technology at The University of Texas at Austin. As part of their program, a series of experiments were performed at Arnold Engineering Development Center (AEDC) to examine the penetration efficiency of five generic target types at two different impact velocities: one representative of an extension to current state-of-the-art gun systems (super-ordnance velocity), and the other at a velocity of a future but hypothetical gun system (hypervelocity). The desire was to perform the experiments using as large a scale size as possible; it was determined that the highest projectile energy that could be launched with reasonable success out of the two-stage light-gas gun at AEDC was approximately 2.9 MJ. For design purposes, the kinetic energy of the projectile was fixed at 2.88 MJ. This energy is approximately 42% of the launch kinetic energy of a full scale long-rod projectile. For the same impact velocity, the geometric dimensions of the projectile scale as the cube root of the kinetic energy, so the replica model projectile (and targets) are 75% of the full scale dimensions.

Constant kinetic energy, heavy tungsten alloy projectiles, with a length-to-diameter (L/D) ratio of 30, were selected for the experiments. Since the aspect ratio and kinetic energy (KE) are held constant, the diameter of the projectile for a given impact velocity V can be obtained from the relation $\frac{1}{2}MV^2 = KE$:

$$D = \left[\frac{8 KE}{\pi \rho_p V^2 (L/D)} \right]^{\frac{1}{3}}, \quad (1)$$

where it has been assumed that the projectile is a right circular cylinder, and ρ_p is the projectile density. The penetration performance, as measured by the depth of penetration P divided by the original length of the projectile L , is shown in Fig. 1 for $L/D = 20$ tungsten alloy projectiles into semi-infinite RHA. The experimental data are from various researchers, and are denoted by the symbols; and the solid curve is a least-squares regression fit of a hyperbolic equation through the data [1].¹ The depth of penetration can be written as:

$$P = f(V) L = f(V) \left(\frac{L}{D} \right) D, \quad (2)$$

where $f(V)$ denotes the velocity dependence of penetration, e.g., the regression fit to the experimental data. Substituting Eqn. (1) into Eqn. (2) for D provides an estimate of the depth of penetration as a function of the impact kinetic energy, impact velocity, and the aspect ratio of the projectile:

¹ The hyperbolic curve fit at the lower impact velocities lays above the experimental data, and indicates that Sorensen, *et al.*, used a different data set than those shown in Fig. 1 for the lower impact velocities. The dashed line represents a polynomial curve fit through the $L/D = 20$ -23 data over the entire velocity range. But the original curve of Sorensen, *et al.* [1], was used during the planning of the tests, and so is used here.

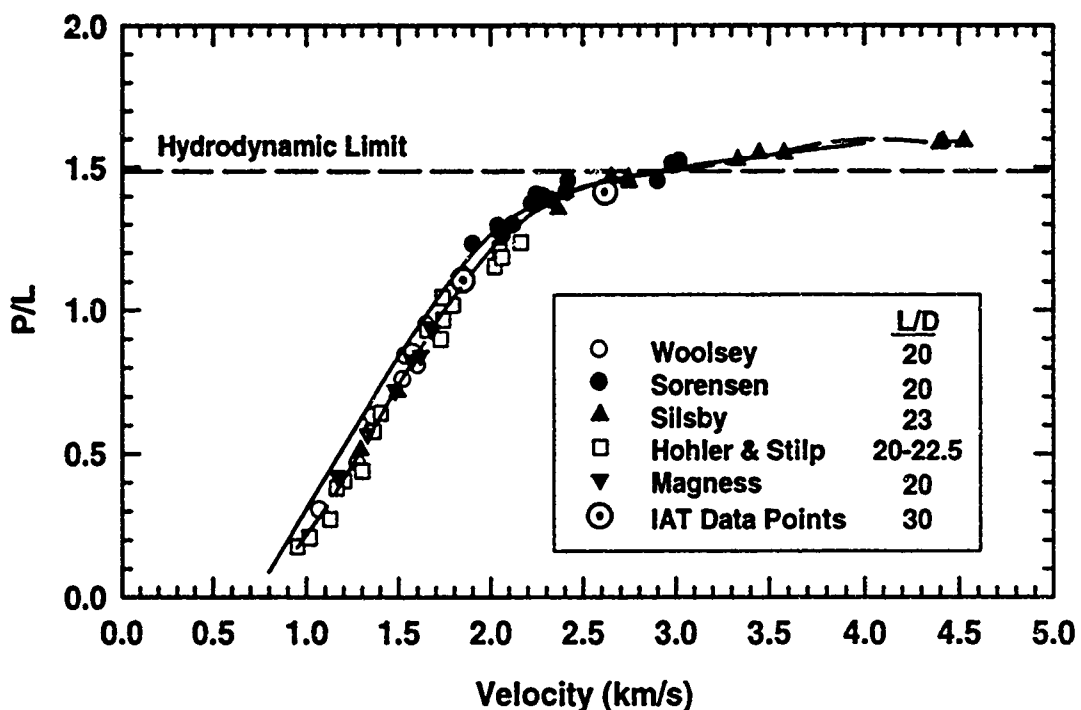


Figure 1. Normalized depth of penetration versus impact velocity.

$$P = \left[\frac{8 KE}{\pi \rho_p V^2} \left(\frac{L}{D} \right)^2 \right]^{1/3} f(V). \quad (3)$$

Using the above equation, the curve in Fig. 2 is generated. Figure 2 represents penetration efficiency, measured here in centimeters of penetration, as a function of impact velocity for a constant energy (2.88 MJ), $L/D = 30$ projectile.

The two impact velocities were selected to give nominally the same depth of penetration into semi-infinite RHA. These two points, 1.775 and 2.60 km/s, are denoted by the solid circles in Fig. 2.² The impact velocity of 1.775 km/s is higher than the muzzle velocity of current field systems. In a "laboratory" environment, a double-travel, 120-mm gun system can almost achieve 1.775 km/s. As this velocity is above current ordnance velocities, but can possibly be achieved with incremental improvements in fielded technology, we refer to this velocity as super-ordnance velocity. A two-stage light-gas gun is required to launch the 2.60-km/s projectile; this velocity will be called hypervelocity.

The projectiles were sized to keep the kinetic energy constant. The dimensions of the projectiles are shown in Table 1. The projectiles were designed as right-circular cylinders with superior grooves for sabot gripping. The diameters given in Table 1 represent the mass effective diameter. The projectiles were made from a Teledyne Firth Sterling 91% tungsten alloy with a nickel-cobalt matrix (designated X27X). The projectiles had a density of 17.45 g/cm³; and an ultimate strength of 1.3 GPa at an elongation of 10%.

² The other points in Fig. 2 will be discussed in Section 2.4.

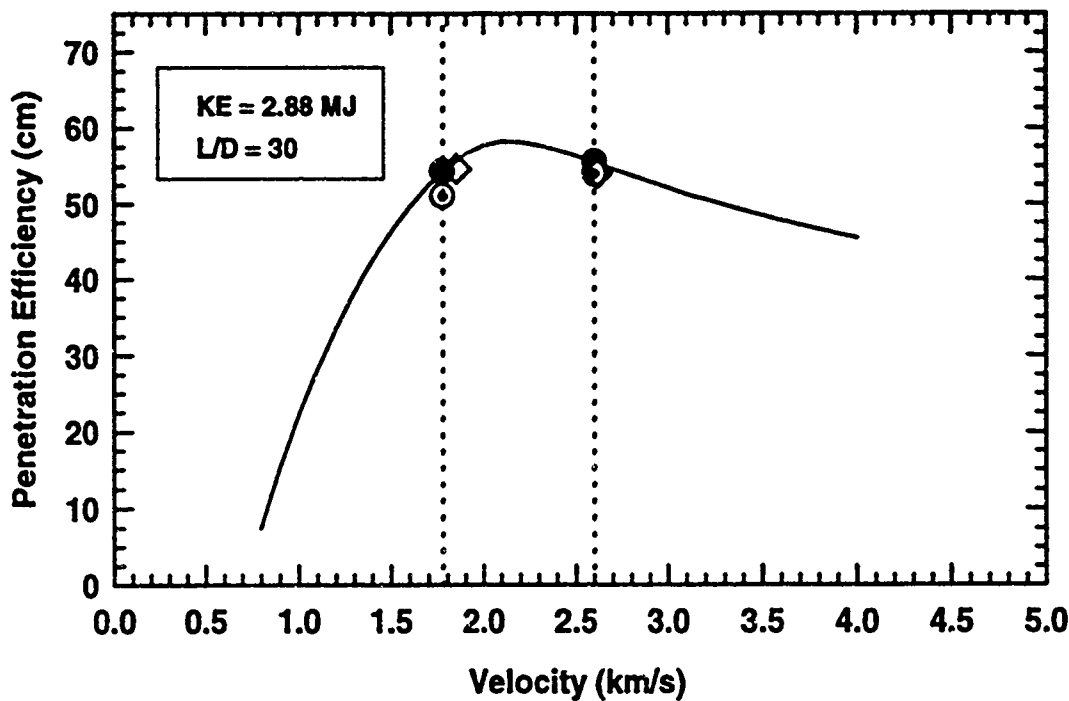


Figure 2. Depth of penetration for constant energy long-rod projectiles.

Table 1. Projectile Dimensions

	Super-Ordnance Velocity	Hypervelocity
Velocity (km/s)	1.775	2.60
Mass (g)	1830	850
Kinetic Energy (MJ)	2.88	2.88
Length (cm)	49.4	38.4
Diameter (cm)	1.65	1.28

Pretest predictions were made for three of the target types: 1) a rolled homogeneous (RHA) target, 2) a high-hard steel, spaced-plate target array, and 3) a ceramic laminate target. A witness pack was placed behind each target, and the depth of penetration of the residual projectile was used as the metric for comparisons between the pretest predictions and the experiments. Figure 3 is a schematic of the experimental arrangement. Figure 3 shows the RHA target; the other targets were substituted for the other tests. The specific details of target configuration and the associated pretest predictions are discussed below. This report is complementary to the reports published by the IAT that describe the experiments and the results [2-3]. The reader is referred to these reports for specific details on the experiments.

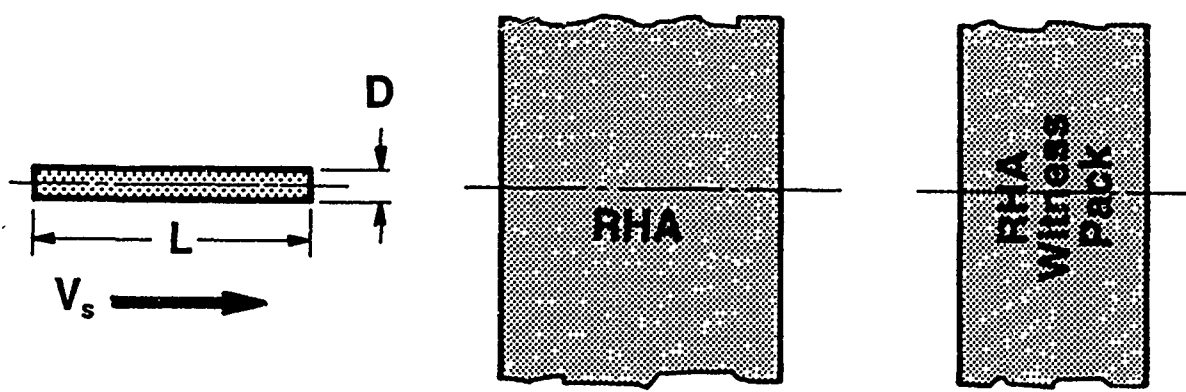


Figure 3. Schematic of experimental arrangement.

2.0 ANALYSIS APPROACH

2.1 Introduction

Pretest predictions were performed using numerical simulations and analytical penetration models. The numerical simulations were performed using the nonlinear, large deformation, Eulerian wavecode CTH [4]. CTH uses a van Leer algorithm for second-order accurate advection that has been generalized to account for a non-uniform and finite grid, and multiple materials; CTH has an advanced material interface algorithm for the treatment of mixed cells. CTH has been modified to allow the flow stress to be functions of strain, strain rate, and temperature [5-6]. The Johnson-Cook model [7] was used to model the viscoplastic behavior of the tungsten alloy and steel plates. The Johnson-Holmquist model [8] was used to model the response of ceramic elements. The analytical models were the MITI model [9], and the Walker-Anderson model [10-11]. Assumptions had to be made about breakout for all the predictions since neither the analytical models nor CTH treat failure explicitly.

2.2 Constitutive Treatment

Viscoplastic behavior of the steels and tungsten alloy was modeled using the Johnson-Cook model [7]. RHA is not in the Johnson-Cook constitutive library; but material constants have been determined for 4340 steel, which is often used as a surrogate material for RHA. The constants for the 4340 steel are for a Rockwell C hardness of R_c30. For the computations, the RHA was modeled with a hardness of 270 BHN, which is representative of the hardness of thick armor plate. The initial yield and strain-hardening coefficient for 4340 steel were reduced proportionally. Constants for high-hard steel, with a hardness of R_c49, exist in the Johnson-Cook constitutive library; the constants were scaled to 500 BHN, the hardness of the plates used in the spaced-plate target experiments. The front element of the ceramic laminate target was slightly harder than the "thick" RHA plates; the hardness was 300 BHN, so the constitutive constants were estimated by scaling the values used for 270 BHN steel to 300 BHN. The constitutive constants for the tungsten alloy projectile were taken from Ref. [12]; thermal softening was not included for the tungsten alloy.³ The constitutive constants used for the various metallic elements of the different targets are summarized in Table 2. The constitutive model used for the ceramic elements will be described in Section 6.2.

³ Good agreement between computations and experiments has been obtained using the constitutive constants for the tungsten alloy given in Table 2.

Table 2. Constitutive Parameters

Material	Y_o (GPa)	B (GPa)	n (-)	C (-)	m (-)	θ_m (K)	G (GPa)	v (-)	σ_{eq} (GPa)
Tungsten Alloy	1.35	0.000	0.00	0.006	1.00	∞	118.3	0.30	1.75
4340 Steel (270 BHN)	0.735	0.473	0.26	0.014	1.03	1793	77.7	0.29	1.42
High-Hard Steel (500 BHN)	1.36	0.517	0.22	0.003	1.17	1778	77.7	0.29	2.00
4340 Steel (300 BHN)	0.844	0.543	0.26	0.014	1.03	1793	77.7	0.29	1.42

$$\sigma_{eq} = (Y_o + B\dot{\varepsilon}_p^n) [1 + C \ln(\dot{\varepsilon}_p/\dot{\varepsilon}_o)] (1 - \theta^m) \quad \dot{\varepsilon}_o = 1.0 \text{ s}^{-1} \quad \theta^* = \left(\frac{\theta - \theta_o}{\theta_m - \theta_o} \right) \quad \theta_o = 300^\circ\text{K}$$

2.3 Treatment of Target Breakout

2.3.1 Numerical Modeling

CTH has a tensile void insertion model, but otherwise, it does not model material failure. In previous work [13], it was found that using the "normal" mixed cell option (described below) results in excessive interaction between the projectile and target during the projectile breakout phase. Real materials fail after reaching some critical strain, but since there is no explicit failure criterion, the target maintains its strength far too long during the thinning of the bulge until breakout finally occurs in the simulation.

Various options exist within CTH to model the flow stress of mixed cells. In one option, the flow stress of the mixed cell is calculated as the volume-fraction weighted average of the flow stresses for the materials within the cell that have strength (this is the "normal" option). In another option, the flow stress of the mixed cell is calculated as the volume-fraction weighted average of the flow stresses for *all* the materials within the cell (including void). This has the effect of significantly reducing the strength of cells that contain an appreciable amount of void. The two options were evaluated against experimental data from Hohler and Stilp [14-15] for finite steel targets. The results of the computations were compared with the experimental lengths and velocities of residual projectiles after perforation of a target. It was found that the latter mixed cell option provided better agreement with the experimental data, most likely because, as the back of the target begins to strain, the flow stress decreases proportionally with the amount of void within the cell. It is believed this option, as compared to the "normal" option, more accurately reproduces the physical characteristics of breakout near the rear target surface.

Computational simulations of long-rod penetration for normal impact into armor steel targets have been performed over a range of impact velocities, e.g., Refs. [12,16-17], and the results have been compared with experiments. Although the majority of the simulations have used $L/D = 10$ projectiles, the numerical simulations are in very good agreement with the results of experiments. Comparisons are considerably more limited with finite-thickness targets. But as described above, with a suitable selection of the mixed cell option, reasonably good agreement was obtained between the numerical simulations and experiments on residual velocity and length of the projectile after

target perforation. With this experience, we concluded that no further "calibration" of the computer code or constitutive models was necessary before simulating the experiments with steel elements. As will be discussed later, this was not the case for the ceramic laminate target.

2.3.2 Analytic Modeling

Only the MITI model [9] had previously been modified for finite-thickness targets, but a breakout algorithm had to be developed for the Walker-Anderson model. Breakout is modeled in a rather empirical fashion. There is a factor that accounts for the resistance to penetration in both analytical models. The details vary depending upon the specific model, but the essence of the approximation is as follows: when the projectile reaches some specified distance from the target back surface, the resistance to penetration is decreased from the nominal value to zero, achieving zero when the projectile reaches the rear surface of the target. The details for the breakout phase for the Walker-Anderson model are given in the paragraphs below.

The residual velocity after breakout can be estimated from a momentum balance assuming that the penetration velocity, tail velocity, and residual length of the projectile are known. Numerical simulations show that the velocity profile, at least along the centerline of the projectile, is remarkably linear while penetrating a semi-infinite target (this observation is for an eroding projectile) [12]. The velocity goes from the penetration velocity u to the tail velocity v over a distance of approximately 1.5-2.0 rod diameters (D). Assuming the total length of the rod after breakout is given by L_r , then a momentum balance gives for the residual velocity V_r :

$$V_r = \left(\frac{v+u}{2} \right) \frac{\mu D}{L_r} + \left(1 - \frac{\mu D}{L_r} \right) v \quad (4)$$

where μ is on the order of 1.5-2.0.

The projectile senses that there is a free surface when the plastic zone in the target reaches the back surface of the target. At this point, the back surface of the target will begin to bulge. In the analytical model, the distance from the penetration interface to the edge of the plastic zone is given by $(\alpha-1) R_c$, where R_c is the crater radius (R_c is typically about 1.8-2.0 D for ordnance velocity impacts). The parameter α is estimated by using cavity expansion theory, e.g., Refs. [11,18-20]. In this technique, a cavity is expanded from zero initial radius at a constant velocity. The procedure calculates a velocity for the interface between the resulting plastic zone and an outer elastic zone; αR_c is the extent of the plastic zone when the cavity has been expanded to the crater radius R_c . Solutions have been derived for both spherical and cylindrical (incompressible) coordinates, and the resulting expressions are [18,19]:

$$\alpha = \left(\frac{2E_t}{3Y_t} \right)^{1/3} \quad (5a)$$

$$\alpha = \left(\frac{\sqrt{3}E_t}{2(1+v_t)Y_t} \right)^{1/2} \quad (5b)$$

where E_r , v_r , and Y_r are Young's modulus, the Poisson ratio, and the flow stress of the target, respectively. The difference in these expressions is really just in the exponent, as $\sqrt{3/2(1+0.3)} = 0.666173\dots \approx 2/3$.

A constant α , however, underpredicts the depth of penetration as a function of velocity at velocities above 1 km/s. A velocity-dependent α results from the cavity expansion solution when compressible (in the sense of the bulk modulus) plastic response is included. The equation for α is [11]:

$$(\rho_r u^2 + Y_r) \sqrt{K_r - \rho_r \alpha^2 u^2} = Y_r \left(1 + \frac{\rho_r \alpha^2 u^2}{2G_r} \right) \sqrt{K_r - \rho_r u^2} \quad (6)$$

where K_r and G_r are the bulk and shear modulus of the target, respectively. This provides better agreement between the model and experimental data; Eqn. (6) is the expression used to estimate α in the Walker-Anderson model.

A simple analytical approximation has been used to model the effects of breakout. Although some pertinent physical aspects of breakout have been considered in the formulation, the model is essentially phenomenological in nature. The approximation employs a degradation to the value of α . As α decreases, so does the target resistance. There are time-dependent terms for α in the analytical model, but the easiest way to see the dependence on α is to examine steady-state penetration. In the case of steady-state penetration, the Walker-Anderson model provides an explicit relationship for the target resistance R_r of the Tate model [11,21]:

$$R_r \equiv \frac{7}{3} \ln(\alpha) Y_r. \quad (7)$$

Clearly, a decrease in the value of α implies that R_r decreases. Degradation of α in the breakout approximation is facilitated by allowing α to vary from its initial value when the plastic zone first reaches the rear target interface to a value of 1.0 when the projectile reaches the rear surface. Let α_0 be the value for alpha from the cavity expansion expression, T be the target thickness, and R_c be the crater radius. Then the value of α for $T - R_c(\alpha_0 - 1) \leq x \leq T$ is defined to be:

$$\alpha = \alpha_0 - (\alpha_0 - 1) \left[\frac{x - [T - R_c(\alpha_0 - 1)]}{R_c(\alpha_0 - 1)} \right]^n. \quad (8)$$

The exponent n is adjusted to give good agreement between the analytic model and experimental results. In this sense, we have accounted for the physical effect of bulging by using n as the free parameter in order to match experimental data. A graph of Eqn. (8) for various values of n as a function of x/T is shown in Fig. 4. The values of α_0 and R_c were 5.0 and 0.25, respectively, for this example. It is evident from the figure that when $n = 1$, α degrades in a linear fashion with respect to x/T . For $n > 1$, however, the degradation rate of α begins at a slow rate and then increases with

respect to x/T . In our experience, $n = 2$ appears to fit a wide range of breakout data quite reasonably.⁴ Moreover, it appears to be physically consistent that the value of n should be greater than 1.0 since during the early stages of breakout only a small portion of the total plastic zone volume is involved with the rear surface of the target, causing the effects of breakout on target resistance to be small.

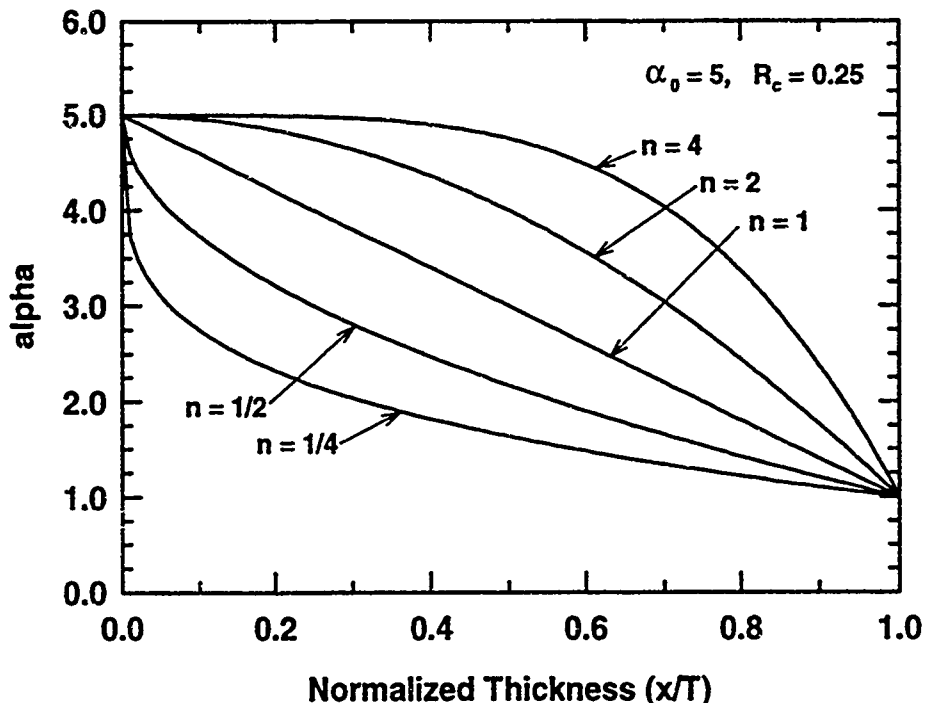


Figure 4. Variation of α with x/T .

2.4 Baseline Response

As mentioned in the previous section, the penetration curve in Fig. 1 and the penetration efficiency curve in Fig. 2 are for $L/D = 20$ projectiles. Penetration efficiency decreases with increased aspect ratio; therefore, the baseline performance for the two projectiles into semi-infinite RHA needed to be determined. Two experiments were performed. The results are given in Table 3, and are shown in Figs. 1 and 2 as the open circles with a dot at the center of the circles.

The high-velocity experiment was essentially at the desired velocity, but the impact velocity for the low-velocity experiment was too high. It is necessary to estimate the penetration performance at the baseline velocities. Two methods will be presented here.

The first procedure relies on the existence of other experimental data to estimate the slope of the P/L versus V curve. In the ordnance velocity range, P/L can be written as a linear function of the impact velocity V :

⁴ Using $n = 2$, the model did reasonably well in reproducing data from Hohler and Stilp [14-15] for the length and velocity of the residual rod after breakout (tungsten rods into steel targets).

Table 3. Baseline Penetration into Semi-Infinite RHA

Velocity (km/s)	P_{exp} (mm)	P/L (:)	P_{adj} Eqn. (10)	$(P/L)_{adj}$ Eqn. (10)	P_{adj} Eqn. (12)	$(P/L)_{adj}$ Eqn. (12)	P_{adj} Eqn. (13)	$(P/L)_{adj}$ Eqn. (13)
1.85	546	1.10	-	-	-	-	-	-
2.62	541	1.41	-	-	-	-	-	-
1.775	-	-	510	1.03	515	1.04	524	1.06
2.600	-	-	N/A	N/A	540	1.41	537	1.40

$$\frac{P}{L} = a + bV \quad (9)$$

where the intercept a and the slope b depends upon the L/D and the specific projectile material (assuming that the target is RHA) [22]. Therefore, $(P/L)_{adj}$ is given by:

$$\left(\frac{P}{L}\right)_{adj} = \left(\frac{P}{L}\right)_{exp} + b(V_{adj} - V_{exp}) \quad (10)$$

In general, the slope b is of the order of 1.00; for $L/D = 30$ projectiles, a slope of 0.984 was found from a linear least-squares curve fit to data over the velocity range of 1.4 to 1.75 km/s [23]. At impact velocities above 1.8 km/s, the P/L curve becomes nonlinear and turn towards the hydrodynamic limit, e.g., see Fig. 1. A more complicated expression can be used to fit the data over the entire velocity regime. Sorensen, *et al.* [1], did this with the hyperbolic expression:

$$\frac{P}{L} = 0.275 + 0.595V - 0.940[1.304 - 1.259V + 0.315V^2]^{1/2} \equiv f(V). \quad (11)$$

The derivative of $f(V)$ with respect to velocity gives the slope of the P/L curve, and corrections can then be estimated over the entire velocity range from:

$$\left(\frac{P}{L}\right)_{adj} = \left(\frac{P}{L}\right)_{exp} + \frac{df(V)}{dV}(V_{adj} - V_{exp}). \quad (12)$$

The second procedure adjusts the depth of penetration by taking a simple ratio of the impact velocities, i.e.:

$$\left(\frac{P}{L}\right)_{adj} = \left(\frac{P}{L}\right)_{exp} \left(\frac{V_{adj}}{V_{exp}} \right). \quad (13)$$

The procedure given in Eqn. (13) is not as accurate as that of Eqns. (10) and (12), but if the velocity dependence of P/L cannot be estimated *a priori*, then Eqn. (13) may be the only way to estimate the adjustment.

The two procedures (with two different equations for the first procedure) were applied to the experimental data to obtain the baseline penetration of the $L/D = 30$ projectiles into semi-infinite RHA at the impact velocities 1.775 km/s and 2.600 km/s. The values are shown in Table 3. It is believed that Eqn. (10) is more accurate than Eqn. (12) for the 1.775-km/s impact case [Eqn. (11) is not as accurate as the linear least squares curve fit for $L/D = 30$ data]. At the higher impact velocity of 2.60 km/s, Eqn. (16) is not applicable. However, because the slope of P/L with respect to V is very small at the higher impact velocities, very little error is associated with the application of Eqn. (12) to $L/D = 30$ projectiles. Equation (13) should only be used if *a priori* (similar) data do not exist from which an estimate can be made of the slope of the penetration curve with impact velocity.

The adjusted data points are shown as diamonds in Fig. 2. These points then represent the baseline penetration into semi-infinite RHA. These points are required to establish e_m efficiencies.

3.0 FINITE-THICKNESS RHA TARGET

3.1 Target Description

The RHA target is shown in Fig. 5. A 45.7-cm thick block was built up by welding four RHA (MIL-A-12560G, Class 3) square plates together (two 10.16-cm thick plates, and two 12.70-cm thick plates). A 7.62-cm thick gap separated the main target block from a second RHA block which served as a witness pack.

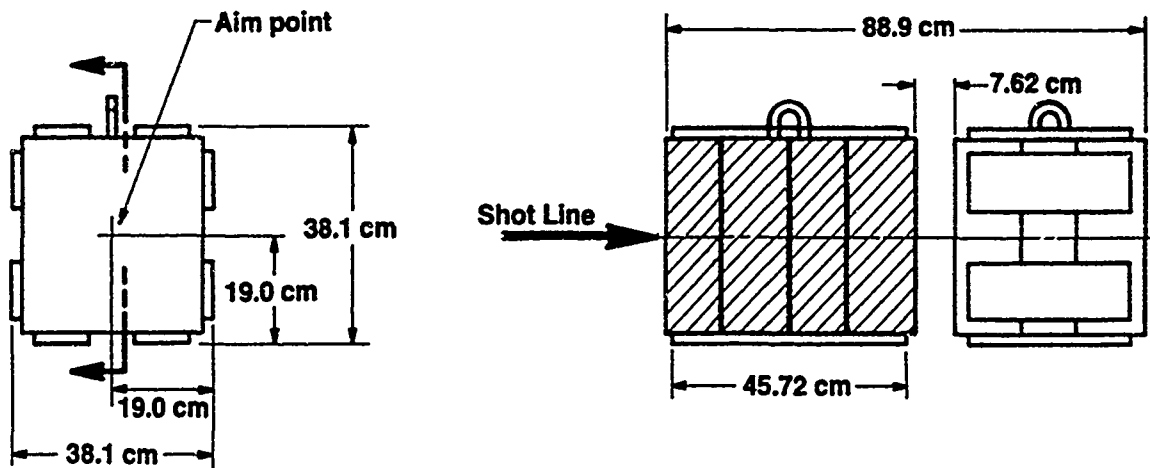


Figure 5. RHA target and witness pack dimensions.

3.2 Numerical Simulations

The two-dimensional axisymmetric option of CTH was used to model the problem. Square zones (1.27 mm on a side) were employed in the initial projectile/target interaction region, and near the back of the target. The length of zones in the central region of the target was increased gradually to a maximum length of about 3 mm at the mid-depth distance. This was done to speed up the calculation and conserve computational memory. Square zones (1.27 mm) were also employed in the projectile/target interaction region for the RHA witness pack located behind the RHA target.

The tail and interface (penetration) velocities versus time, along the projectile centerline, are shown in Fig. 6 for the two impact velocities, $V_p = 1.775$ and 2.600 km/s. The tail and interface velocities versus the position of the projectile nose (depth of penetration) are plotted in Fig. 7. The initial positions of the rear of the target and the front of the witness pack are drawn on Fig. 7.

The arrival of the elastic wave at the rear of the projectile is clearly evident in Figs. 6-7. The deceleration of the projectile by the elastic wave is given by:

$$\Delta v = \frac{2Y_p}{\rho_p c} \quad (14)$$

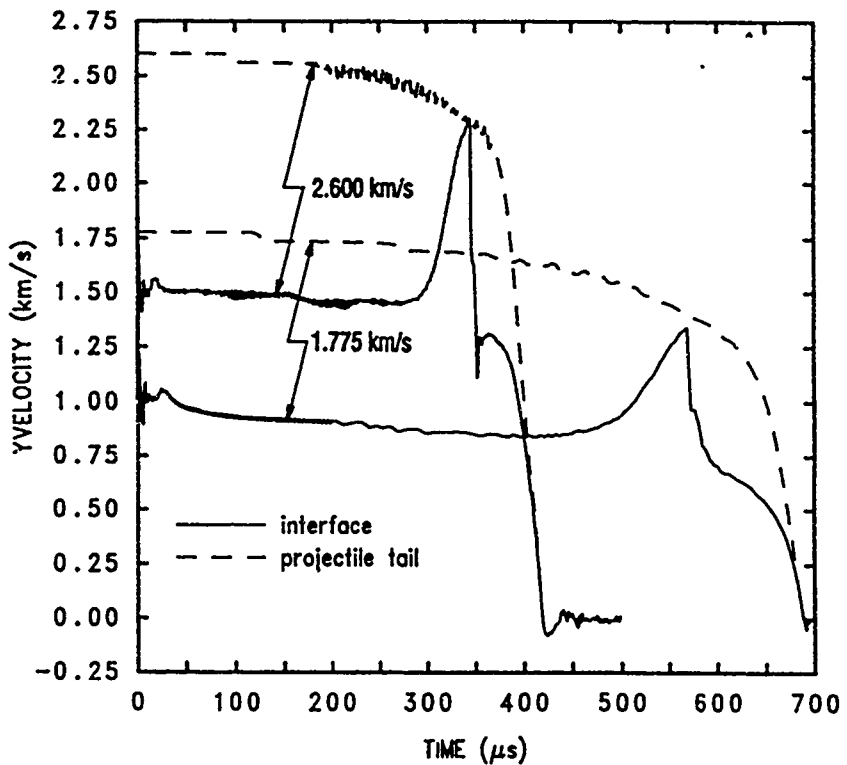


**Figure 6. Penetration and tail velocities versus time,
RHA target—CTH results.**

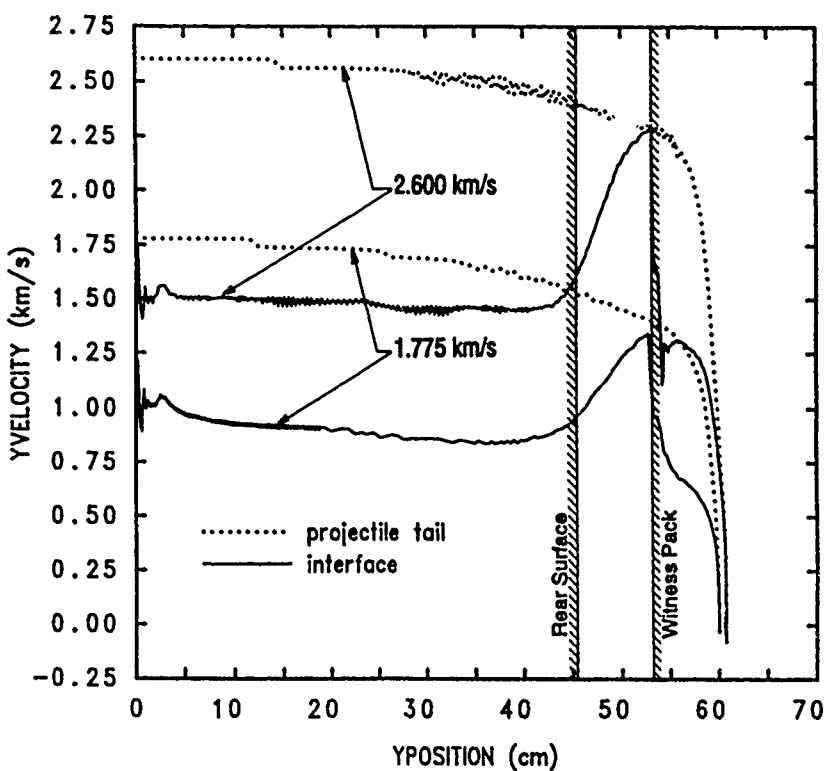


**Figure 7. Penetration and tail velocities versus depth of penetration,
RHA target—CTH results.**

where Y_p is the flow stress of the projectile, ρ_p is the projectile density, and c is the longitudinal sound speed. Δv is approximately 50 m/s for the tungsten alloy. The step deceleration occurs every (approximately) $2l/c$ time increment, where l is the current length of the projectile. Notice that as the length of the projectile gets shorter, the step deceleration occurs more frequently. This elastic deceleration is slightly more important for the slower moving projectile since 50 m/s is a larger percentage of the initial impact velocity; also, because the projectile is moving slower, there is more time for elastic waves to propagate between the projectile/target interface and the projectile tail. However, only the first several elastic step decelerations are discernable in the tail velocity. The elastic-plastic interface of the projectile (a material nonlinearity) is not a perfectly reflective interface, and some of the wave "leaks" through and a portion of this transmitted wave then reflects from the projectile-target interface, the amount reflected being proportional to the impedance mismatch. The complicated wave interactions between the elastic-plastic interface and the projectile-target interface "smears" the elastic deceleration wave. In addition, the nose of the projectile is decelerated because of its interaction with the target, providing further deceleration waves to the elastic portion of the projectile. Therefore, after the first few reflections, the deceleration becomes continuous, thereby resulting in a "smooth" deceleration history for the projectile tail.

The penetration velocity along the centerline is approximately steady-state (aside from the effects of the initial shock) until the projectile is within several projectile diameters of the rear surface of the target. With target bulging, i.e., with the lack of material confinement, the projectile nose velocity increases. The distance from the rear surface at which the projectile "senses" the free surface can be estimated from where the penetration velocity begins to deviate from the quasi-steady value. For the lower impact velocity case, the distance is approximately 7.0 - 7.5 cm, while for the higher impact velocity case, this distance is approximately 6 cm. These distances should be normalized by the diameter of the respective projectiles. Performing this normalization, the lower velocity projectile senses the rear surface of the target at approximately 4.2-4.5 projectile diameters from the rear surface; the higher velocity projectile senses the rear surface at approximately 4.7 projectile diameters.

After target perforation, the nose and tail velocities begin to equilibrate. For the lower velocity impact case, the nose and tail velocities are within approximately one elastic wave transit of complete equilibration when the projectile impacts the witness pack. The nose and tail velocities have equilibrated for the higher velocity impact case when the projectile impacts the witness pack. Another shock is generated with the impact of the remnant projectile against the witness plate. If the remnant projectiles had been longer, then steady-state velocities would be achieved in the witness pack; however, the lengths of the projectiles after penetrating and perforating the main RHA target plate are fairly short. A discussion of the residual lengths of the rods after perforating the main target element will be given below.

The pressure (mean stress) at the projectile-target interface (along the centerline) versus position is shown for the two impact cases in Fig. 8. After the initial impact shock, the pressure decays to a steady-state value. The pressure decreases as the projectile approaches the rear surface due to decreased confinement, and falls to zero when the target is perforated. Subsequent impact

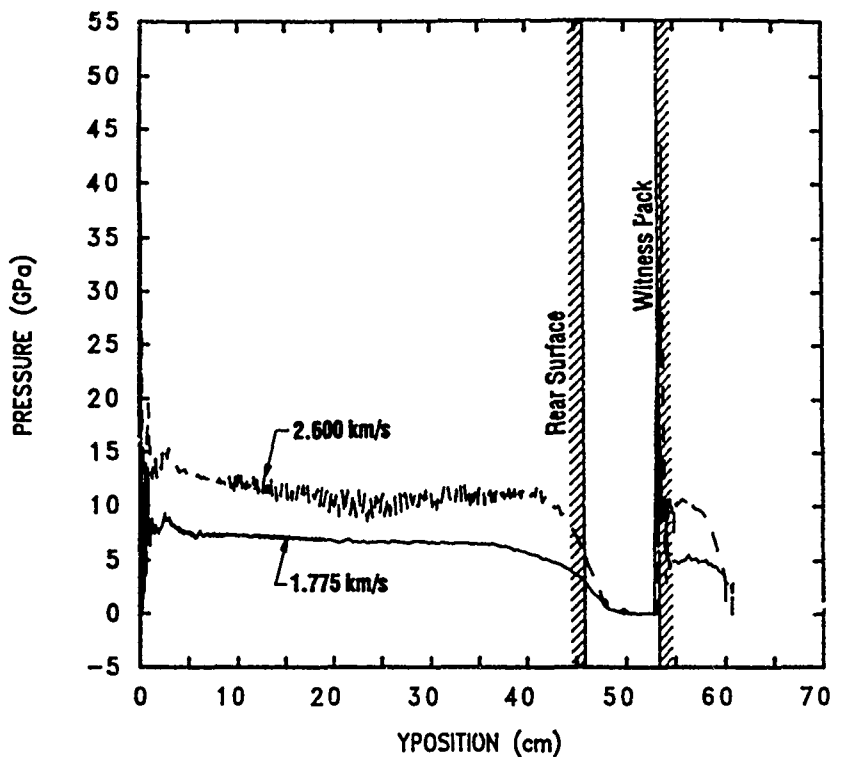


Figure 8. Pressure versus position, RHA target—CTH results.

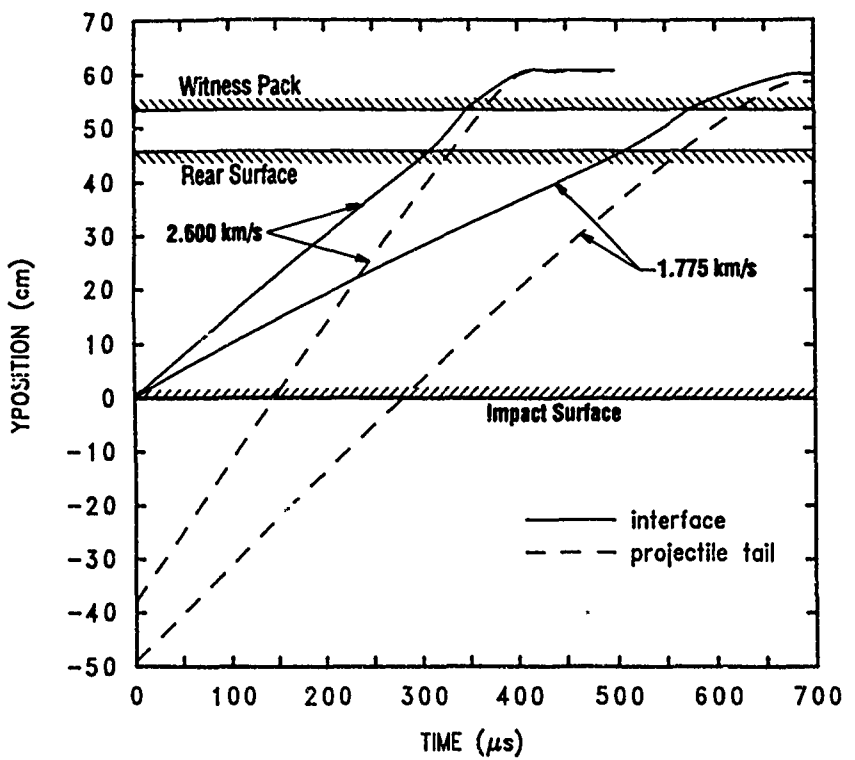


Figure 9. Nose and tail positions versus time, RHA target—CTH results.

of the residual projectiles into the witness pack result in pressure (shock) spikes which then decay to the quasi-steady-state pressures approximately equal to the penetration pressures in the main target. At the end of penetration, the pressure drops to zero.

The position versus time of the nose and tail of the projectile are plotted in Fig. 9. The position of the nose is coincident with the projectile/target interface, and this position represents the instantaneous depth of penetration. The initial positions of the impact surface, the rear of the target, and the front of the witness pack are also shown in Fig. 9. The projectile, just before perforation of the RHA target, and a short time after perforation, is shown in Figs. 10 and 11 for the two impact velocities, respectively. Contour lines for the pressure are shown on the right-hand side of the figures, and contour lines for equivalent plastic strain are shown on the left-hand side of the figures. Comparing Figs. 10a with 10b, and Figs. 11a with 11b, it is evident that the projectile continues to erode after it reaches the original back surface of the RHA target, even though breakout is almost imminent in Figs. 10a and 11a.

The lengths of the projectiles, normalized by their respective diameters, are plotted as a function of penetration depth in Fig. 12. The computations indicate that the higher velocity projectile undergoes more rapid (normalized) erosion at the very beginning of penetration, but then the rate of erosion per unit depth of penetration is approximately the same for both projectiles. The continued erosion of the projectiles after reaching the original free surface of the target is evident in the figure since the lengths continue to decrease as the projectile moves into the air gap between the RHA target and the witness pack. For example, in Fig. 10a, the length of the projectile is 7.5 cm; the length of the projectile in Fig. 10b is 7.1 cm. By the time the projectile strikes the witness pack, the length is 6.6 cm. Since the diameter of the projectile is 1.65 cm, the L/D 's are 4.5, 4.3, and 4.0, respectively. Similarly, the lengths of the projectile in Figs. 11a and 11b are 4.8 cm and 4.4 cm, and the length when the projectile impacts the witness pack is 4.1 cm. This corresponds to L/D 's of 3.8, 3.4, and 3.2, respectively, for the higher velocity rod.

Summarizing, the lengths of the projectiles at impact with the witness plates are approximately $4.0D$ and $3.2D$, respectively, for the lower and higher impact velocity cases. The normalized projectile velocities V_r/V_s at impact with the witness pack are 0.783 and 0.881, respectively.

Note that the lower velocity remnant projectile is longer in terms of normalized length, but because the diameter of the two rods are different, the slower velocity remnant projectile is actually quite a bit longer than the higher velocity remnant rod. The final depth of penetration into the witness pack is a function of both the length and the impact velocity. The computations predict that the faster velocity projectile will penetrate slightly deeper into the witness pack: 7.4 cm of penetration versus 6.7 cm of penetration. However, the deeper penetration by the higher velocity projectile is a little more subtle than simply a higher impact velocity. The remnant projectile lengths in the final crater are different for the two rods, e.g., see Figs. 12 and 13. From Fig. 12, it is seen that approximately $0.9D$ of the projectile is left at the bottom of the crater for the lower impact velocity case; virtually none of the projectile remains at the higher impact velocity case. The material plots at the end of penetration into the witness pack, Fig. 13, shows the differences in the residual projectile. Thus, the higher velocity results in additional penetration as a result of extra projectile erosion.

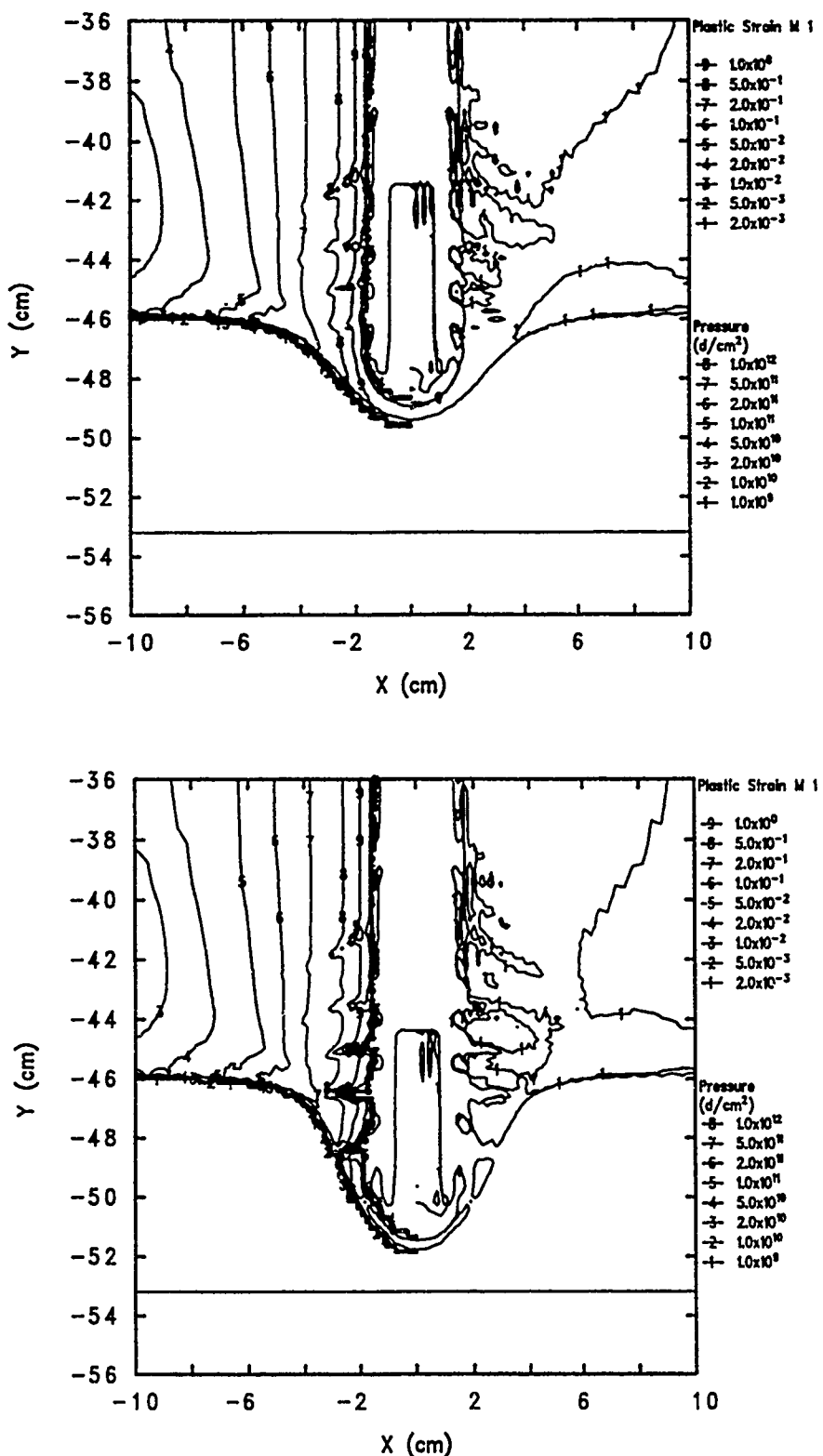


Figure 10. Material interface plots of perforation of the RHA target, $V_p = 1.775 \text{ km/s}$:
a.) Near breakout ($t = 540 \mu\text{s}$) b.) After perforation ($t = 560 \mu\text{s}$).

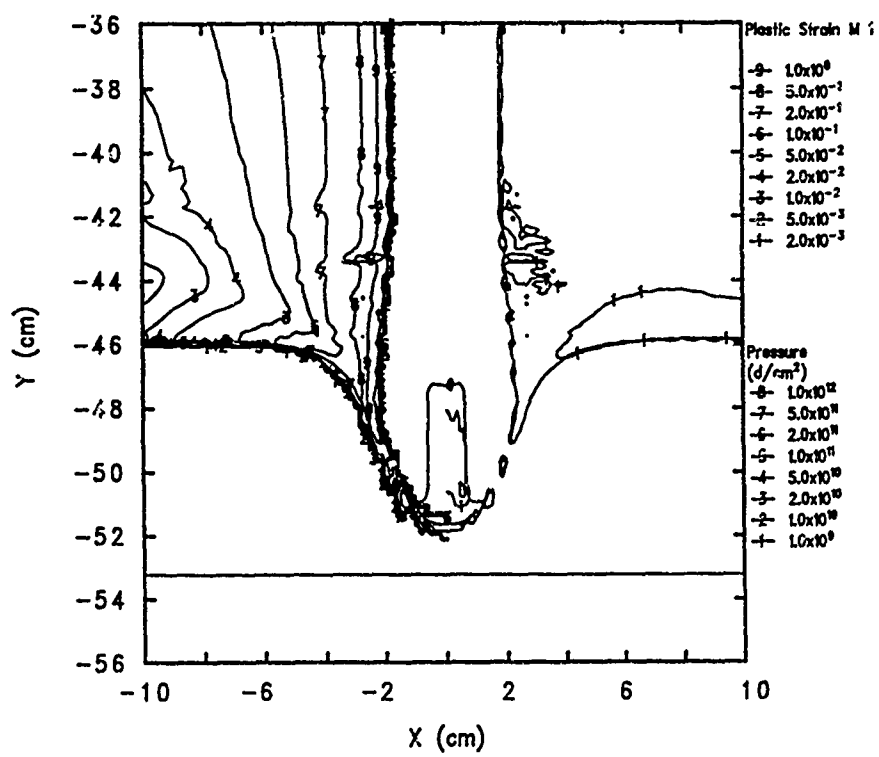
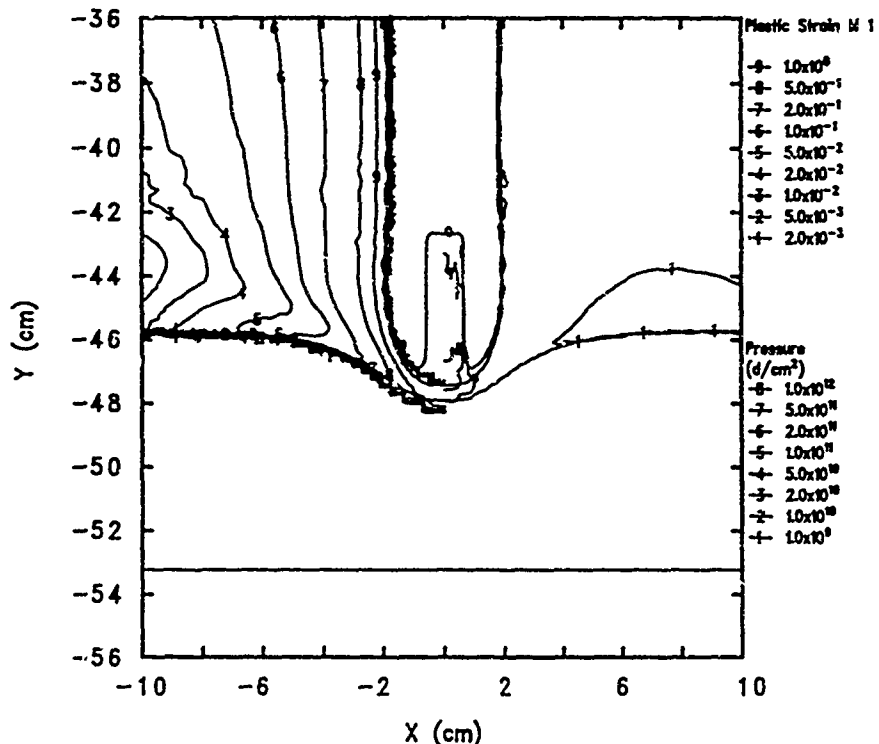


Figure 11. Material interface plots of perforation of the RHA target, $V_p = 2.600 \text{ km/s}:$
a.) Near breakout ($t = 320 \mu\text{s}$) b.) After perforation ($t = 340 \mu\text{s}$).

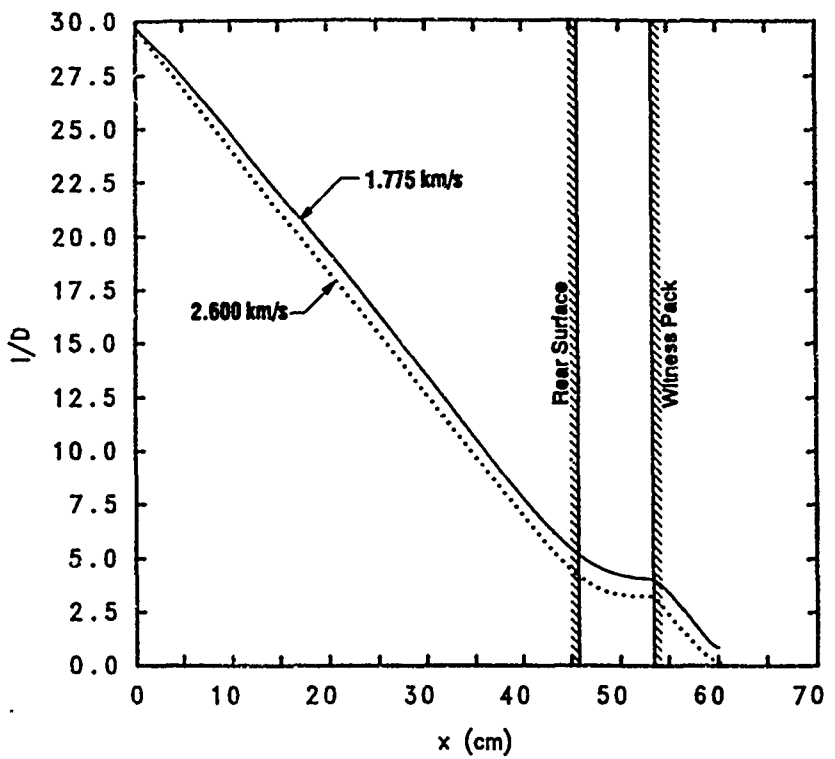


Figure 12. Normalized length of the projectiles versus depth of penetration, RHA target—CTH results.

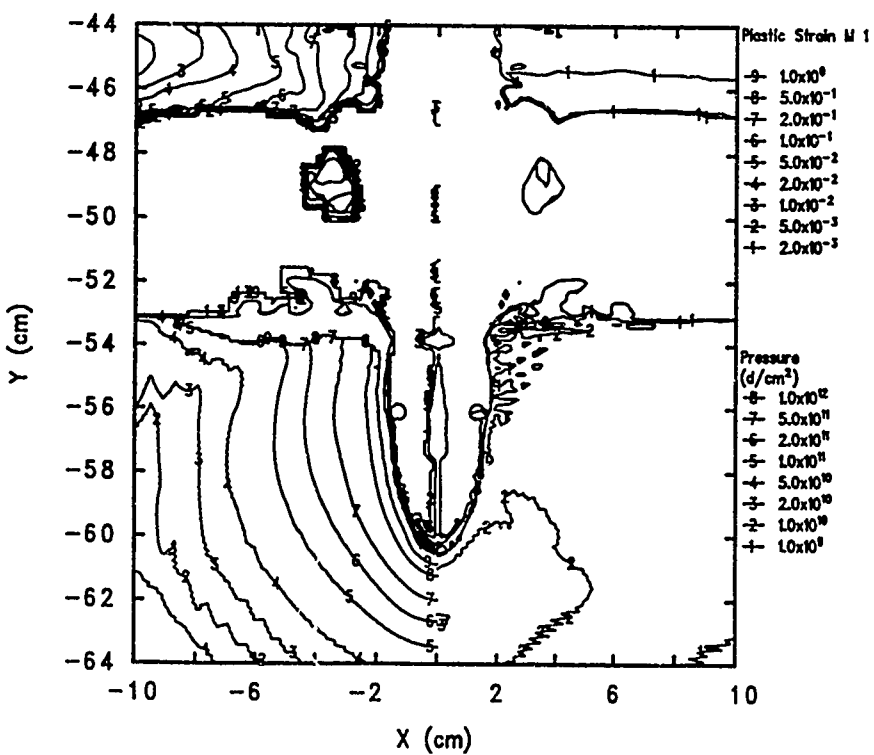
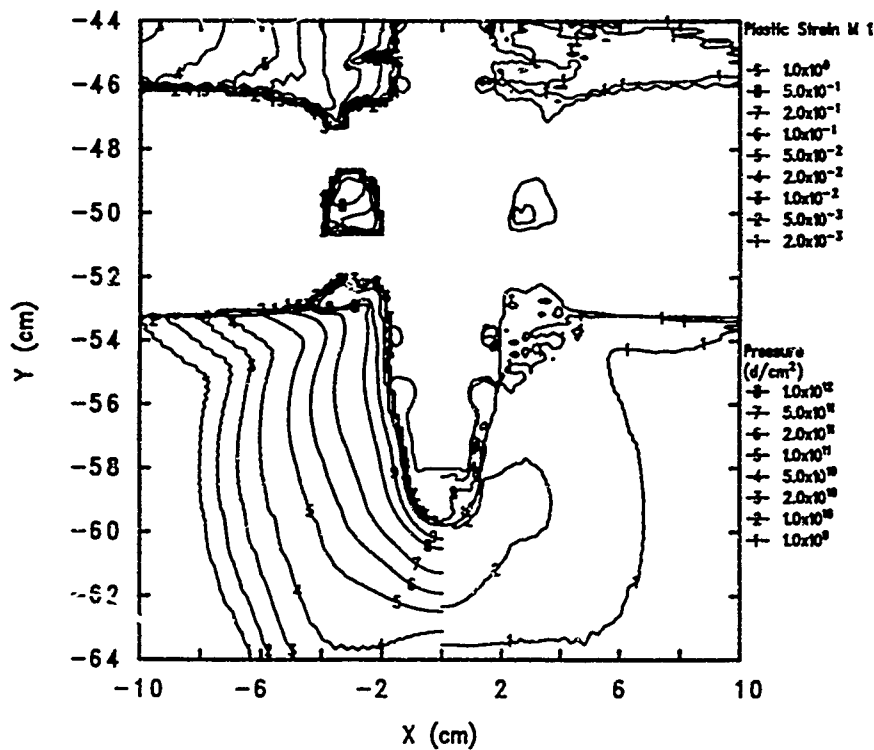


Figure 13. Material interface plots of final crater in witness pack:
a.) $V_p = 1.775$ km/s b.) $V_p = 2.600$ km/s.

The total penetration of steel (the total distance travelled by the projectiles minus the width of the air gap between the target and the witness plate) are virtually identical for the two impact cases. There is approximately 0.75 cm difference in the total steel penetration; this is only a 1.4% difference in the two computations. However, since the absolute amount of penetration into the witness pack is considerably smaller, the 0.75 cm difference represents a 10% difference in penetration depths into the witness pack.

3.3 Analytical Predictions

The analytical models treat the materials as rigid plastic. The flow stresses were taken as being representative of dynamic flow stresses for the target and projectile. The flow stress for the RHA was assumed to be 1.2 GPa, and that of the tungsten alloy projectile, 1.5 GPa. These values can be estimated from the Johnson-Cook model by substituting expected values for ϵ and $\dot{\epsilon}$.

The position versus time predictions from the Walker-Anderson model are shown in Fig. 14. It is assumed, upon perforation of the target, that the projectile velocity immediately equilibrates. The times for the projectiles to traverse the distance between the RHA target and the witness pack are estimated from the gap distance (7.6 cm) and the residual velocities of the two projectiles. The initial conditions for impact into the witness pack is then given by the lengths and velocities of the projectiles. Figure 14 looks very similar to Fig. 9. The lengths of the projectiles versus the depth of penetration are shown in Fig. 15. The normalized lengths of the projectiles are shown in Fig. 16. Again, Fig. 16 looks similar to Fig. 12 except that, in the analytic model, there is no further erosion of the projectile once it has reached the rear surface of the target. In addition, the Walker-Anderson model overpredicts the total amount of erosion for the lower velocity projectile.

The Walker-Anderson model predicted that the depths of penetration into the witness pack were 6.7 cm and 7.5 cm for the 1.775 and 2.600-km/s impacts, respectively. The MITI model predicted 6.9 cm and 7.4 cm of penetration into the witness pack. These results are in remarkably close agreement with the CTH results.

3.4 Experimental Results and Summary

The depths of penetration into the witness pack for the experiments, CTH, and the analytical models for the RHA target are given in Table 4. The agreement between the models appears extraordinary, but we note that the analytical models were developed for long-rod penetration into semi-infinite armor steels. Even though the target is finite in thickness, it is sufficiently thick that most of the projectile erodes during penetration of the RHA target. What is surprising, however, is that the models agree so well with experiment since none of the analytical models account fully for the L/D effect [22] (the MITI model has no L/D effect, while the Walker-Anderson model accounts only for approximately 50% of the effect).⁵ From this, we conclude that somehow the effects of breakout and L/D provided compensating errors. Nevertheless, it still is remarkable that

⁵ The experimental data used for verification of the ability of the analytical models to reproduce experiments were projectiles with $L/D \approx 10$.

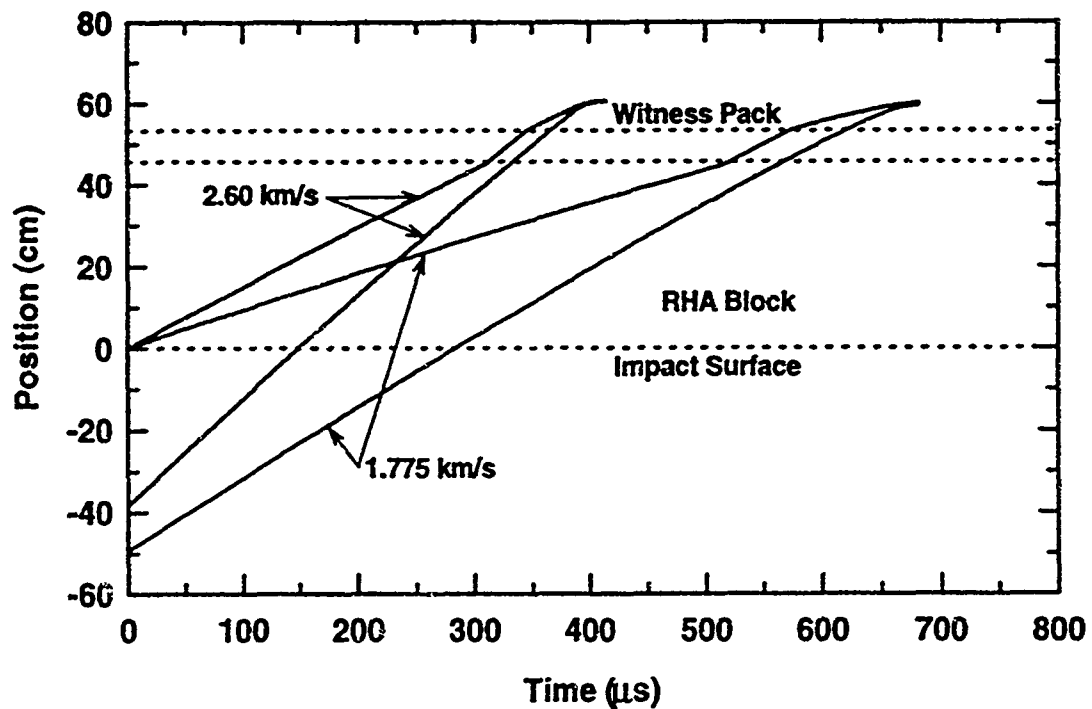


Figure 14. Nose and tail position versus time,
RHA target—Walker-Anderson results.

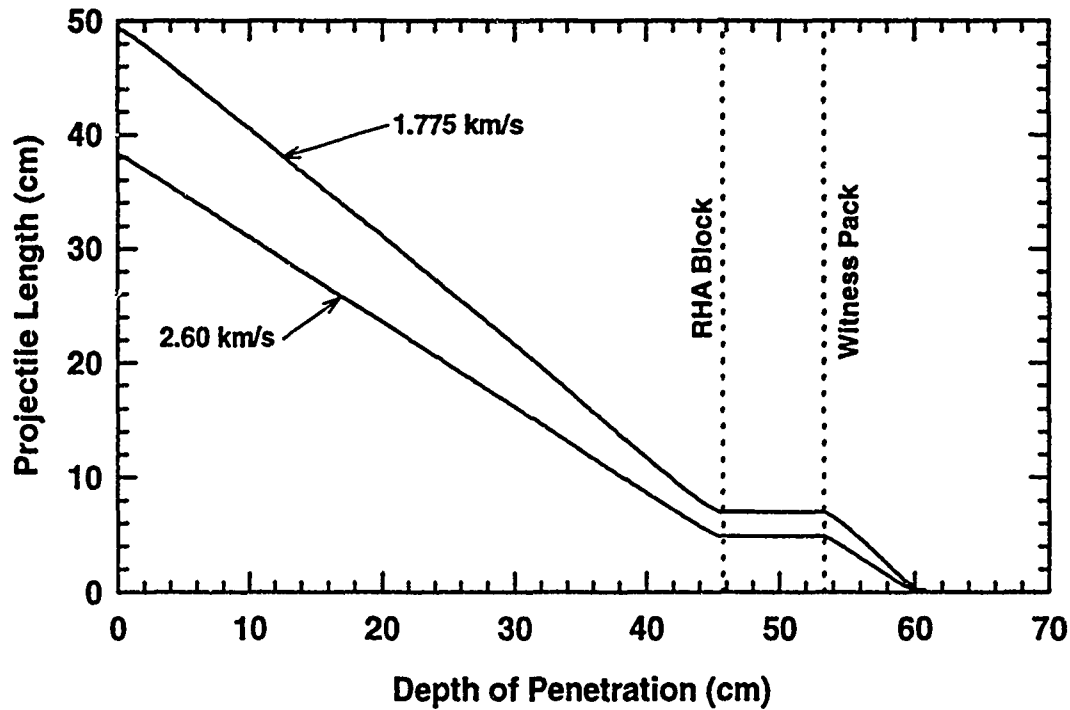


Figure 15. Projectile lengths versus depth of penetration,
RHA target—Walker-Anderson results.

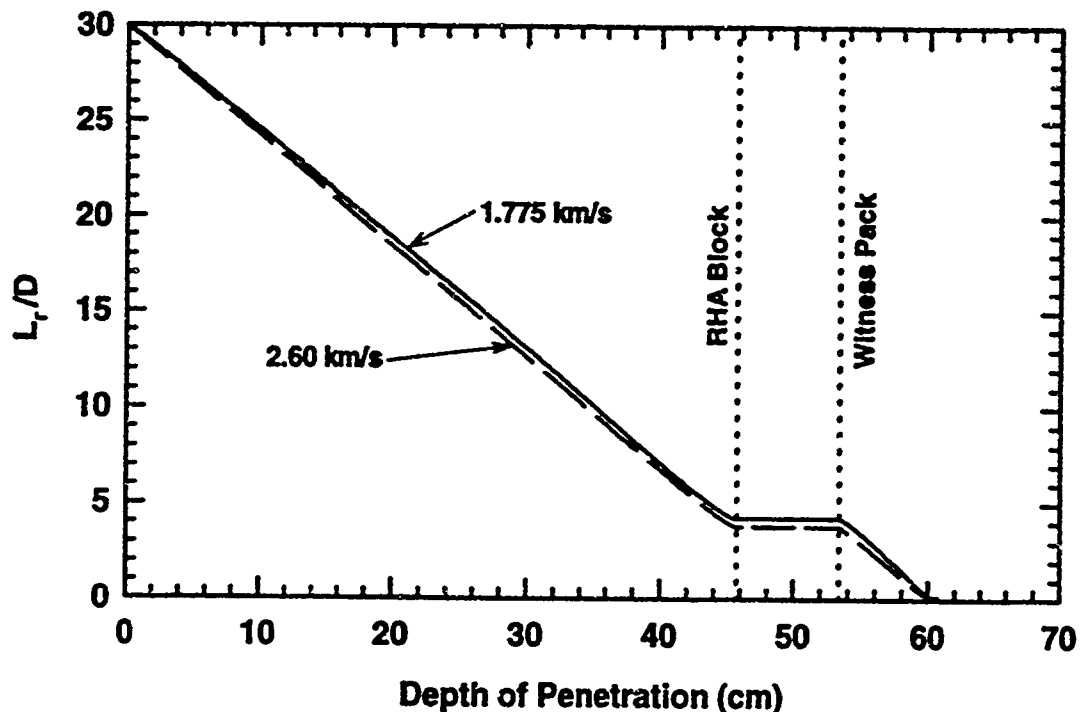


Figure 16. Normalized length of the projectiles versus depth of penetration, RHA target—Walker-Anderson results.

all the models correctly predict that the high-velocity rod penetrates approximately 10% further into the witness pack than the low-velocity projectile. This is even more remarkable in view that all the models correctly predict that there is only 1.4% difference in the total penetration.

Table 4. Depths of Penetration into Witness Pack: RHA Target

V_i (km/s)	Penetration into Witness Pack (cm)			
	Experiment	CTH	Walker-Anderson	MITI
1.80	6.7	-	-	-
1.775	-	6.7	6.7	6.9
2.59	7.4	-	-	-
2.600	-	7.4	7.5	7.4

The numerical simulations predict that there will be approximately $0.75D$ residual rod left in the crater from the lower velocity impact test, but essentially no intact residual penetrator material from the higher velocity impact. This prediction was verified in the experiments; i.e., a residual projectile with a length on the order of one diameter was recovered from the witness pack for the 1.80-km/s experiment, but there was no remnant projectile for the 2.59-km/s impact.

Four additional experiments were performed with the RHA target, and comparisons between the pretest predictions and the experimental results can also be made for these experiments. In these additional experiments, the witness pack was removed so that flash X-rays could be used to determine the residual velocity and length of the projectile after perforation of the RHA target, Fig. 17. The experimental results are given in Table 5. The results from CTH and the Walker-Anderson model were examined to estimate the residual velocities and lengths of the projectile after perforation of the RHA target (and before impacting the witness pack); these results are also given in Table 5.

The results from repeat experiments provide an indication of the expected spread in the experimental data. For these experiments, the spread in the residual velocities is 2-5%, and the spread in the residual lengths is between 6-11%. The models are in reasonable agreement with the experimental results, although the agreement is somewhat better for the high-velocity case. For the 1.775-km/s impact case, the model predictions lie outside the uncertainty bound of the experiments. For this low-velocity case, there is a tendency for the models to overpredict the residual velocity and underpredict the residual length of the projectile. These represent compensating errors in the impact against the witness pack.

There are two possible sources of error on the accurate prediction of projectile residual length: inadequate modeling of breakout, or the strength of the projectile used in the calculation was too low. With respect to the latter possibility, it is well documented that the strength of the projectile does not appreciably effect the depth of penetration into a semi-infinite target; however, the length

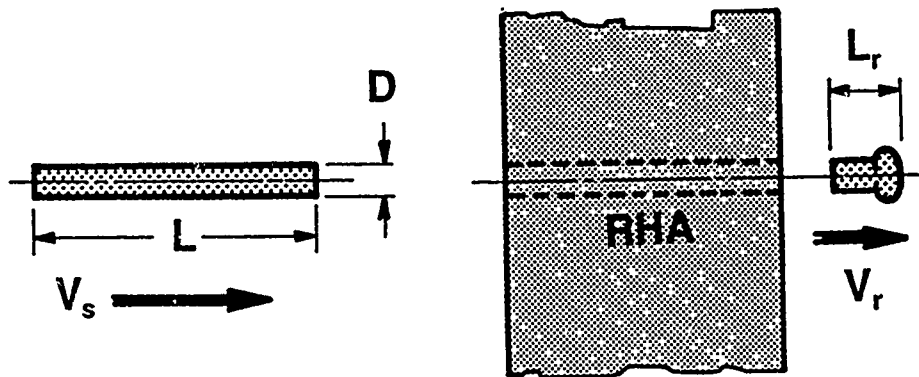


Figure 17. Schematic of experimental arrangement without witness pack.

Table 5. Residual Length and Velocity After Perforation of RHA Target

	V_r (km/s)	D (cm)	V_r (km/s)	V_r/V_i (-)	L_r (cm)	L_r/D (-)
Experiment	1.73	1.65	1.30	0.751	7.7	4.7
Experiment	1.77	1.65	1.36	0.768	8.2	5.0
CTH	1.775	1.65	1.40	0.789	6.60	4.00
Walker-Anderson	1.775	1.65	1.52	0.856	7.00	4.24
Experiment	2.53	1.28	2.23	0.881	4.9	3.8
Experiment	2.57	1.28	2.26	0.879	4.4	3.4
CTH	2.600	1.28	2.29	0.881	4.40	3.44
Walker-Anderson	2.600	1.28	2.38	0.915	4.57	3.57

of the residual projectile after perforation of a finite-thickness target is sensitive to the strength of the projectile. The postulate that strength and breakout effects are the primary sources of the errors is supported by the observation that better agreement between the predictions and the experiments exists at 2.600 km/s where strength effects are not as dominant as for the lower velocity impact. Regardless of the sources of errors, these experiments, where information was obtain for the residual velocities and lengths of the projectiles, demonstrate that even though the computational and analytical models provided the correct integrated response (i.e., depth of penetration into the witness pack), the models do not reproduce other "details" of the experiments with equal fidelity.

4.0 PENETRATION OF SHORT L/D PROJECTILES

4.1 Introduction

It has long been observed that P/L increases in semi-infinite targets as the aspect ratio L/D of the projectile decreases, e.g., Refs. [24-25]. However, the absolute depth of penetration is proportional to the length of the projectile. Therefore, in military applications, the emphasis has been on increasing the aspect ratio to $L/D \sim 30$. Practical armor systems have finite dimensions, with the result that a portion of the original projectile could perforate the armor system, and in fact, the armor technology targets were designed to stress the projectile, but be defeated by the projectile. It has been reported that the remnant projectile can contribute significantly to damage behind an armor element [26]. This remnant projectile is characterized by a residual length L_r and residual velocity V_r , and it is desired to obtain an independent estimate of the penetration capability of the residual projectile if L_r and V_r are known. The overall objective of this portion of the study was to gather existing data for short L/D projectiles and demonstrate that P/L can be estimated given L_r and V_r [27].

The database for heavy metal alloy projectiles impacting armor steel targets, such as RHA, for low aspect ratio projectiles at relatively modest impact velocities is not particularly robust. Further, penetration is a strong function of target strength [14-15], and the available data are for various target strengths. The approach taken here is to use similitude modeling to form nondimensional terms, called Pi terms, that will permit a larger experimental database.

4.2 Nondimensionalized Semi-Infinite Penetration

Experience and analytical modeling have demonstrated that the target density, projectile density, impact velocity, and target flow stress are the most important physical parameters [13-14,16] in determining penetration efficiency. These parameters can be formed into two Pi terms: a nondimensional velocity π_1 and a nondimensional density π_2 , defined as:

$$\pi_1 \equiv (\rho_p V^2 / \sigma_t) \quad \pi_2 \equiv (\rho_p / \rho_t) \quad (15)$$

where ρ is the density, V is the impact velocity, and σ is the flow stress. The subscripts p and t denote the projectile and target, respectively.

Figure 18 depicts P/L versus impact velocity for $L/D = 1$ projectiles; Fig. 19 provides similar data for $L/D = 3$ projectiles, and Fig. 20 shows the data for $L/D = 5$ and 6 projectiles. There were so few $L/D = 5$ and 6 data that they were combined into a single data set. The data are from a compendium [28] of penetration data from various sources. The data are for a variety of projectiles into different types and hardnesses of metallic targets. The legend in the figures indicates the projectile material (W, tungsten alloy; St, steel; Al, aluminum) impacting a target material. The number in front of the target designation gives the Brinell hardness of the target material. The letters after the target designation refer to the investigators who obtained the data: e.g., H&S, Hohler and Stilp; C&G, Christman and Gehring; AC, Alex Charters.

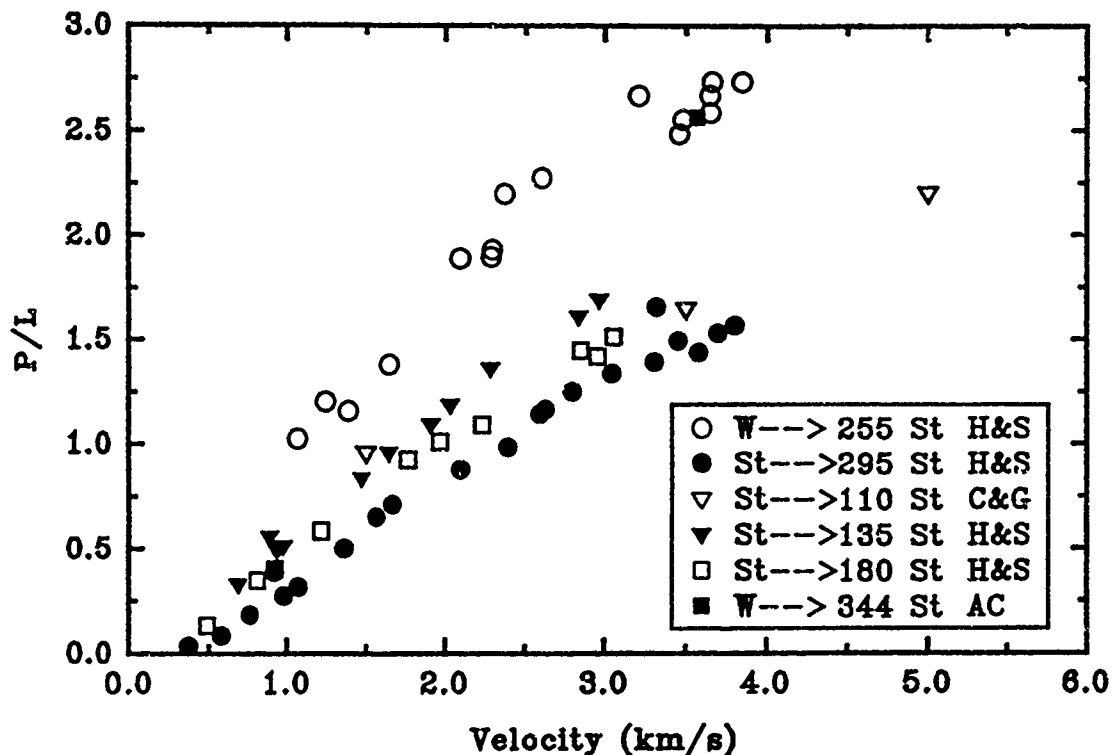


Figure 18. P/L for $L/D = 1$ rods versus impact velocity.

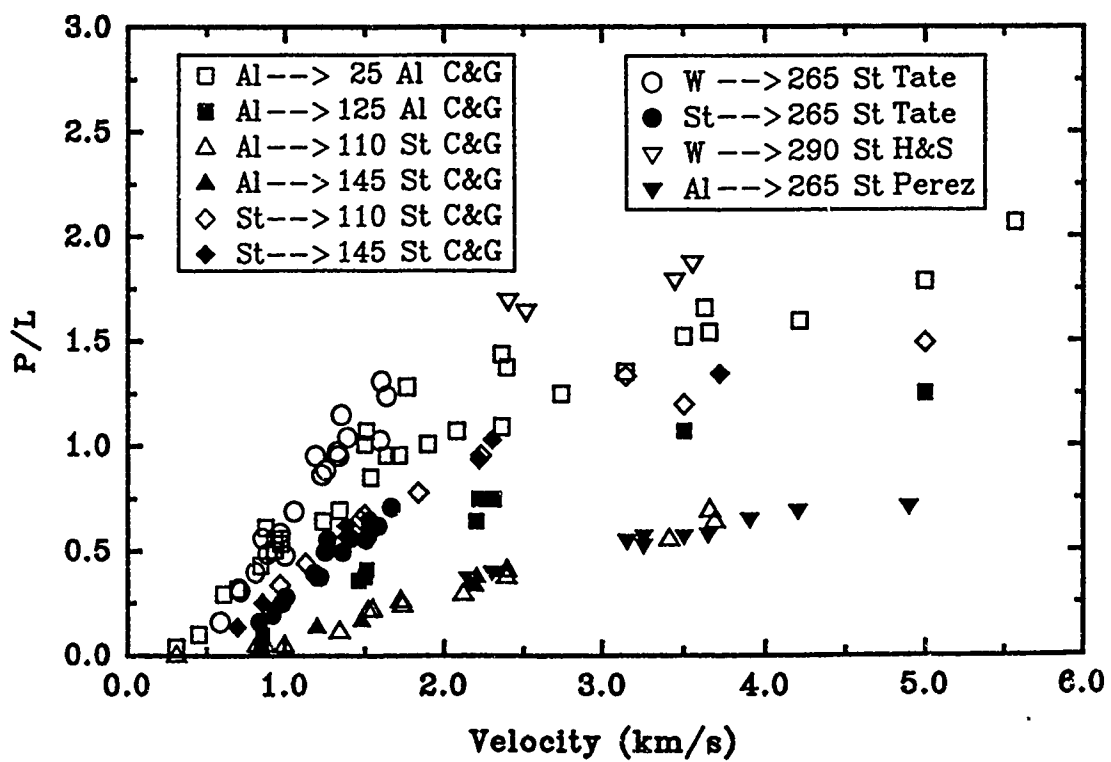


Figure 19. P/L for $L/D = 3$ rods versus impact velocity.

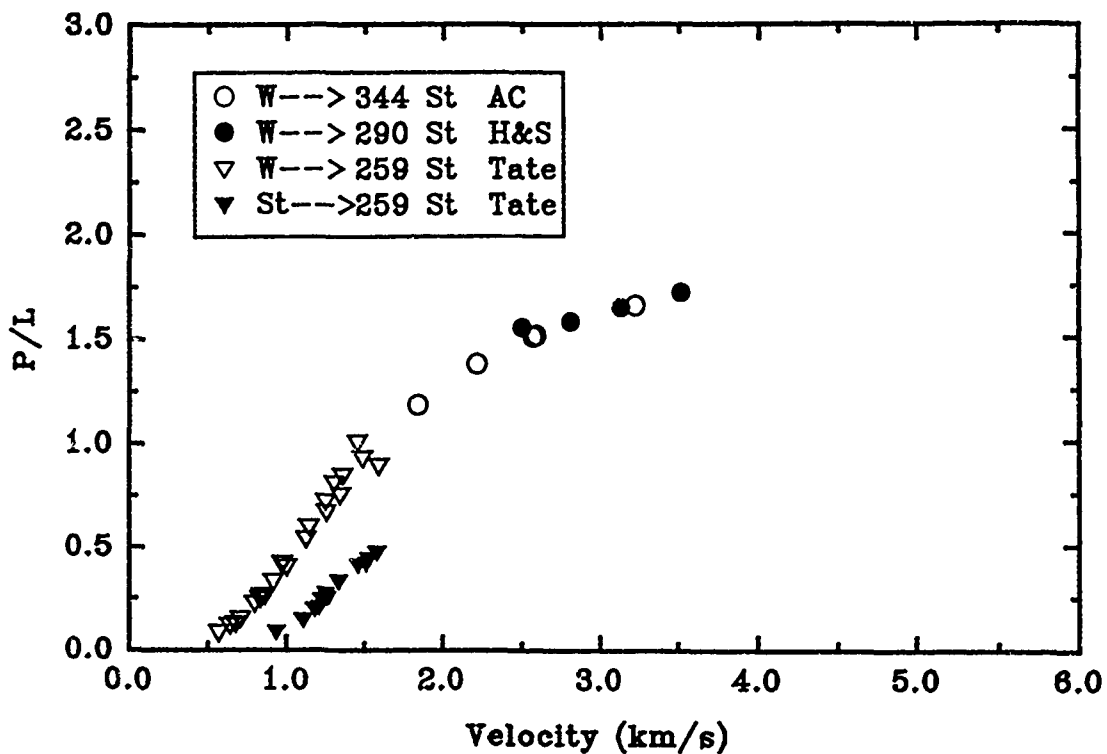


Figure 20. P/L for $L/D = 5$ and 6 rods versus impact velocity.

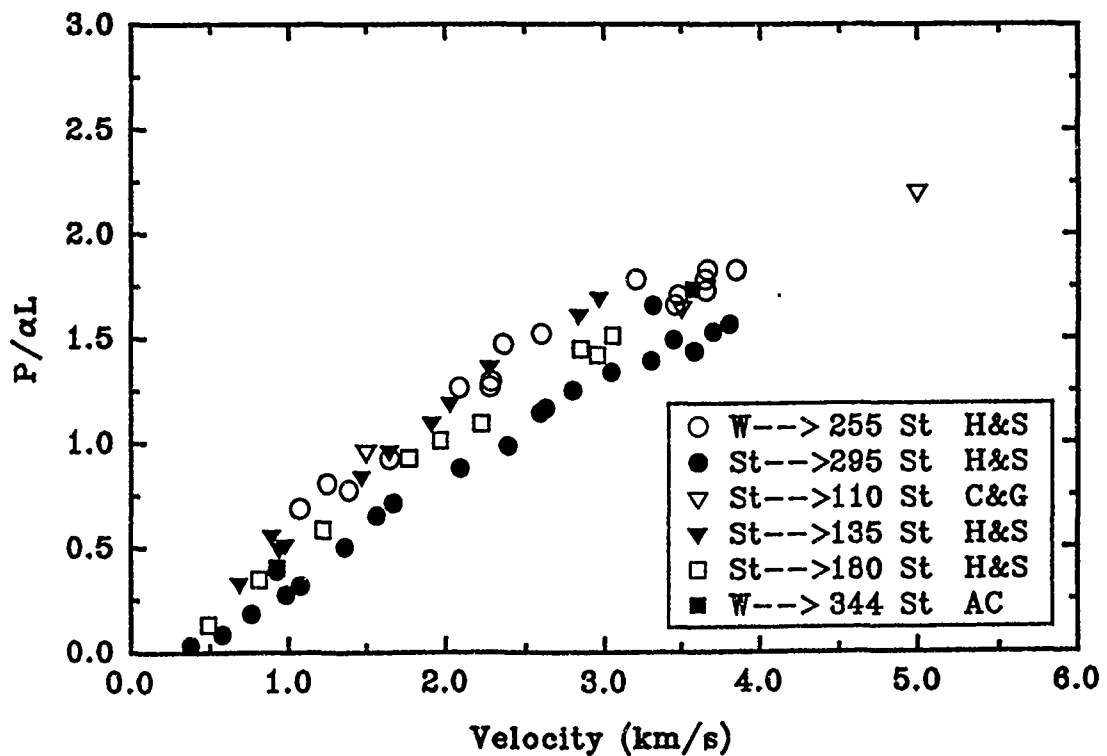


Figure 21. $P\alpha/L$ for $L/D = 1$ rods versus impact velocity.

We will demonstrate the ability to collapse these seemingly disparate data by considering the $L/D = 1$ projectiles. First, we note that the penetration limit for hydrodynamic flow is given by the density ratio $(\rho_p/\rho_t)^{1/2}$. To first order, the difference in penetration of tungsten-into-steel versus steel-into-steel can be accounted for by further normalizing the depth of penetration by this density ratio. $P/\alpha L$, where α is the square root of the density ratio, is plotted versus impact velocity in Fig. 21.

The next step is to account for target hardness. This is done by calculating the nondimensionalized impact velocity, with the flow stress given by: σ_c (GPa) = $3.48 \times 10^{-3} \cdot (BHN-11.24)$. The results are shown in Fig. 22. We have selected the exponent to be $1/3$ on this Π term since P/L varies as $V^{2/3}$ at hypervelocities [29]. The data have collapsed quite well into a common curve; however, there is some disparity in the tungsten-into-steel versus steel-into-steel data, suggesting that all of the density dependence has not been fully accounted for in the model.

We next let the abscissa be represented by the product of the nondimensionalized velocity and nondimensionalized density. A regression analysis was performed to determine the exponent for the nondimensional density term. This was found to be approximately -0.15 . The results are plotted in Fig. 23.

One last "adjustment" was made to a subset of the data. Christman and Gehring [25] used very soft targets in their experiments. In general, their data do not agree with the data of other researchers when the data are plotted in the nondimensional coordinates used here. If we assume that these very soft materials strain harden disproportionately to their initial flow stress, then a larger σ_c should be used in the denominator of the nondimensionalized velocity. The 110 BHN steel was changed to an effective 220 BHN steel; the arrows show the "movement" of the data points in Fig. 23, making these data much more consistent with the data for substantially harder targets.

Similar analyses were performed on the $L/D = 3$ and $L/D = 5 \& 6$ data. The same exponents found for the $L/D = 1$ case were used for the two Π terms in the abscissa. The final results are depicted in Figs. 24-25. Again, a "strength" adjustment was used on the very soft targets used by Christman and Gehring (110 BHN and 145 BHN steel were modified to become 220 BHN steel, and 25 BHN aluminum was modified to 50 BHN aluminum; all other hardness values were used as reported).

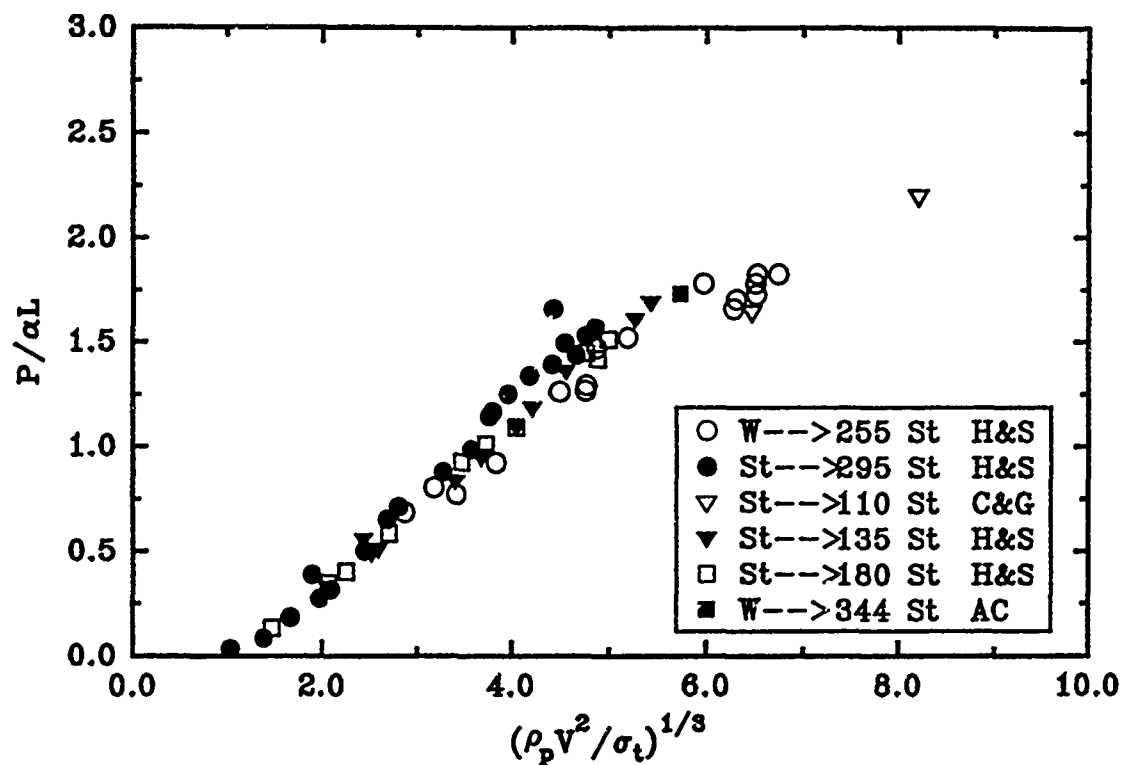


Figure 22. $P\alpha/L$ for $L/D = 1$ rods versus $\pi_1^{1/3}$.

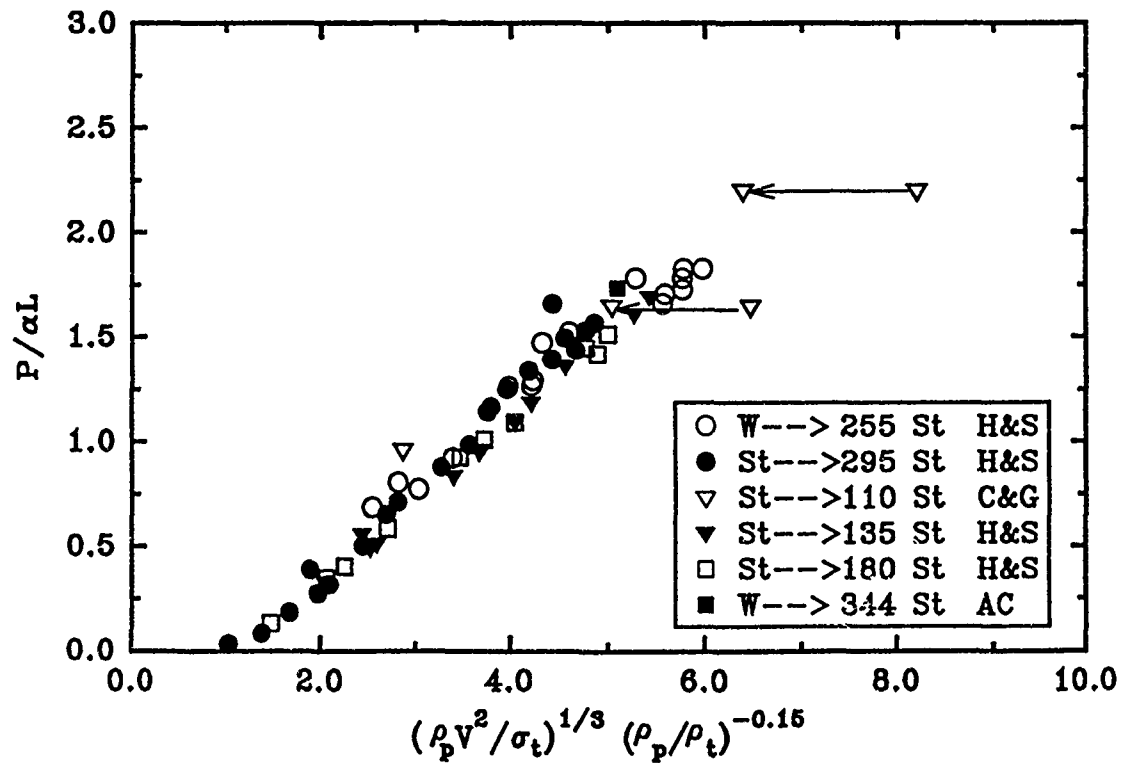


Figure 23. $P\alpha/L$ for $L/D = 1$ rods versus $\pi_1^{1/3} \pi_2^{-0.15}$.

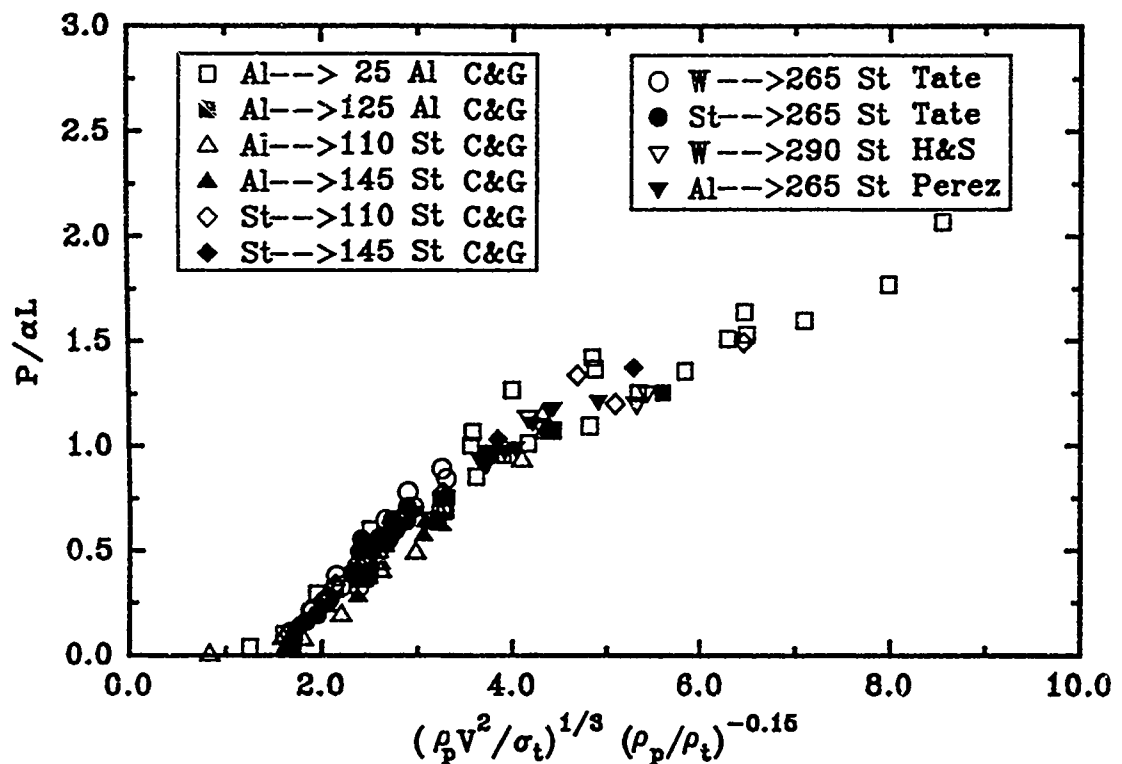


Figure 24. $P\alpha/L$ for $L/D = 3$ rods versus $\pi_1^{1/3} \pi_2^{-0.15}$.

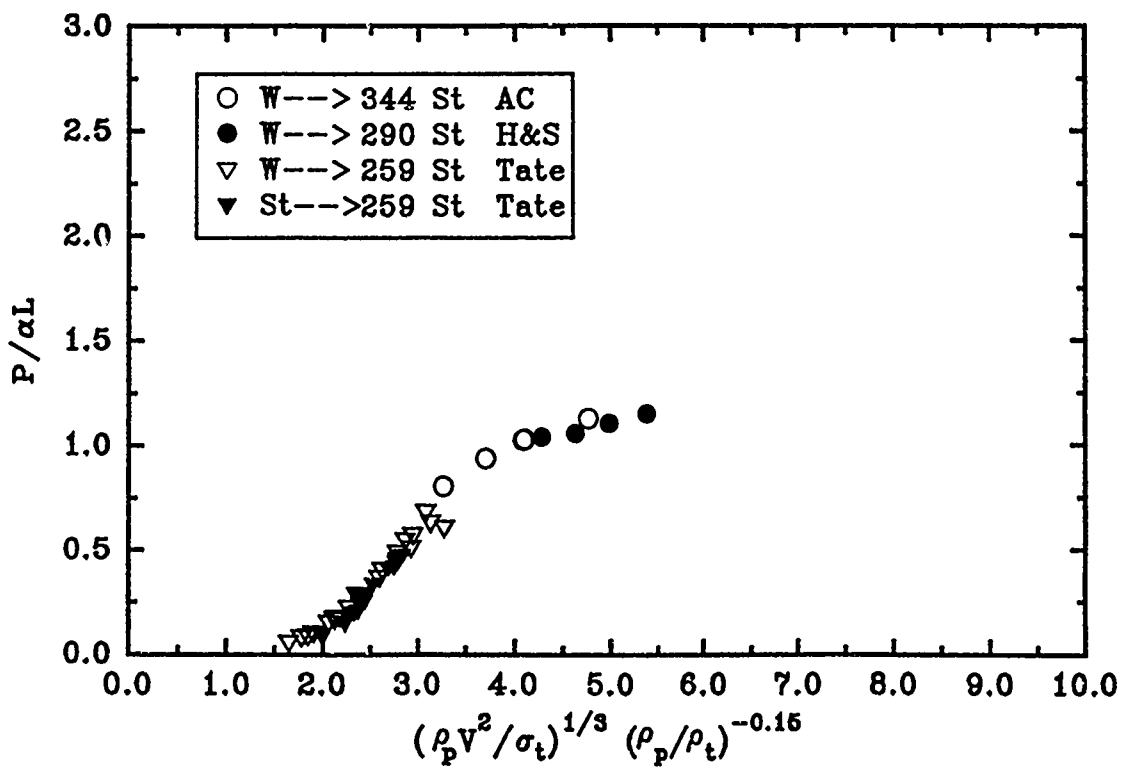


Figure 25. $P\alpha/L$ for $L/D = 5$ & 6 rods versus $\pi_1^{1/3} \pi_2^{-0.15}$.

4.3 Analysis

Two types of least squares regression fits were made to the data using the Pi terms of Figs. 23-25. First, a regression fit was done in order to represent the data over the entire parameter space (all impact velocities):

$$x \equiv \pi_1^{1/3} \pi_2^{-0.15} \equiv \left(\frac{\rho_p V^2}{\sigma_t} \right)^{1/3} \left(\frac{\rho_p}{\rho_t} \right)^{-0.15} \quad (16)$$

$$\frac{P}{\alpha L} = a + b x \quad (17)$$

$$\ln\left(\frac{P}{\alpha L}\right) = a + \frac{b}{x\sqrt{x}} \quad (18)$$

$$\ln\left(\frac{P}{\alpha L}\right) = a + b e^{-x} \quad (19)$$

The coefficients for the regression fits are summarized in Table 6; also given are the r^2 regression correlation coefficient for each curve fit and the standard error in estimating $P/\alpha L$. Secondly, linear least squares regressions, of the same form as the linear fit for $L/D = 1$ [Eqn. (17)], were performed in the nominally linear range of the data. The appropriate information, with limits of applicability, is also given in Table 6.

Table 6. Parameters for Regression Analysis of Penetration by Small L/D Projectiles

L/D	a	b	r^2	Eqn. No.	Standard Error	Limits of Applicability
1	-0.433	0.400	0.970	17	0.093	$1.0 \leq x \leq 7.0$
3	0.821	-6.277	0.964	18	0.080	$0.5 \leq x \leq 9.0$
3	-0.582	0.413	0.936	17	0.067	$1.5 \leq x \leq 4.0$
5&6	0.264	-16.59	0.985	19	0.041	$1.0 \leq x \leq 6.0$
5&6	-0.912	0.496	0.965	17	0.039	$1.9 \leq x \leq 4.0$

Computer simulations and the results from the six experiments discussed in Section 3.4 were used to investigate the applicability of the regression fits to estimate penetration performance as a function of impact velocity. The computer simulations were performed using the Eulerian wavecode CTH [4]. The depths of penetration for a right-circular, tungsten-alloy cylinder impacting RHA targets for different velocities and aspect ratios were computed. The initial conditions and results are summarized in Table 7.

The two experimental data points for depth of penetration into a witness pack (after first penetrating and perforating the 45.7-cm thick RHA target) are summarized in Table 4. In the other four experiments, Table 5, the witness pack was removed and orthogonal flash X-rays were employed to obtain the residual velocities and residual lengths of the projectiles. These experiments were averaged to provide estimates of L_r and V_r for the two experiments with the witness pack.

Table 7. Summary of Computational Results for Small L/D Projectiles

L/D (-)	V_r (km/s)	P/L (-)	$P/\alpha L$ (-)	$\pi_1^{1/3} \pi_2^{-0.15}$ (-)
1	1.3	1.143	0.772	2.848
1	1.5	1.320	0.892	3.138
1	1.8	1.500	1.013	3.538
1	3.0	2.228	1.498	4.974
3	1.3	0.977	0.660	2.848
3	1.5	1.130	0.763	3.138
3	1.8	1.383	0.935	3.538
3	3.0	1.754	1.185	4.974
5	1.3	0.872	0.589	2.848
6	1.5	1.000	0.676	3.138
5	1.8	1.283	0.867	3.538
5	3.0	1.644	1.111	4.974

The results of the experiments and the computations are plotted in Fig. 26. The results all lay within the data scatter. The point which deviates the most from the regression fits is the computed $L/D = 3, 3.0\text{-km/s}$ case. This point lays within the region of the $L/D = 3$ data where there exists large scatter in the data. At abscissa values greater than 5, the regression fit is controlled essentially by the soft (25 BHN) aluminum targets. We have already noted that the forming of the P_i terms using the reported strength of the very soft targets leads to results that are not consistent with the harder targets. Although using a *modified* value for the hardness appears to be consistent with other data at lower impact velocities, it may be that such a simple "first approach" is not adequate for the higher impact velocities. P/L for the two experimental data points appear to be well represented by the regression analysis.

4.4 Summary

Penetration performance has been plotted in terms of nondimensional expressions that were formed from an *a priori* knowledge of the physical parameters most important in determining depth of penetration into semi-infinite targets. We acknowledge that some other parameters that have been ignored—for example, projectile strength—do influence penetration performance; but in general, the effects that have been ignored can be considered second-order effects.

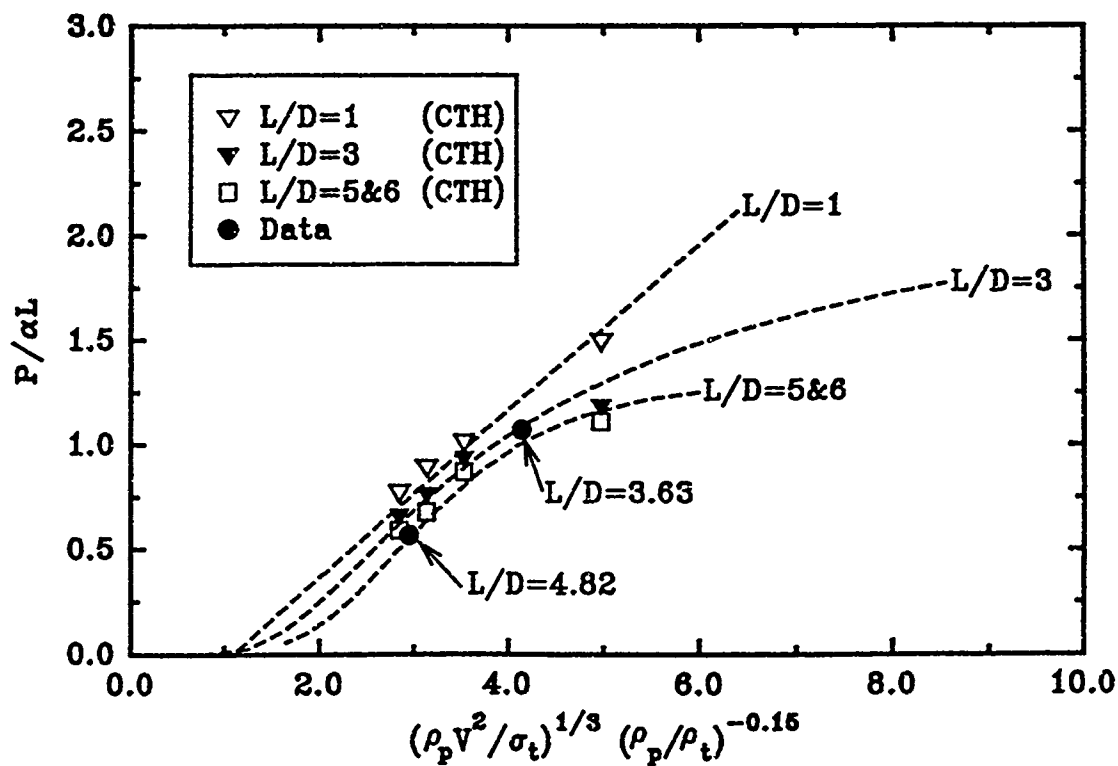


Figure 26. Comparison of computations and experiments with regression analyses.

An implicit assumption in the analysis is that the impact velocities are sufficiently large that erosion of the projectile occurs during penetration. The data for relatively low aspect ratio rods have been analyzed for a fairly wide range of target strengths, projectile densities, and impact velocities. Relatively good correlation has been obtained for $P/\alpha L$ in terms of $(\rho_p V^2 / \sigma_t)^{1/3} (\rho_p / \rho_t)^{-0.15}$, although it was shown that the flow stress of very soft targets needs to be increased somewhat in order to bring the results of soft targets into consistent agreement with harder targets. This approach was justified by noting that strain hardening (and perhaps strain-rate hardening) increases the strength of these very soft materials, relative to their initial strengths, considerably more than harder materials.

Finally, the results from numerical simulations and experiments were compared to regression fits of the nondimensionalized data. In general, these independent results agree within the data scatter. In particular, we note that the experimental results do not represent the performance of a pristine projectile; rather, the experimental results are for a rod that has undergone considerable erosion during penetration and perforation of a finite-thickness target before striking a witness pack. Although not unexpected, the good agreement demonstrates that the penetration performance of a residual projectile after perforation of a target can be estimated from independent experiments that begin with an undeformed and unstressed projectile of the appropriate length and impact velocity.

5.0 HIGH-HARD STEEL SPACED-PLATE TARGET

5.1 Target Description

The spaced-plate target is shown in Fig. 27. Six high-hard steel plates (MIL-A-45100D), each 1.90-cm thick, were positioned 2.54 cm apart at a 65° angle. A 7.62-cm thick gap separated the RHA witness pack and the last plate of the target. The witness pack was also inclined 65° as shown in Fig. 27.

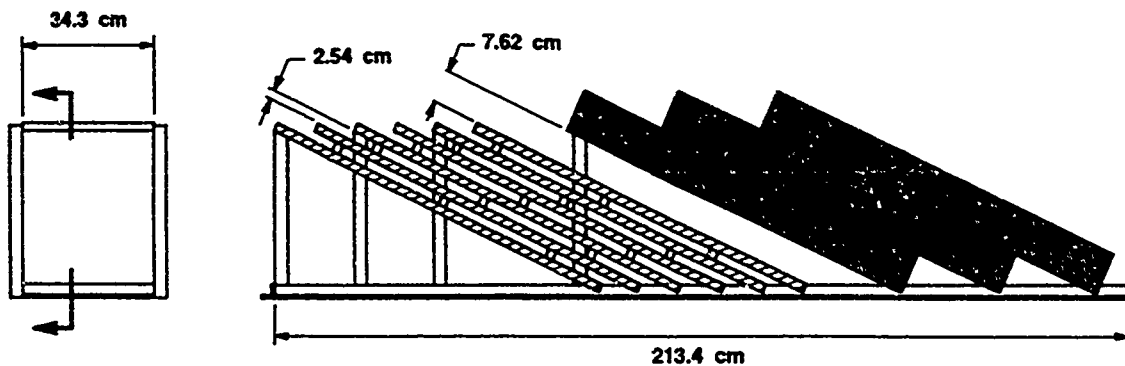


Figure 27. Schematic of the high-hard spaced-plate target array.

5.2 Numerical Simulations

The three-dimensional numerical simulation of the projectile interaction with the oblique, spaced-plate target array proved to be quite challenging because of the size of the problem. Six zones were used across the diameter of the projectile; square zoning was used in the interaction region. There is one plane of symmetry, so only one-half of the problem needed to be analyzed.⁶ Further, the geometric dimensions of the plates and the witness pack were decreased for the computational model to further reduce the "size" of the problem. Approximately one million computational cells were used to describe the problem geometry, and since 37 variables were stored for each computational cell, 38 MWords of memory were required. The problems were executed on the TACOM Cray 2 supercomputer system. Although the CRAY 2 has ample memory for better zonal resolution, CPU time was viewed as the limiting factor.⁷ The 2.600-km/s impact problem

⁶ The coordinate system used for the computations was defined as follows: the projectile traveled in the negative Y direction, and Z = 0 was the plane of symmetry.

⁷ Initially, the problem was configured with 10 zones across the diameter of the projectile. After 232 hours of CPU time, the problem had only gotten to 272 μ s (3467 integration time steps), and it was estimated that hundreds of additional CPU hours would be required to complete the problem. However, we did compare the results of the 6-zone and 10-zone problems up to 272 μ s, and the results compared favorably. That is, the 6-zone resolution appears to be numerically converged. For axisymmetric problems, 3 zones across the radius is not adequate for good numerical resolution; the volume of zones becomes larger with increasing radius in "square zoning" for axisymmetric problems. For 3-D problems, the zones are constant volume for "square zoning."

took 142-CPU hours (4142 integration time steps) to complete; the 1.775-km/s impact problem took considerably longer, 231-CPU hours (6103 integration time steps), because the projectile was longer and had a lower velocity.

The simulations permit insight into the experiments that could probably not have been obtained by any other means (i.e., direct measurements were not possible in the experiments because of geometric shadowing by the plates). Figure 28 shows the position along the centerline of the projectile nose and tail as a function of time for the two impact cases. The positions of the high-hard plates and the witness pack are also shown in the figure.* The nose position versus time has a somewhat "wavy" appearance, while the tail position versus time is approximately linear. These observations are readily explained by examining the nose and tail velocities versus position.

Before examining the velocities, it is meaningful to consider the pressure (mean stress) as a function of position, Fig. 29. In the figure, the pressure is taken at the projectile-target interface along the plane of symmetry. The interaction with the six plates and the witness pack are easily discernable. The initial penetration pressure for each plate is the nominal steady-state penetration pressure (this is concluded by observing the steady-state pressure in the witness pack). Because of the obliquity, the edge of the projectile impacts a plate before the centerline point on the nose arrives at the geometric location of the plate; thus, the steep increase in pressure occurs slightly before the "plate location" in the figures. But the pressure drops rapidly due to the bulging of the rear surface of a plate almost immediately after impact (the line-of-sight thickness is only 2.7 projectile diameters for the 1.775-km/s impact, and 3.5 D for the 2.600-km/s impact case).

The nose and tail velocities on the projectile centerline are shown with the solid and dotted lines, respectively, as a function of position in Figs. 30 and 31. The original positions of the plates and the witness pack are also depicted in this figure. For the low-velocity case, Fig. 30, the nose of the projectile is perforating the second steel plate about the time the first elastic deceleration wave arrives at the tail of the projectile. For the high-velocity case, Fig. 31, the projectile nose has impacted the third plate of the array before the tail "finds out" that there was an impact with the first target plate.

It is informative to examine "snapshots" in time of the projectile-target interaction. Figure 32 depicts the velocities of the projectile-target interface and tail (on the plane of symmetry) as a function of time. Figure 33 shows a series of snapshots that depicts material boundaries and pressure contours, approximately every 100 μ s, for the 1.775-km/s impact case; the times of the snapshots are denoted by arrows on Fig. 32. The figures show the XY-plane (the projectile is traveling in the negative Y-direction), along the plane of symmetry ($Z = 0$). The "snapshots" catch the projectile at various stages of penetration and perforation of the plates, and in Fig. 33d, it is seen that debris from a plate that is being penetrated is already interacting with a subsequent plate. The velocities versus time of the nose and tail for the 2.600-km/s impact case are shown in Fig. 34, and the snapshots in time are shown in Fig. 35. Although the velocities are different, the overall interactions are very similar.

* In all plots of position, the position refers to the projectile-target interface on the original projectile centerline.

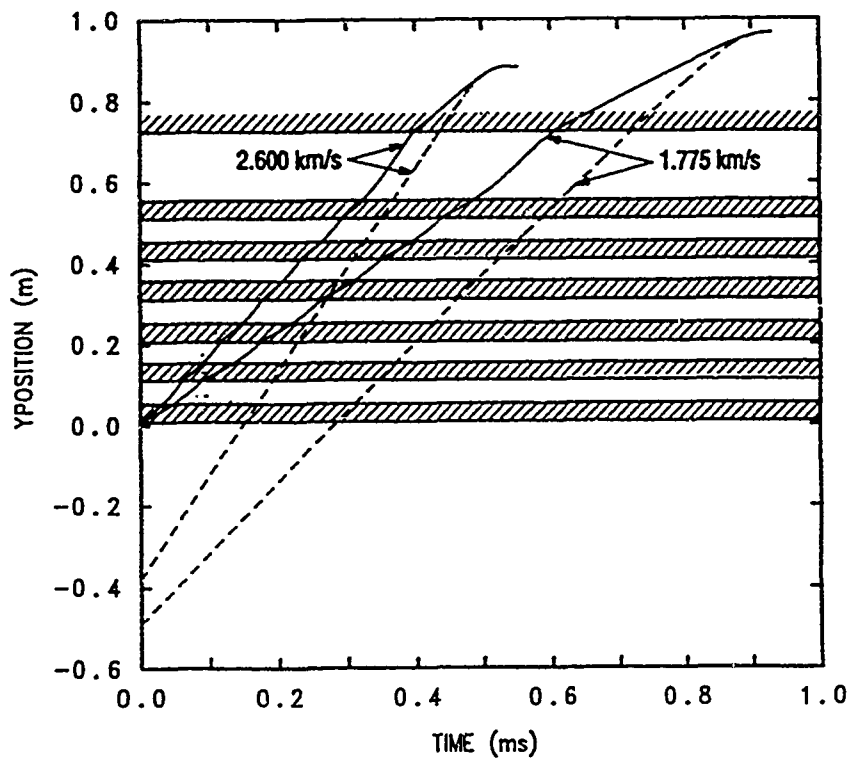


Figure 28. Nose and tail positions versus time, spaced-plate target—CTH results.

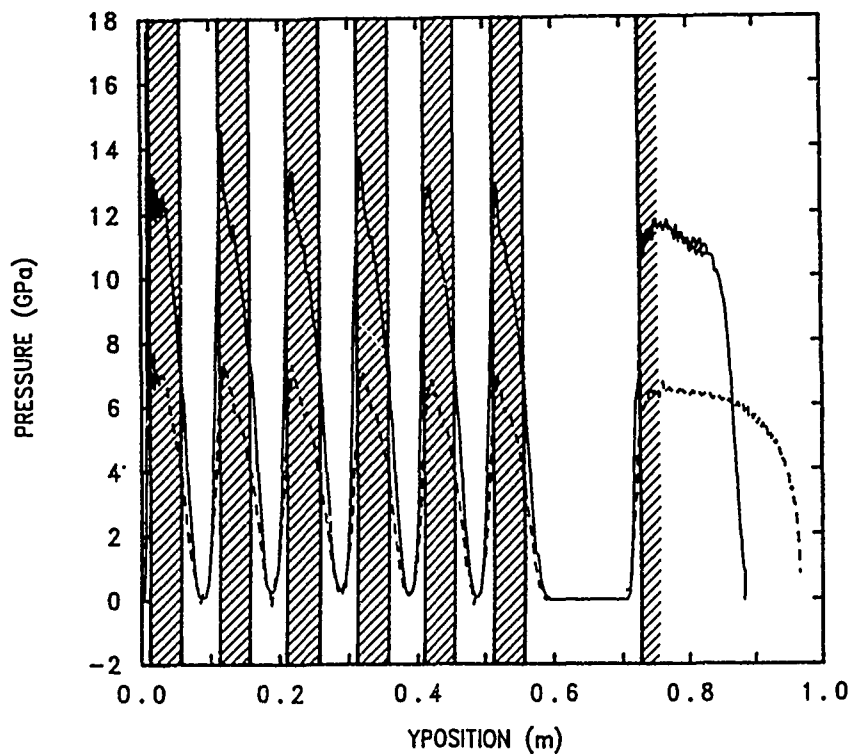


Figure 29. Centerline penetration pressure versus penetration position, spaced-plate target—CTH results (solid line represents the 2.600-km/s impact; dashed line represents the 1.775-km/s impact).

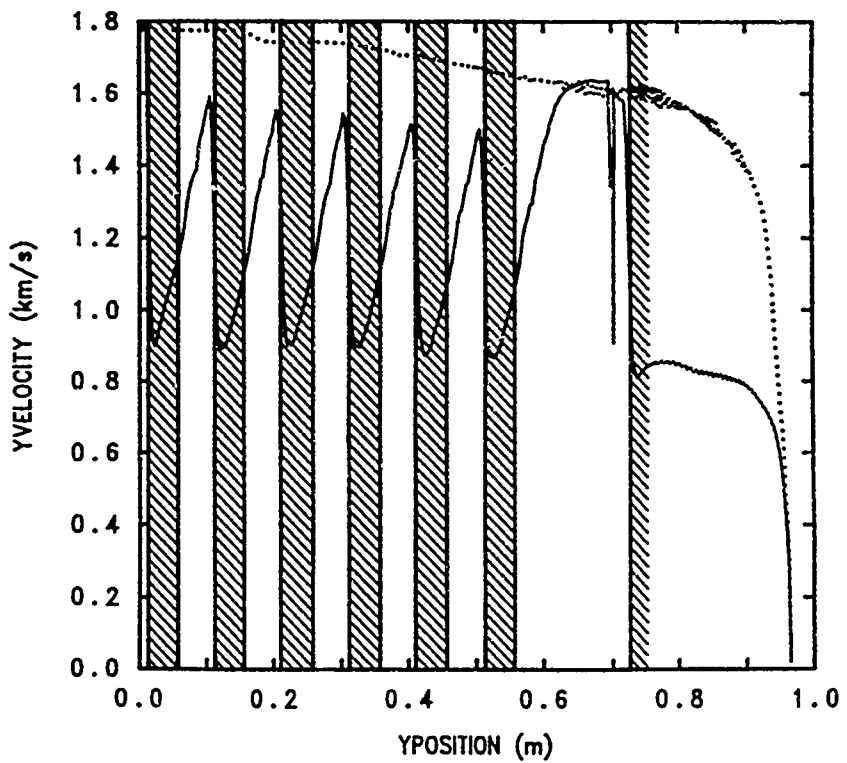


Figure 30. Nose (penetration) and tail velocities versus penetration position, spaced-plate target, $V_p = 1.775$ km/s—CTH results.

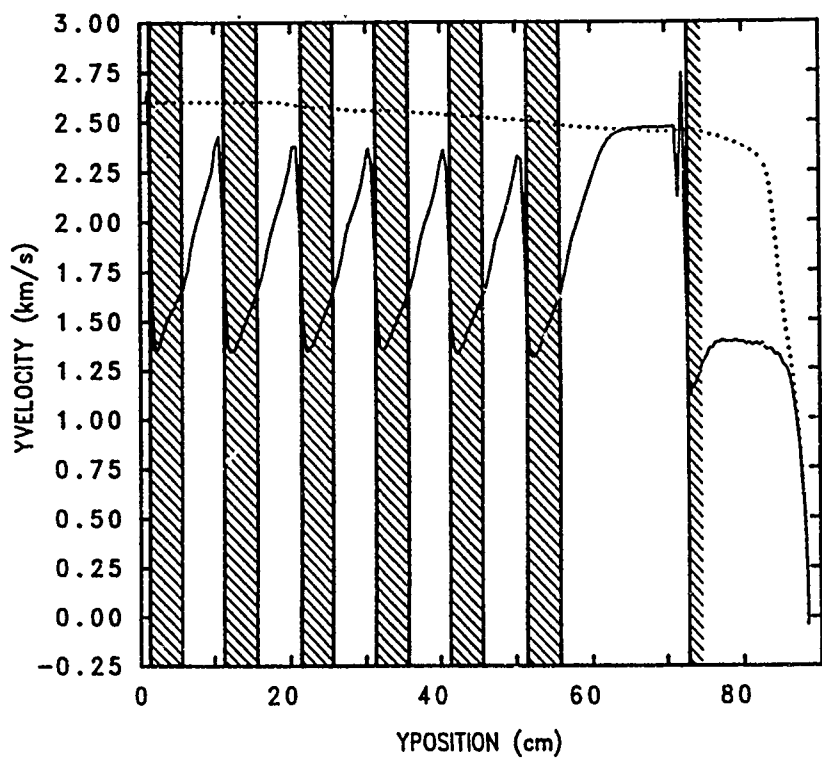


Figure 31. Nose (penetration) and tail velocities versus penetration position, spaced-plate target, $V_p = 2.600$ km/s—CTH results.

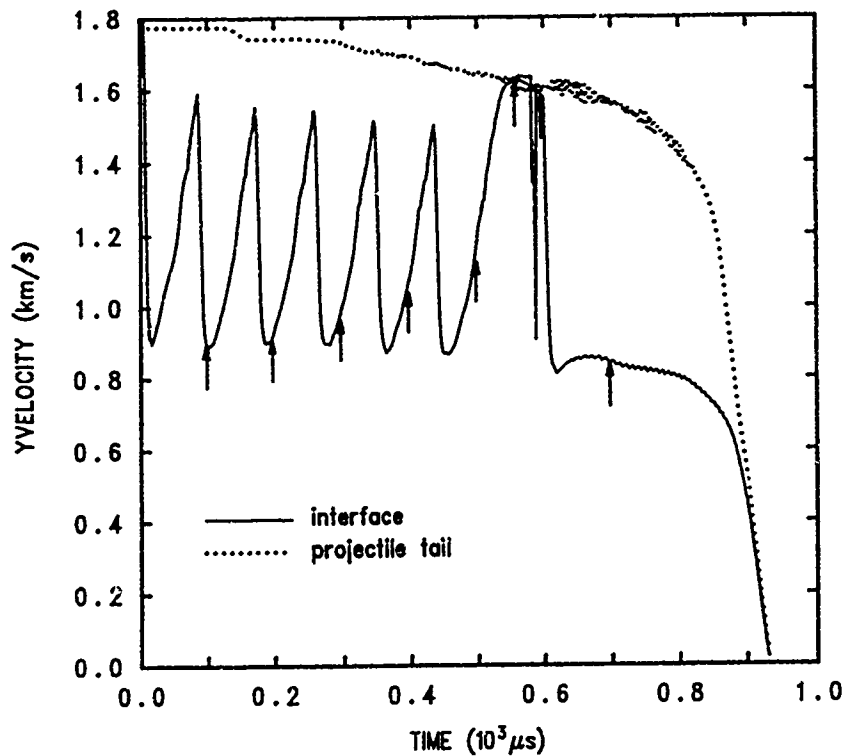
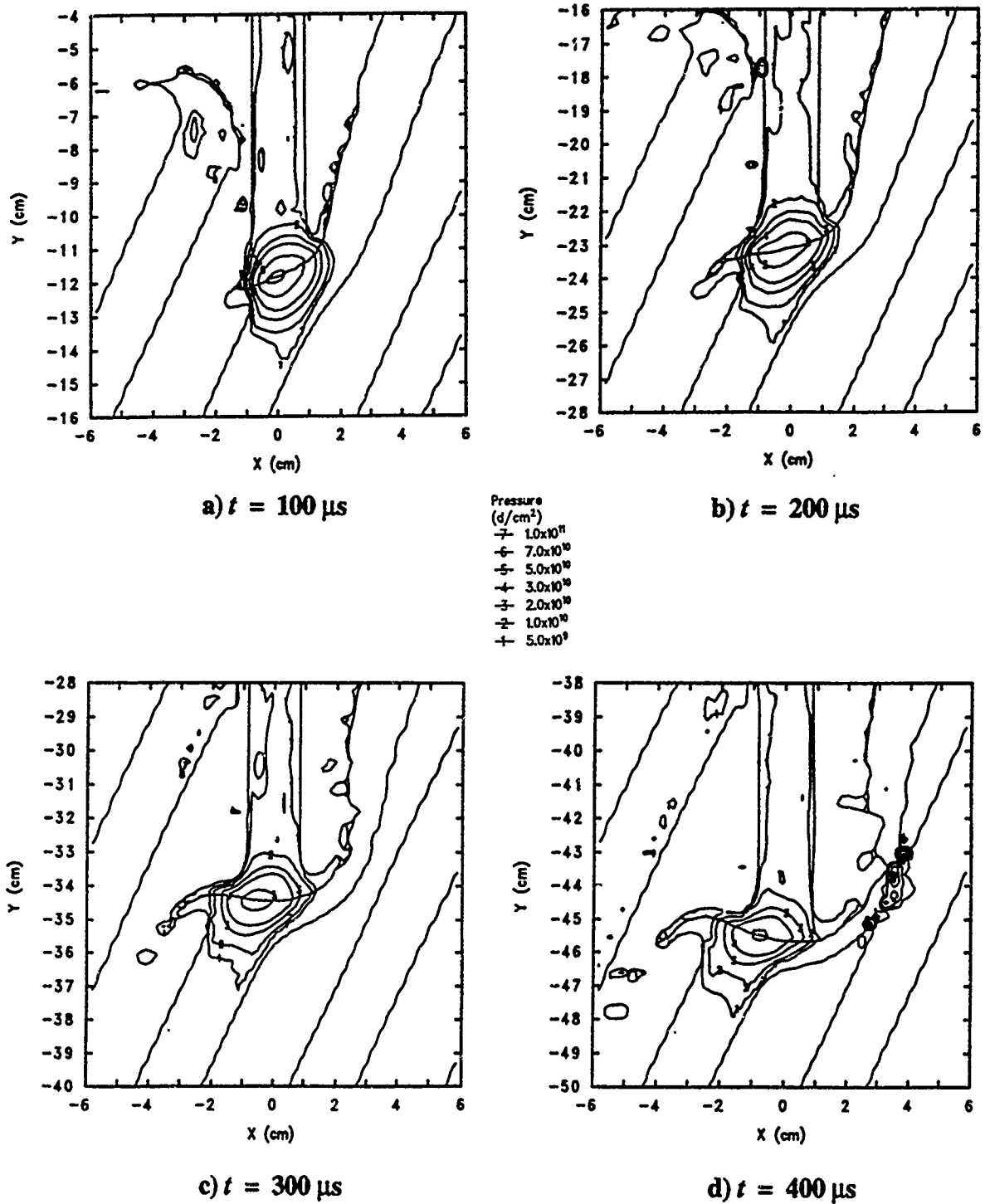


Figure 32. Nose (penetration) and tail velocities versus time, spaced-plate target, $V_p = 1.775$ km/s—CTH results.

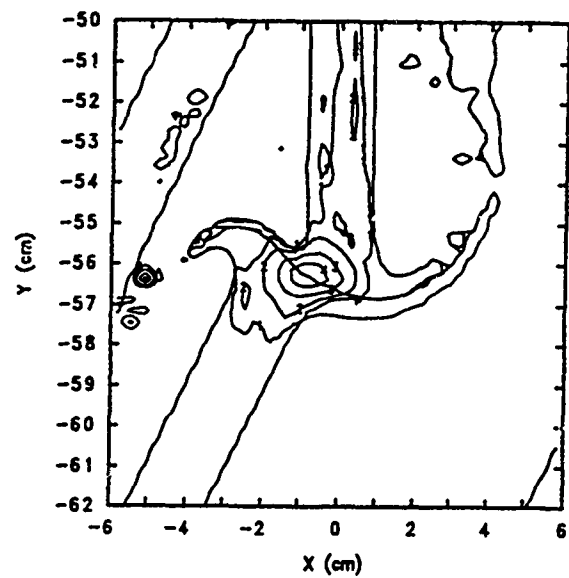
Figures 36 and 37 provide a series of 3-D perspective plots of the projectiles and the spaced-plate array. The 1.775-km/s impact case is shown at five different times in Fig. 36, and the 2.600-km/s impact case is shown at three times in Fig. 37. Analysis of the results depicted in these figures indicates that projectile performance should be sensitive to projectile pitch because the projectile would "wipe" the sides of the holes in the plates, for example, see Figs. 36b and 36c. Figure 36d, and the enlarged view of Fig. 36e, show the deformation of the nose of the rod after perforation of the last plate (also see Fig. 33f). Except for the nose, the rod is fairly straight. However, it is evident in Fig. 36e (also Fig. 33h) that the stresses within the rod have caused it to bend.

Figure 38 shows a plane view of the plates and witness pack for the XY plane with $Z \approx 0$ (the plane of symmetry), and the YZ plane with $X \approx 0$. Figure 39 depicts the YZ plane for various values of X to the left and right of the original projectile centerline $X = 0$ (see Figs. 33 or 35 for reference). The asymmetry of the holes, the result of plate obliquity and plate interactions during penetration, is quite evident.

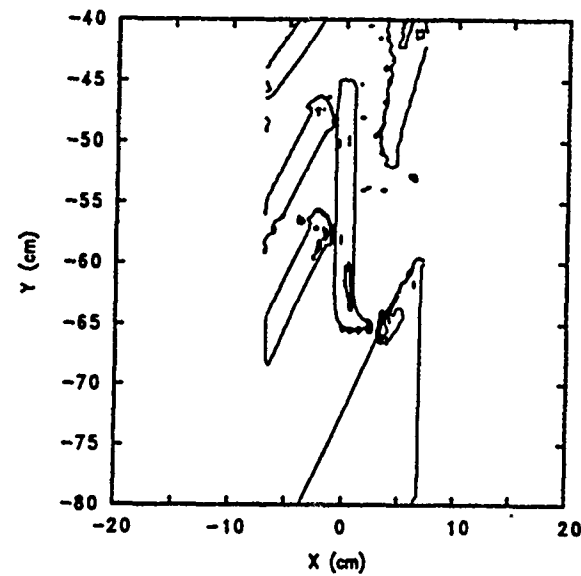
Because the plate spacing is relatively close, the nose and tail of the projectile are not able to equilibrate in velocity before the nose of the projectile impacts the next plate of the target array, Figs. 30 and 31. However, the spacing between the sixth plate and the witness pack is sufficiently large that the projectile nose and tail velocities equilibrate to 1.60 km/s and 2.45 km/s, respectively, for the two cases before impact with the witness pack. Within the witness pack, the projectiles achieve a quasi-steady-state penetration velocity until the final deceleration phase.



**Figure 33. Material boundaries and pressure contours,
spaced-plate target: $V_p = 1.775 \text{ km/s}$**



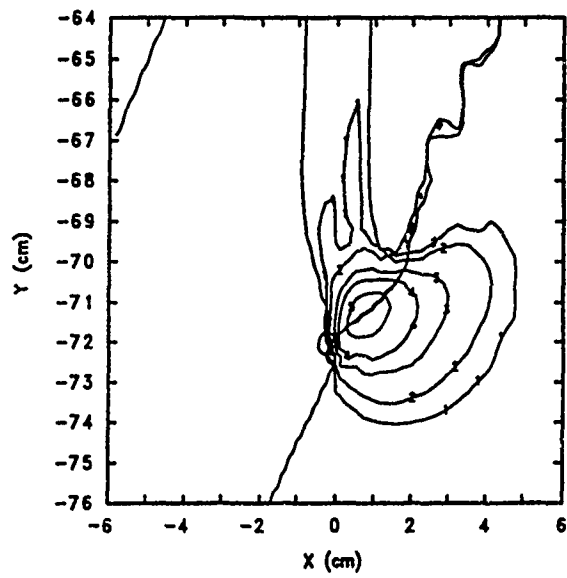
e) $t = 500 \mu\text{s}$



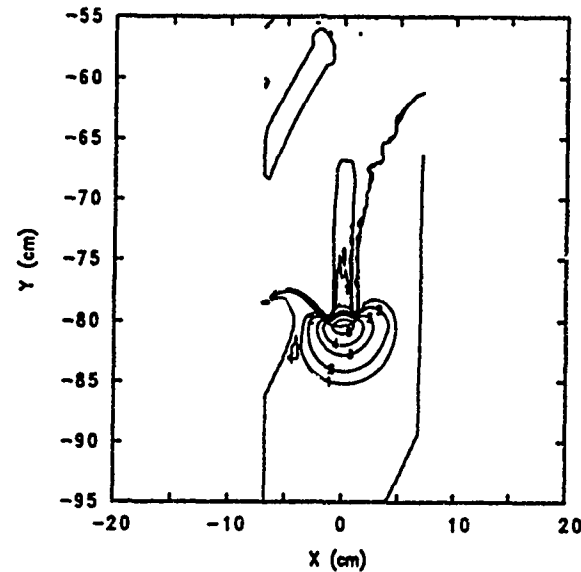
f) $t = 562 \mu\text{s}$

Pressure
(d/cm^2)

- 1.0×10^{11}
- 7.0×10^{10}
- 5.0×10^{10}
- 3.0×10^{10}
- 2.0×10^{10}
- 1.0×10^{10}
- 5.0×10^9



g) $t = 600 \mu\text{s}$



h) $t = 700 \mu\text{s}$

Figure 33. Material boundaries and pressure contours,
spaced-plate target: $V_p = 1.775 \text{ km/s}$ (Cont'd)

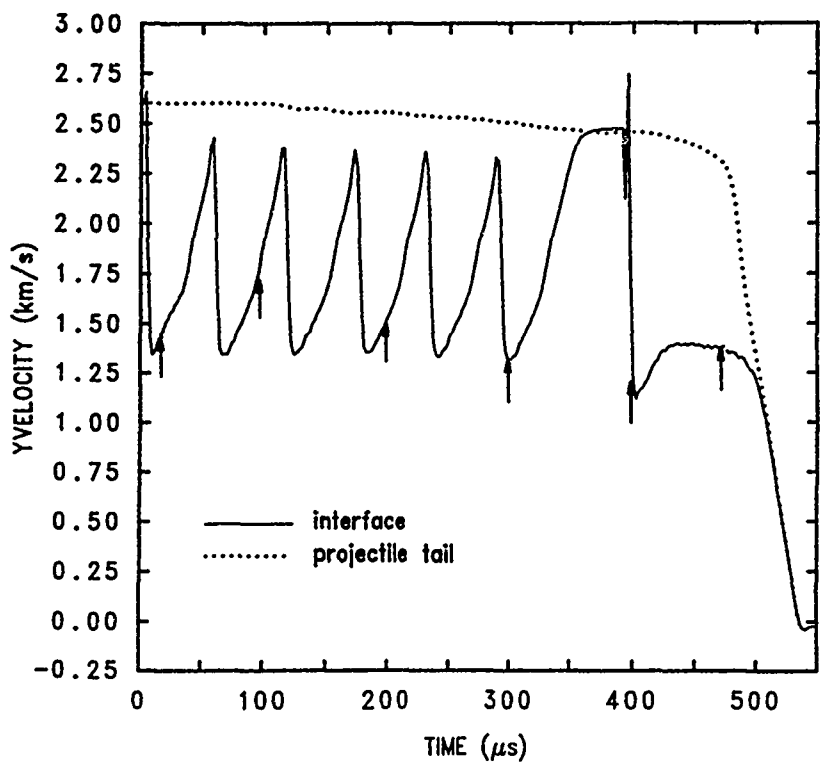


Figure 34. Nose (penetration) and tail velocities versus time, spaced-plate target, $V_p = 2.600$ km/s—CTH results.

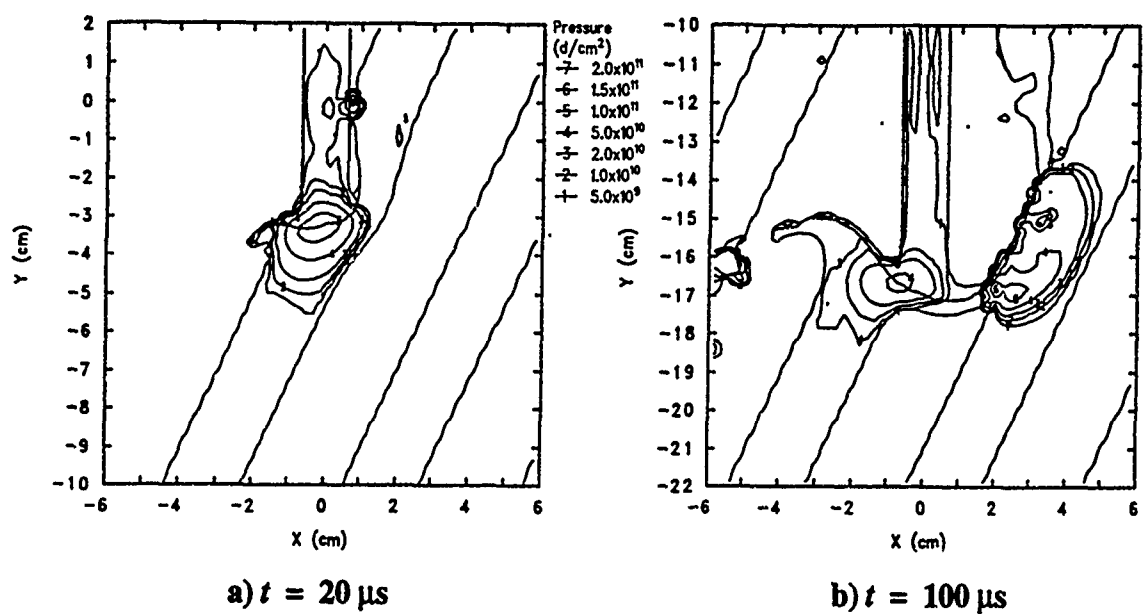


Figure 35. Material boundaries and pressure contours, spaced-plate target: $V_p = 2.600 \text{ km/s}$

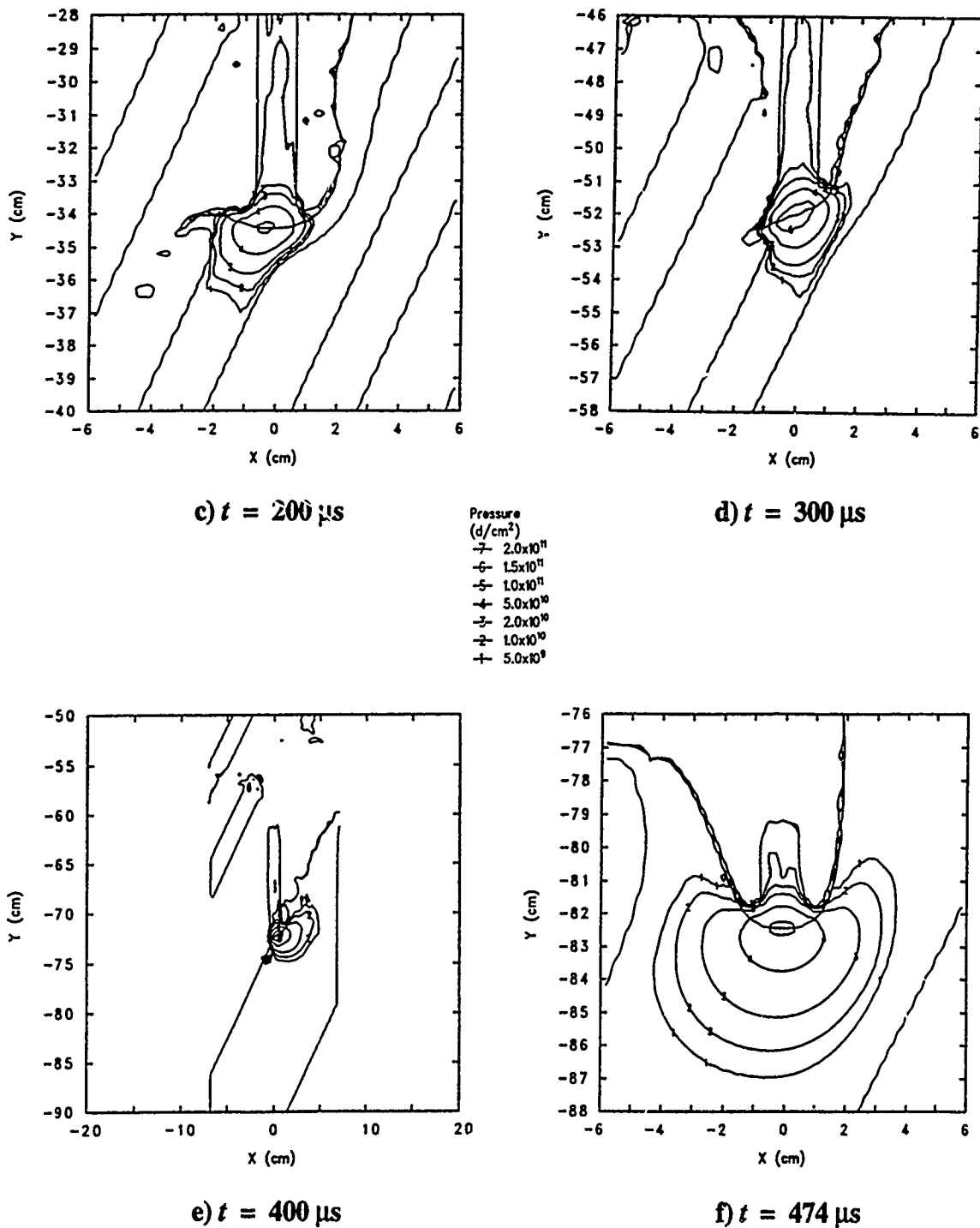


Figure 35. Material boundaries and pressure contours,
spaced-plate target: $V_p = 2.600 \text{ km/s}$ (Cont'd)

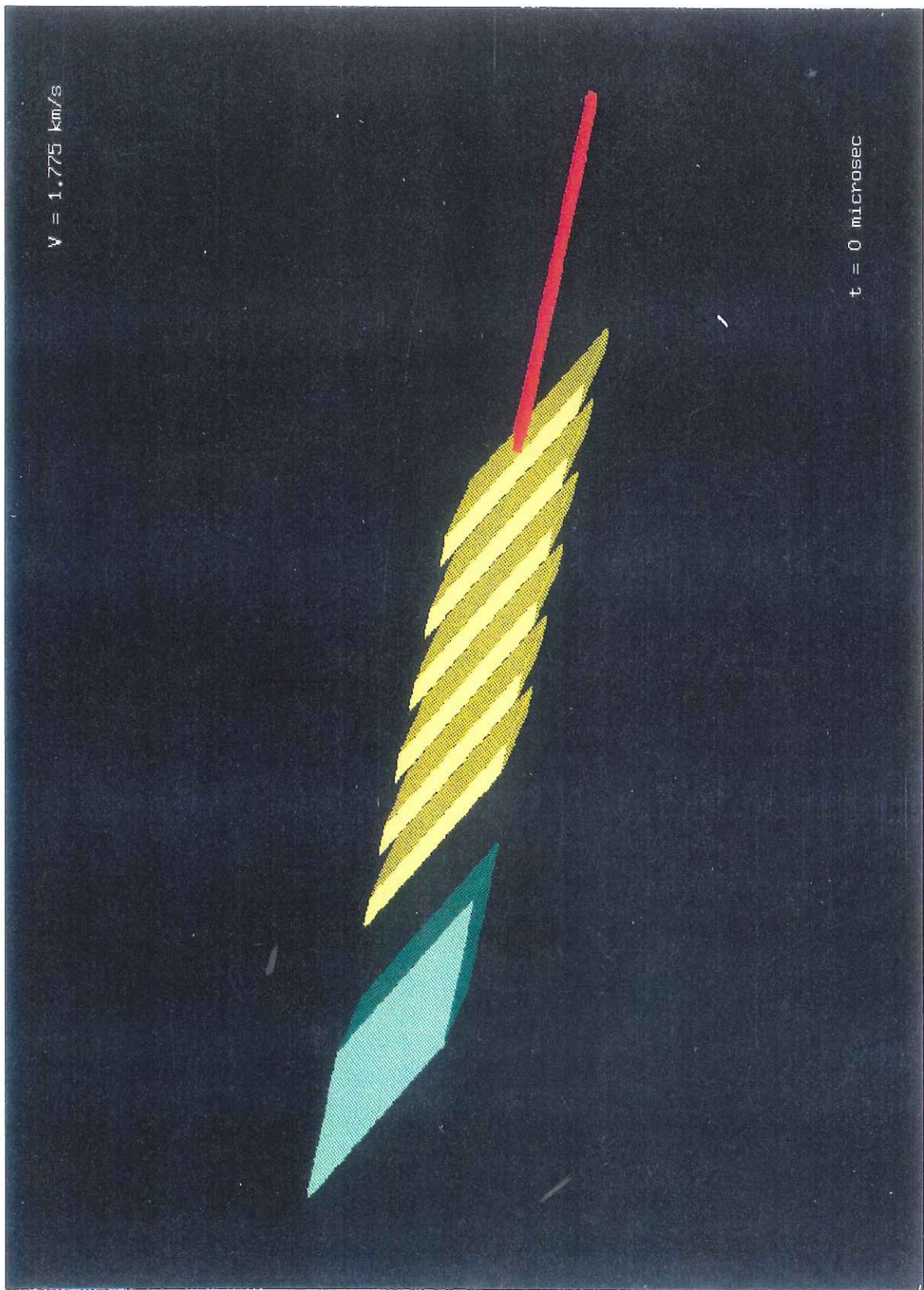


Figure 36. 3-D views of projectile-target interaction: $V_p = 1.775 \text{ km/s}$.
a) $t = 0 \mu\text{s}$

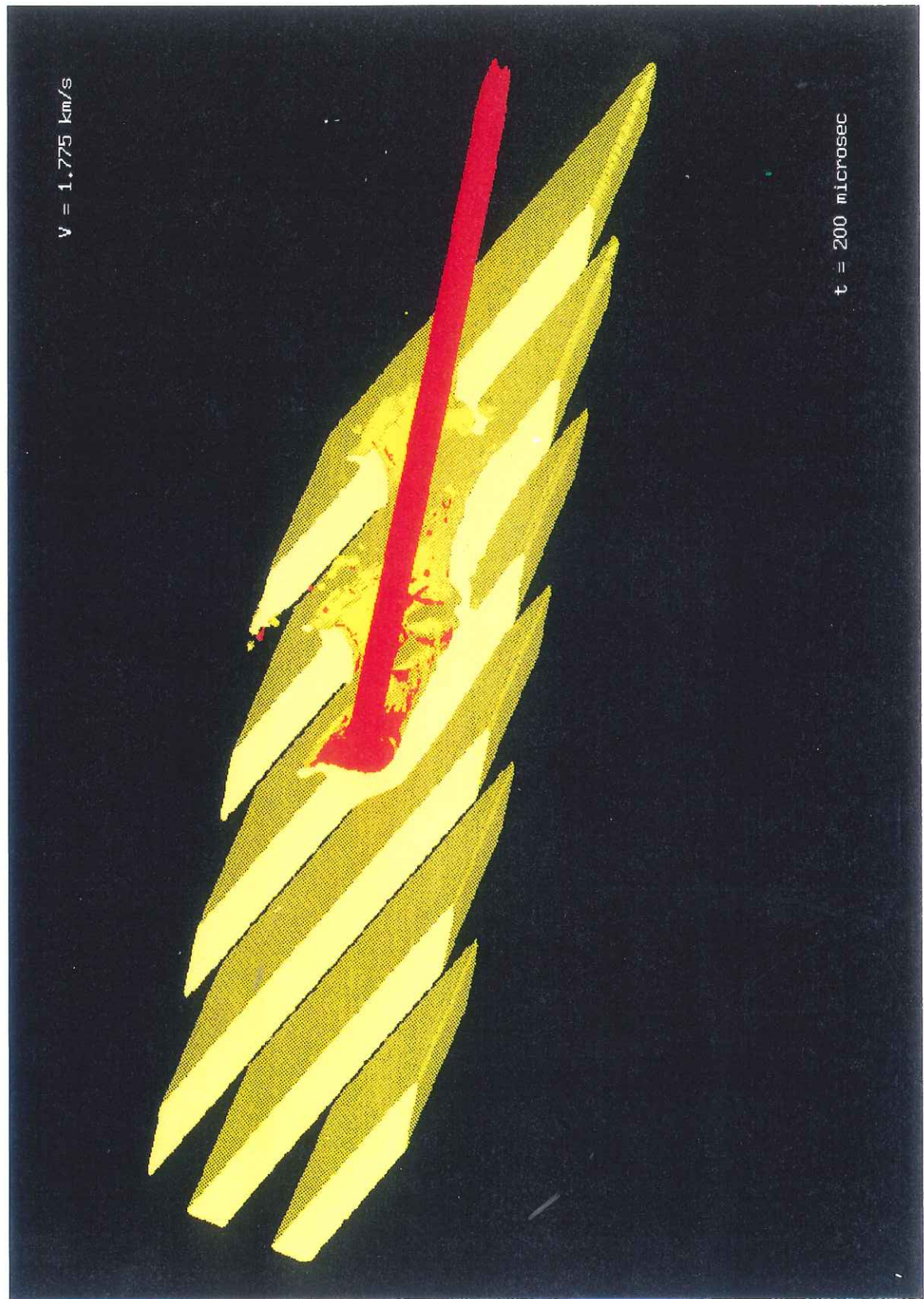


Figure 36. 3-D views of projectile-target interaction: $V_p = 1.775 \text{ km/s}$.
b) $t = 200 \mu\text{s}$



Figure 36. 3-D views of projectile-target interaction: $V_p = 1.775 \text{ km/s}$.
c) $t = 400 \mu\text{s}$

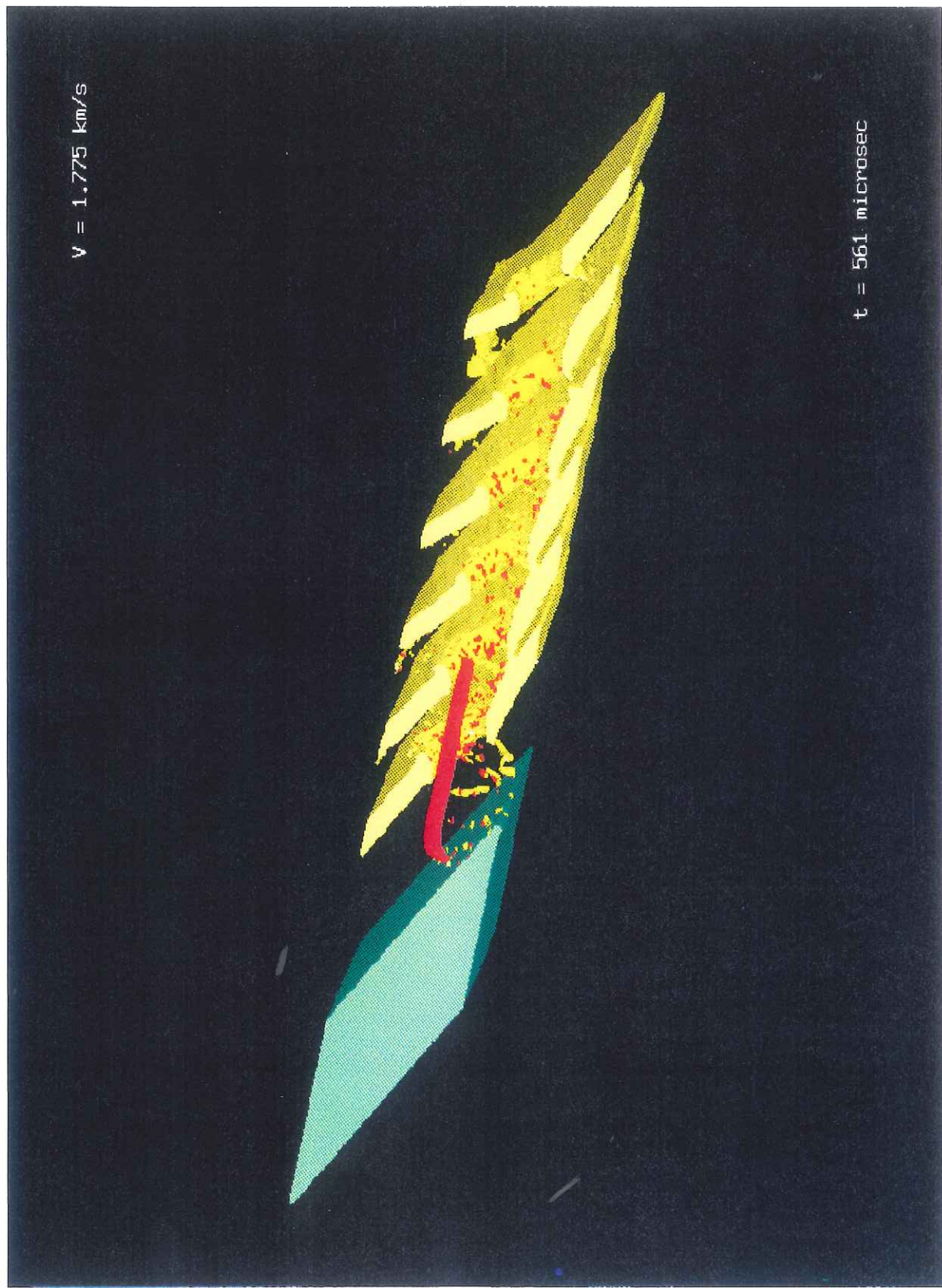


Figure 36. 3-D views of projectile-target interaction: $V_p = 1.775 \text{ km/s}$.
d) $t = 561 \mu\text{s}$



Figure 36. 3-D views of projectile-target interaction: $V_p = 1.775 \text{ km/s}$.
e) $t = 561 \mu\text{s}$ (enlarged view)



Figure 36. 3-D views of projectile-target interaction: $V_p = 1.775 \text{ km/s}$.
f) $t = 742 \mu\text{s}$



Figure 37. 3-D views of projectile-target interaction: $V_p = 2.600 \text{ km/s}$.
a) $t = 200 \mu\text{s}$



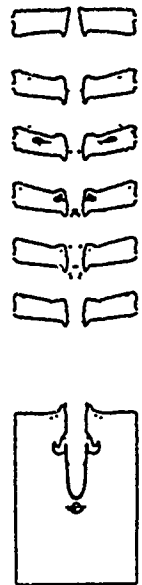
Figure 37. 3-D views of projectile-target interaction: $V_p = 2.600 \text{ km/s}$.
b) $t = 400 \mu\text{s}$



Figure 37. 3-D views of projectile-target interaction: $V_p = 2.600 \text{ km/s}$.
c) $t = 550 \mu\text{s}$



XY - Plane **Z = 0**



YZ - Plane **X = 0**

Figure 38. XY-plane, Z = 0; and YZ-plane, X = 0, view of plates and witness pack, spaced-plate target, $V_p = 2.600$ km/s.

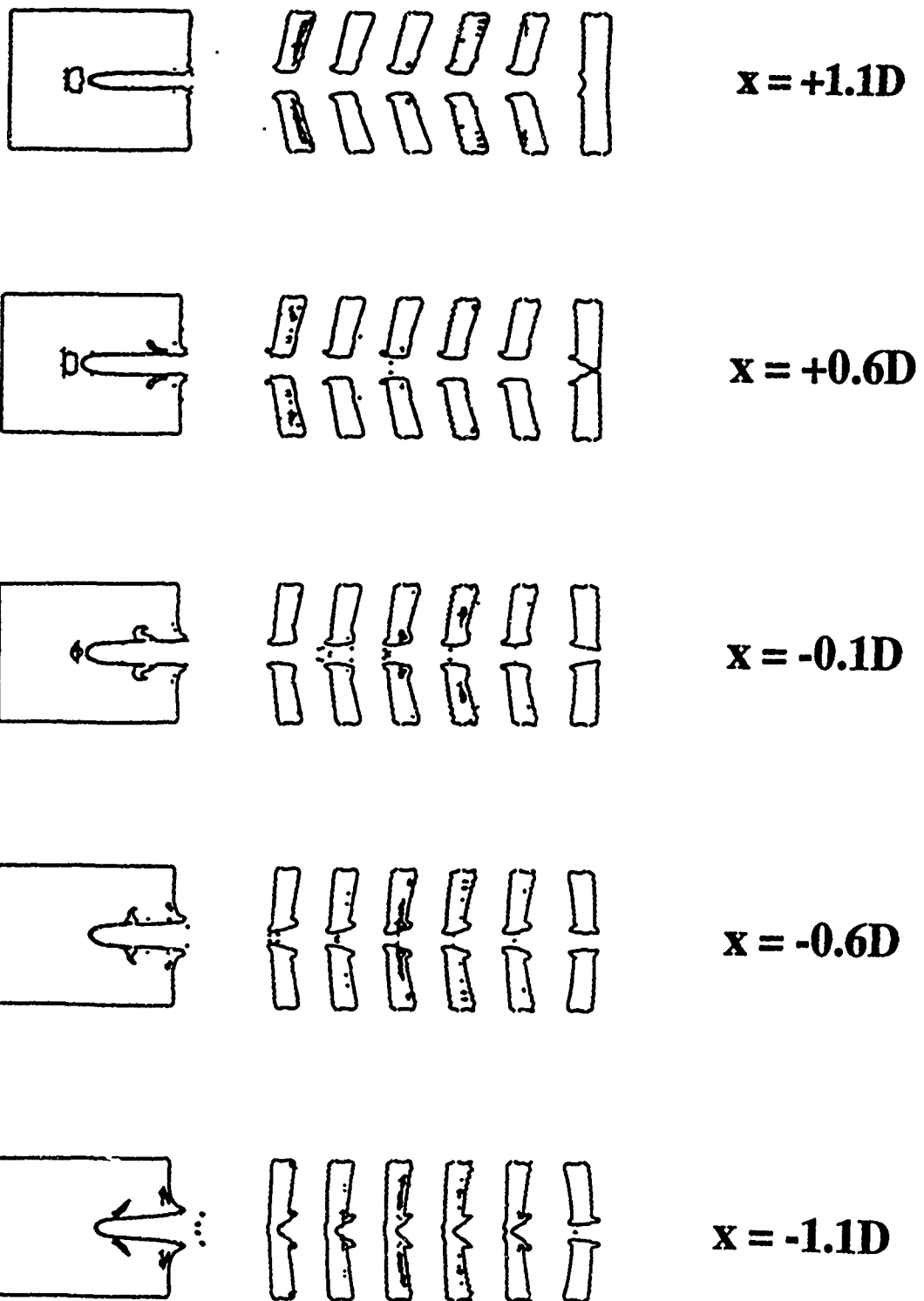


Figure 39. YZ-plane, various X's, view of plates and witness pack, spaced-plate target, $V_p = 2.600$ km/s.

For the 1.775-km/s impact case, the projectile has a length of approximately 19 cm ($L/D = 11.5$) after it perforates the sixth plate (and before striking the witness pack). Although approximately two-thirds of the projectile has eroded, the velocity of the residual rod has decreased only by 10% to approximately 1.60 km/s (Fig. 30). The line-of-sight depth of penetration into the witness pack is 21.3 cm. A correction to this value, and the reason for a correction, is given in Section 5.4

For the 2.600-km/s impact case, the projectile has a length of approximately 9.6 cm ($L/D = 7.5$) after it perforates the sixth plate (and before striking the witness pack). The residual rod has a velocity of approximately 2.45 km/s (from Fig. 31). The line-of-sight depth of penetration into the witness pack is 15.6 cm. A correction to this depth of penetration is also given in Section 5.4.

The lengths of the projectiles, normalized by their respective diameters, are shown in Fig. 40. Unlike the RHA target, Fig. 12, where there exists a comparable erosion rate per unit of penetration (after initial penetration) for both projectiles, it is observed that for the spaced-plate array the hypervelocity projectile "erodes" faster per unit of penetration than the super-ordnance velocity projectile. That is, the L/D curves are diverging in Fig. 40. Further, it is also seen that the projectiles continue to shorten after they have passed the geometric location of the back of each plate, similar to the breakout of the rear surface of the RHA target. Although the hypervelocity projectile impacts the witness pack with 0.85 km/s higher velocity than the super-ordnance velocity projectile, there is sufficient disparity in the lengths of the projectiles ($7.5D$ versus $11.5D$) that the penetration into the witness pack is considerably different. The results of Figs. 12 and 40 suggest that the impact and breakout phases are responsible for the different "erosion rates" of the two projectiles. The cumulative effect of six impacts and breakouts leads to significantly different residual L/D 's before impact with the witness pack.⁹

5.3 Analytical Predictions

The analytical models account for obliquity effects by increasing the plate thicknesses to the line-of-sight-thickness. The line-of-sight thickness of the plates is approximately 3 projectile diameters; in this sense, the plates are relatively thin. The velocity and length of the projectile after perforation of a plate were used for the impact conditions for the next plate. It was assumed that the projectile immediately equilibrates upon perforation of a plate. Additionally, the models do not account for any plate interactions, i.e., the application of the MITI and Walker-Anderson models assumed that the penetration and perforation of each plate could be modeled independently, and the resultant penetration history then consisted of the sum of the penetration/perforations of each plate. A value of 1.8 GPa was used for the dynamic flow stress for the high-hard steel plates. This value is commensurate with the values obtained from the Johnson-Cook model when dynamic effects are included.

⁹ For the RHA target, the projectiles have slightly different residual L/D 's at impact with the witness pack, with the hypervelocity rod having a slightly smaller L/D . Besides the difference in the impact velocity with the witness plate, the hypervelocity rod gets a little extra penetration because there is complete erosion of the projectile. The result is that the two residual projectiles have essentially the same penetration into the witness pack for the RHA target at these impact velocities. In contrast, the L/D 's of the residual projectiles for the spaced-plate target are considerably more disparate than for the RHA target; thus, the final depths of penetration are different.

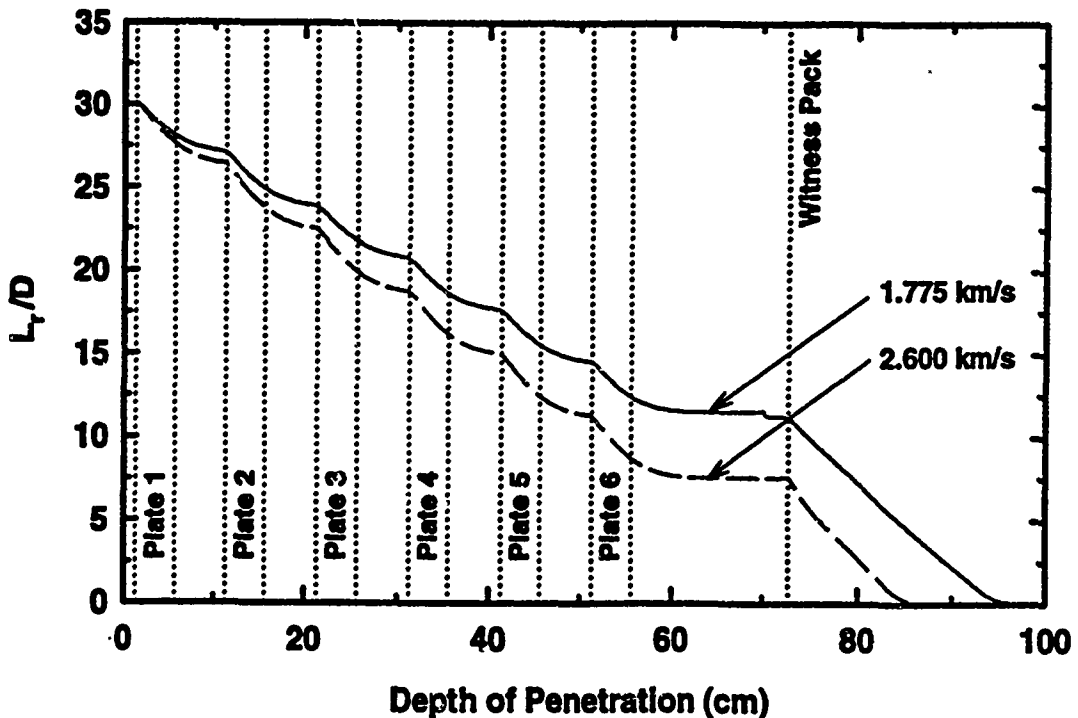


Figure 40. Normalized projectile length versus penetration position, spaced-plate target—CTH results.

The MITI model was applied as developed, with no modifications. A different approach was taken with the Walker-Anderson model. Hohler and Stilp [14] have observed that the front end of the rod is extremely distorted (bent, fractured) after impact and perforation of a 60° oblique plate. The deformed nose bends away from the shotline and in a direction perpendicular to the plate surface, e.g., see the inset in Fig. 80 of Ref. [14]. Additionally, computational modeling of long-rod eroding penetration shows that only 1.5-2.0 diameters of the projectile flows plastically [12]. A reasonable engineering judgement was made that some portion of the nose would be lost before the projectile struck the next plate. In effect, it was postulated that the large stresses and severe deformation result in failure of nose material and this material no longer is integral to the remainder of the projectile. It was decided that after perforation of each plate, a portion of the projectile would be discarded. This new length would then be used for the starting length in impacting a subsequent plate. To assess differences in this assumption, two cases were investigated. First, it was assumed that 1.5 diameters (1.5D) of the rod was lost due to the obliquity effect. The second case assumed that 1.8D of the rod was lost after each plate perforation.¹⁰

¹⁰ This assumption could also have been applied to the MITI model. However, it had already been demonstrated that the MITI model and the Walker-Anderson model gave essentially the same results for the RHA target. It was decided that the MITI model would be applied "as is," with no modifications.

The positions versus time of the nose and tail of the projectiles from the Walker-Anderson model are shown in Fig. 41. In plotting the results, the line-of-sight distance between the plates is divided by the "equilibrated" projectile velocity to estimate the time of impact with the next plate. The overall effect is very similar to Fig. 28, although the assumption of velocity equilibration in the analytical model results in the tail positions versus time in Fig. 41 to exhibit a "wavy" appearance that is not observed in the numerical simulations. The normalized lengths of the projectiles as a function of penetration position are shown in Fig. 42. The assumption of discarding 1.5D of projectile after each plate is explicitly shown in the figure by the sudden decrease in mass at the backside of each plate. If this length was "discarded" uniformly during the flight between the plates, the curves in Fig. 42 would be considerably smoother and would have been more similar to Fig. 40. The results for discarding 1.8D of projectile after perforation of each plate look very similar to Figs. 41-42, and are not reproduced here; however, the results are summarized in Section 5.5.

5.4 Corrections to the 3-D Computations

It was mentioned previously that the lateral extent of the plates and witness pack were made smaller than the actual target to minimize the size of the computational problem. Although diminishing the lateral extent of the plates probably did not affect the penetration solution (because the projectile perforates a plate before edge effects can significantly influence the problem), the witness plate bulged on the sides and back in the computational results. A projectile penetrates deeper into a target that bulges, due to less confinement, than for a target that does not bulge. Therefore, the dimensions used for the witness pack in the 3-D computations result in the residual projectile penetrating deeper into the witness pack than would be expected in the actual experiment.

It was decided to perform several two-dimensional, cylindrically symmetric simulations, using the length and velocity of the residual projectiles just prior to impact with the witness pack, to estimate the effect of bulging that occurred in the 3-D simulations. The differences in penetration depths between full and partial confinement were then used to estimate corrections for the 3-D results.

There were two important issues that had to be resolved to use the results of 2-D simulations to adjust the depths of penetration in the 3-D problems. First, the comparable zoning for the 2-D axisymmetric problem to provide the equivalent 3-D resolution (since the zone volumes are different in 2-D axisymmetric and 3-D simulations) had to be determined. Second, the equivalent radius of the underconfined target in the 2-D axisymmetric geometry that gave equivalent 3-D confinement had to be specified (since the length and width of the target plates are both variables in the 3-D simulation). After some initial numerical experiments, it was decided that the appropriate 2-D zonal resolution was seven zones across the projectile radius (compared to three zones in the 3-D simulation), and an applicable target radius was 7 cm (compared to a minimum plate dimension of 6.78 cm in the 3-D simulations).

Results from the two-dimensional simulations for the super-ordnance velocity projectile, where the residual length and velocity were 18.9 cm and 1.64 km/s, respectively, indicated that underconfinement in the 3-D (numerical) witness pack resulted in an additional 3.3 cm of penetration. Therefore, the corrected total depth of penetration into the RHA witness pack was estimated

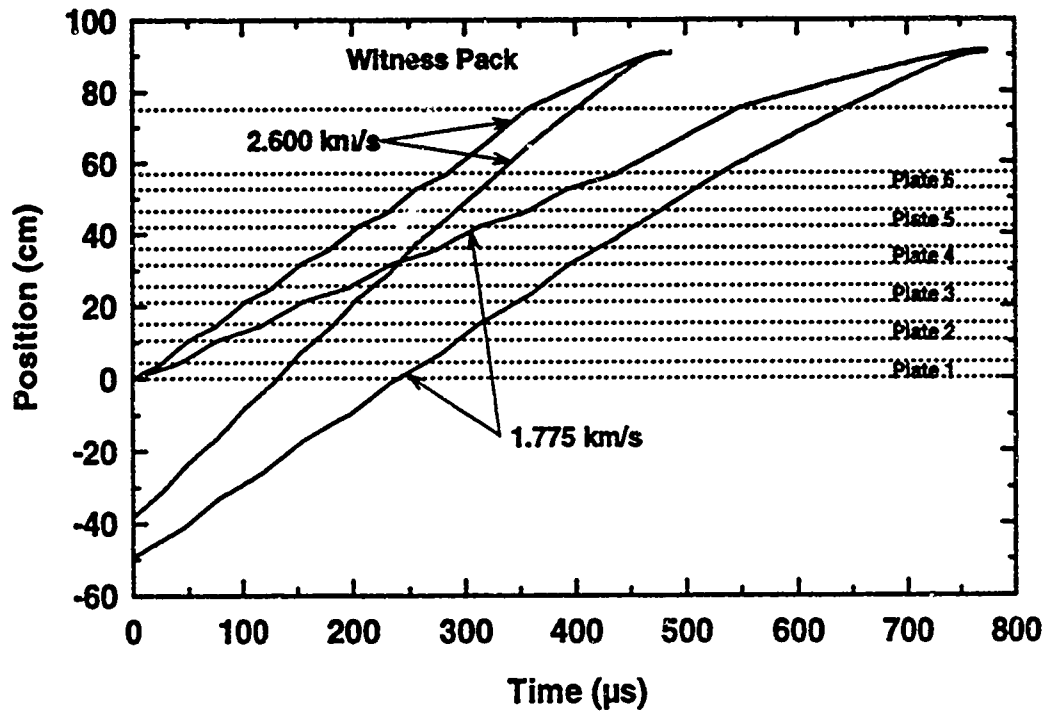


Figure 41. Nose and tail positions versus time, spaced-plate target—Walker-Anderson results.

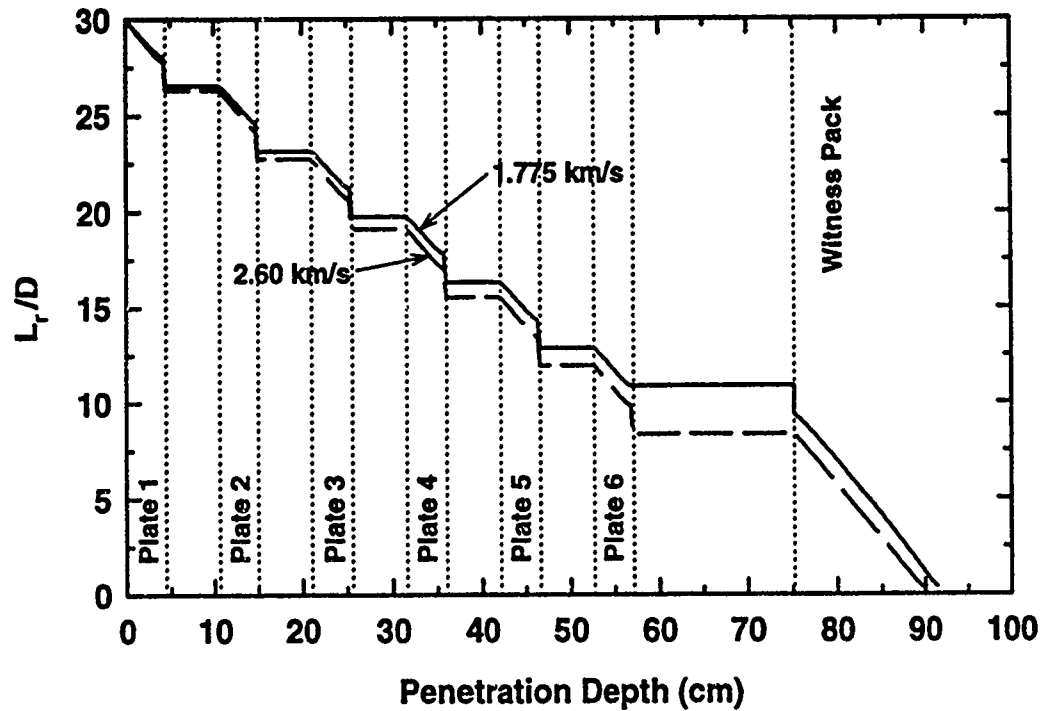


Figure 42. Normalized projectile length versus depth of penetration, spaced-plate target—Walker-Anderson results.

to be 18.0 cm. The hypervelocity projectile, on the other hand, had a residual length and velocity of 9.6 cm and 2.47 km/s, respectively, and the resulting penetration decrement was determined to be 1.5 cm. Therefore, the corrected depth of penetration for this projectile was 14.1 cm.

5.5 Experimental Results and Summary

The depths of penetration into the witness plate for the experiments, CTH, and the analytical models for the spaced-plate target are given in Table 8. It would seem that impact inclination is an important factor in the experiments; this will be discussed further in a couple of paragraphs.

The total line-of-sight steel thickness for the spaced-plate target (exclusive of the witness pack) was 27.0 cm. Focusing on the 1.72 and 2.60 km/s experiments (and not the 1.78 and 2.62 km/s experiments) for the moment, the total steel penetrations (line-of-sight thickness of the high-hard steel plates and the residual penetration into the witness packs) were 41.4 cm and 37.8 cm for the super-ordnance velocity and hypervelocity projectiles, respectively. Although the total penetrations for the spaced-plate target differ only by 9%, the super-ordnance velocity projectile went approximately 40% deeper into the witness pack than the hypervelocity projectile. This is contrasted with the RHA target, with a line-of-sight thickness of 45.7 cm, where there existed only a 1.4% difference in total penetration, and where the hypervelocity projectile went slightly deeper into the witness pack (10%) than the super-ordnance velocity projectile. This again reinforces our observation that repeated impacts and breakouts, combined with target obliquity, have a detrimental effect on projectile performance.

The pretest predictions overpredicted the depths of penetration into the witness pack, although, in general, the computations and the analytical models predicted the correct ordering of the penetration, i.e., the super-ordnance velocity projectile penetrates deeper into the witness pack than the hypervelocity projectile. Comparing the results of the Walker-Anderson model with those of the MITI model, it is evident that it is necessary to account explicitly for failure of the leading portion of the projectile after perforation of an oblique plate. We note that allowing for $1.8D$ of projectile to fail after perforation of a plate seems to provide somewhat better agreement with the experimental results than the use of the $1.5D$ value; however, using $1.8D$ resulted in the hypervelocity projectile penetrating deeper into the witness pack. The analytical results do not show as large a difference in the depths of penetration into the witness pack as seen in the experiments. CTH correctly predicts a difference of approximately 3.9 cm, in good agreement with the difference observed in the experiments. The 3.6 cm difference predicted by the MITI model is misleading since the model overpredicted witness pack penetration by approximately 100%.

The oblique spaced-plate target problem illustrates the need for improvement in breakout mechanics of the numerical and analytical models. In particular, material failure is currently treated in a rather simplistic fashion within CTH. Although the tensile failure model captures the essence of void nucleation, growth, and coalescence, the computational procedure permits unrealistic large strains in tension before material separation. Engineering judgement was used to simulate better target breakout, by the choice of mixed cell constitutive treatment, but the repetitive application of the procedure to multiple plates probably represents a source of error in the results. Similarly, the breakout modeling of the Walker-Anderson and MITI models are overly simplistic. The computations predict severe nose distortion as a result of breakout from an oblique plate; this physics is totally absent from the analytical models, although an attempt was made heuristically with the

Table 8. Depths of Penetration into Witness Pack: Spaced-Plate Target

V_s (km/s)	Penetration into Witness Pack (cm)						MITI
	Experiment	Pitch (deg)	Yaw (deg)	CTH (corrected)	Walker-Anderson (1.5D)	Walker-Anderson (1.8D)	
1.72	14.4	*	*				
1.775				18.0	16.3	12.4	28.5
1.78	10.0	0.45	2.34				
2.60	10.8	0.04	0.44				
2.600				14.1	15.8	13.2	24.9
2.62	**	-1.70	2.62				

* Equipment malfunction.

** Not reported

Walker-Anderson model to account for this feature. Not accounting for nose failure in the MITI model resulted in greatly overpredicting the penetration into the witness pack. In application of the Walker-Anderson model, it was assumed that the amount of nose material lost (in projectile diameters) was the same at both velocities. It would appear that this is not an appropriate assumption, and in fact, if the higher velocity projectile lost slightly more nose material (in projectile diameters, e.g., $2.0D$ instead of $1.8D$), there would be reasonable agreement between the analytical results and the experiments. In particular, the analytical model would then give a larger difference in the final penetration between the two projectiles. In summary, the accumulative errors resulting from modeling breakout six times is probably the largest source of error in the computations and the analytical models.

Analysis of the computational results indicates that projectile performance should be sensitive to projectile pitch because the projectile could "wipe" the sides of the holes in the plates, e.g., see Figs. 33f, 36b, 36c. An estimate can be made of the minimum pitch and yaw angles for the oblique, spaced-plate target. For normal impact, a geometric relationship can be formulated to estimate the critical angle of inclination, i.e., the angle at which the tail of the projectile just strikes the crater wall:

$$\theta_c = \sin^{-1} \left\{ \frac{(H/D - 1)/2}{L/D} \right\}, \quad (20)$$

where H/D is the crater hole diameter normalized by the projectile diameter. Estimates of the hole diameter as a function of velocity can be made from experimental data; curve fits for tungsten alloy projectiles into RHA-like targets have been made in Ref. [11]. H/D is approximately 2.1 at 1.775 km/s, and 2.75 at 2.60 km/s. Therefore, for the $L/D = 30$ projectiles, θ_c is approximately 1.0° at an impact velocity of 1.775 km/s, and 1.7° at 2.60 km/s.

The target is oblique, however, and to our knowledge, no analytical expression currently exists for critical pitch and yaw for oblique targets. The computational and analytical predictions assumed "perfect" impact, i.e., no pitch or yaw; however, estimates can be made by examining the computational results. Hole size in the z -direction appears, to first order, to be unaffected by plate obliquity. Therefore, the critical yaw angle is 1.0° at 1.775 km/s, and 1.7° at 2.60 km/s.

On the other hand, the holes are elliptical in shape as the crater is traversed in the x -direction; this is due to target obliquity, and for plates 2 through 6, the dynamics of plate perforation. Figure 38 shows the asymmetry in hole appearance, and Fig. 39 demonstrates how the holes look as the target is traversed in the x -direction, i.e., up and down in Fig. 27. The results of the computations indicate that the projectile is within one-half to one computational zone of wiping the side of a hole (the projectile has zero pitch and yaw in the computations). Therefore, it is seen that the projectile tail could interact with a hole if the projectile was pitched up or pitched down. The estimate of a critical pitch angle is made by considering the resolution of the numerical simulation. Six zones exist across the diameter of the projectile, and since the projectile has an L/D of 30, and the zoning is square, one zone of pitch over the length of the projectile is approximately $1/180$ radians, or 0.32° . Although the results shown in Figs. 38 and 39 are for the 2.600 -km/s impact, similar results are obtained for the 1.775 -km/s impact case. Therefore, the critical pitch angle is $0.16 - 0.32^\circ$. This is considerably more stringent than the critical yaw angle.

These estimates of critical pitch and yaw angles provide meaningful insights to the experimental results. For example, the witness plate penetration of the 1.78 km/s impact decreased by 4.4 cm over the 1.72 km/s impact case. It certainly can be speculated that the decreased penetration is attributed to the inclination of the rod at impact (unfortunately, the flash X-rays malfunctioned for the 1.72 km/s impact). A second test at nominally 2.6 km/s (2.62 km/s) had a relatively high impact inclination compared to the other experiment at near the same velocity. For the 2.62 km/s impact case, a flash radiograph taken of the residual projectile as it passed between the last high-hard steel plate and the witness pack showed the tail of the projectile was completely broken off. These experimental observations, along with the insights provided by the computations, lend support to the conclusion that penetration performance through the spaced-plate target is quite sensitive to impact inclination.

The interaction of long-rod projectiles with oblique plates represents a canonical problem of interest to the Army. The results of these two problems can serve as benchmark examples for high performance computing since this type of problem taxes the capabilities of today's conventional supercomputers. Almost one million zones and 38.1 MW of memory were required to represent a reduced geometric model of the problem. Although hundreds of CRAY 2 CPU hours were needed to perform the 4000-6000 integration time steps, wall-clock time was considerably longer because of the size of the problem. It took approximately 2.5 months to obtain the complete numerical solutions since the "job" had to "compete" with other problems for the computer resources. Additionally, as already discussed, the physics of the interactions is not well accounted for in analytical models of penetration.

6.0 CERAMIC LAMINATE TARGET

6.1 Target Description

The ceramic laminate target is shown in Fig. 43. The target consisted of a 5.7-cm-thick RHA steel cover plate, four 99.5%-pure Al_2O_3 ceramic elements with a total thickness of 30.5 cm, and a RHA back plate 11.4-cm thick. An RHA witness pack was placed 7.62 cm behind the target to "capture" the residual projectile. The test was performed at 0° obliquity.

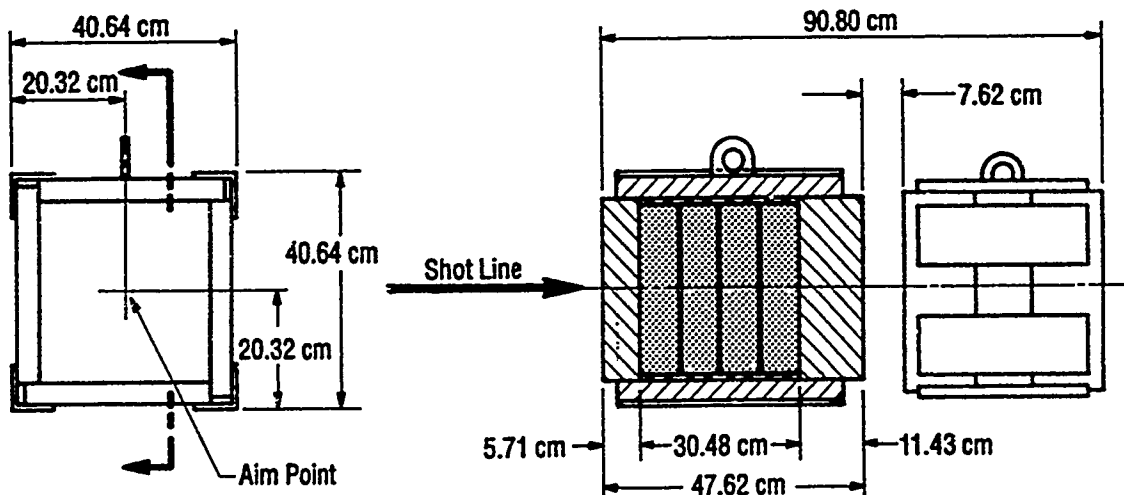


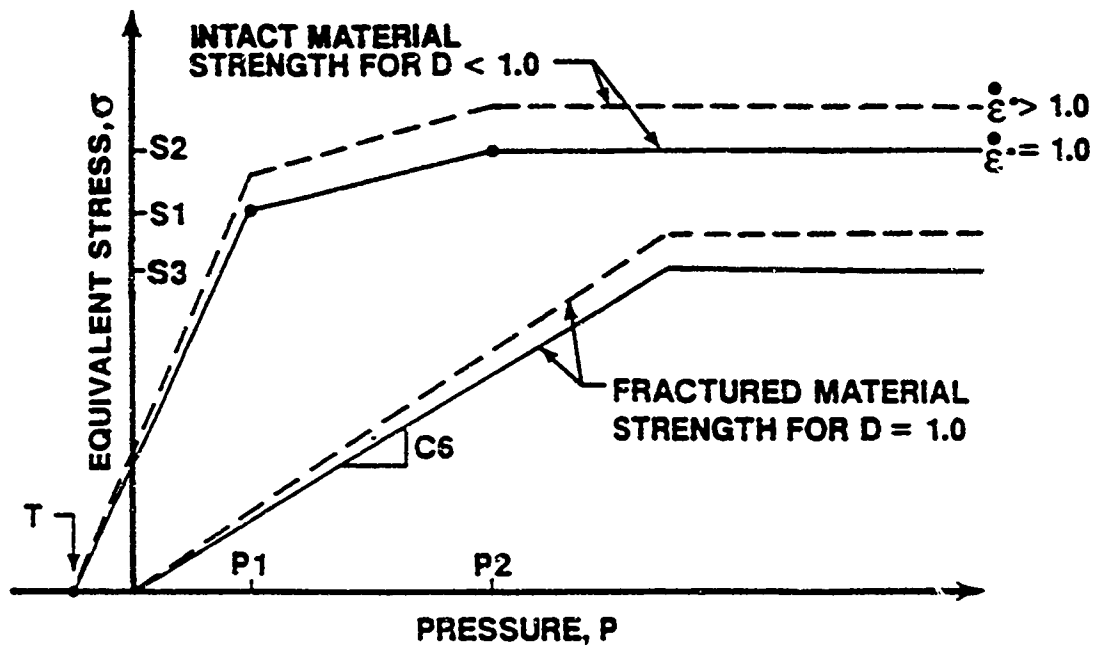
Figure 43. Schematic of ceramic laminate target

6.2 Ceramic Model

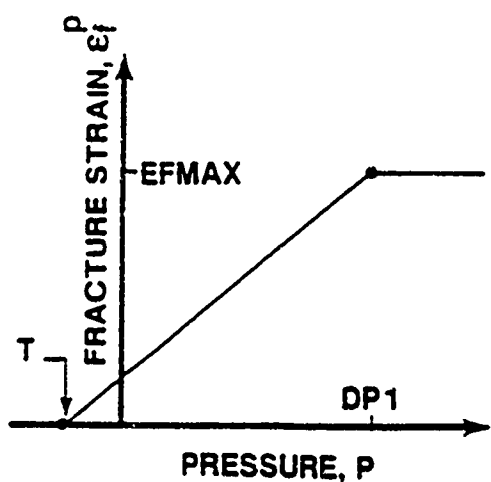
Johnson and Holmquist have developed a phenomenological model for ceramics that attempts to incorporate many of the features observed experimentally in laboratory tests. However, this model—and the model constants—is still in a development, refinement, and evaluation stage. Model constants have been obtained experimentally for one type of aluminum oxide, Coors AD-85 [30-31]. But the ceramic in the target is a higher grade of aluminum oxide, being 99.5% pure Al_2O_3 . Therefore, constants for 99.5 Al_2O_3 had to be estimated. This section provides a very brief description of the ceramics constitutive model, and the next section describes the effort in estimating constitutive constants for 99.5 Al_2O_3 .

The Johnson-Holmquist (J-H) model for brittle materials [8] was used for the ceramic. More recently, Johnson and Holmquist have made slight modifications to the model [32]; however, at the time the pretest calculations were initiated, the revised model was still under development, so only the original model was used.

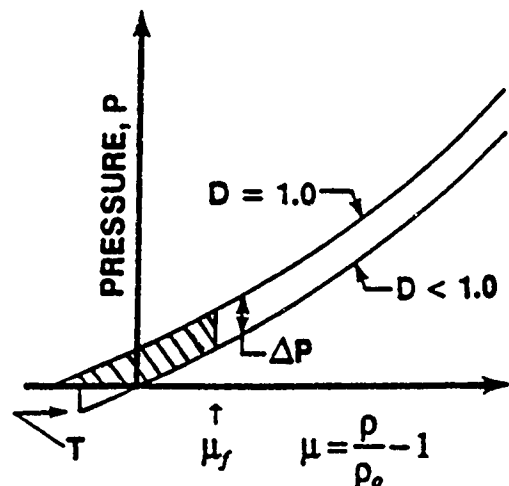
Figure 44 provides a pictorial representation of the model. The prevalent ideas, rooted in experiments, are:



a. Pressure-dependent strength of ceramics—Johnson-Holmquist ceramics model



b. Maximum allowed plastic strain—Johnson-Holmquist ceramics model



c. ΔP increase in equation of state at failure—Johnson-Holmquist ceramics model

Figure 44. Pressure-dependent strength of ceramics—Johnson-Holmquist ceramics model

- 1) Ceramic materials are stronger under confining pressures ($S1$ and $S2$, $P1$ and $P2$), Fig. 44a;
- 2) Ceramic materials have little strength in tension (T), Fig. 44a;
- 3) Ceramic materials can strain-rate harden ($C3$), Fig. 44a;
- 4) Ceramic materials display a "plastic flow" regime after initial yield and before complete failure (ϵ_f^p and DPI), Fig. 44a, 44b;
- 5) The fracture of a brittle material can result in "bulking," or volume expansion, of the material. This is simulated in the model by adding a bulking pressure (ΔP), estimated from energy arguments, to the mean stress (pressure), Fig. 44c;
- 6) Ceramic materials can still support shear stresses after fracture. That is, the strength of a failed ceramic is not necessarily zero. There is a provision for a pressure-dependent strength after failure ($S3$ and $C6$), Fig. 44a.

The terms in parenthesis are the model parameters that control each of the effects. The reader is referred to Refs. [8, 30-33] for further information on the model.

The parameters used for the J-H model are given in Table 9. Since constants had been determined for AD85, these were used as a first estimate for the model constants of 99.5 Al₂O₃. The density, tensile strength, and shear modulus were set equal to measured values for 99.5 Al₂O₃. The intact strength was increased to a value commensurate with the strength inferred from the Hugoniot Elastic Limit (HEL).

Table 9. Constitutive Parameters for the Johnson-Holmquist Ceramics Model

Material	ρ (g/cm ³)	$P1$ (GPa)	$P2$ (GPa)	$S1$ (GPa)	$S2$ (GPa)	$S3^*$ (GPa)	$C6$ (-)	DPI (GPa)	T (GPa)	G (GPa)	ϵ_f^p (-)
99.5 Al ₂ O ₃	3.89	1.4	7.3	3.91	5.58	1.2-4.8	1.13	3.1	-0.26	152	0.005

* This constant was varied in parametric studies.

6.3 Parametric Studies with Ceramic Model

A number of computer runs were made to evaluate the ability of the constitutive model to predict the results of laboratory experiments. Two experimental arrangements were used: depth-of-penetration (DOP) tests on 99.5 Al₂O₃ tiles of varying thicknesses performed by Woolsey and colleagues [34-36], and PHERMEX tests conducted at Los Alamos National Laboratory [37]. Each will be discussed in turn.

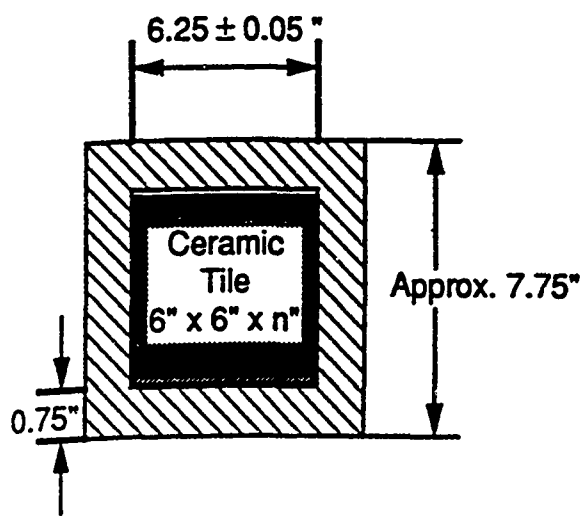
6.3.1 Depth-of-Penetration Tests: CTH

The experimental arrangement used by Woolsey, *et al.*, is shown in Fig. 45 [34-36]. The residual depth of penetration into the RHA steel substrate as a function of the ceramic tile thickness was evaluated for 65-g, $L/D = 10$, tungsten alloy projectiles. The nominal impact velocity for the experiments was 1.5 km/s. A summary of the experimental results is shown in Fig. 46 as the open circles.

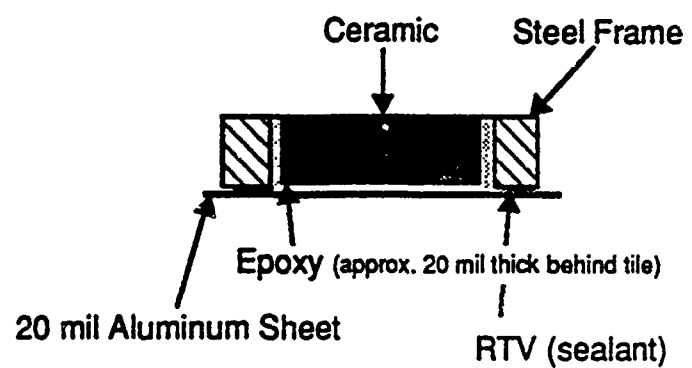
The first few computer runs using the Johnson-Holmquist ceramics model revealed several features that guided the rest of the parametric study. First, the computations showed that virtually all the ceramic material was damaged around the projectile, extending almost to the lateral boundaries of the ceramic block. This observation suggested that the curve controlling penetration was the "failed material" curve, i.e., the lower curve, in Fig. 44a. Second, the pressures at the projectile-target interface were on the order of 7.5 GPa. This was substantially larger than the estimates for the stress cap (parameter $S3$ in Fig. 44a and Table 9) for the failed material. Also, since the pressure in the immediate vicinity of the projectile-target interface would also be quite high, the value of the slope $C6$ would have virtually no influence. That is, the pressures within the target, near the projectile-target interface were sufficiently high that the constitutive response of the failed target material was controlled primarily by the stress cap ($S3$) of the failed material. Johnson and Holmquist, in parametric studies of their own, reached a similar conclusion [32]. Therefore, only the parameter $S3$ was varied in the parametric study.¹¹

Figure 47 shows the penetration velocities versus depth of penetration for a ceramic tile thickness of 2.0 cm. The upper curve in the figure used a value of 1.4 GPa for the cap, and the lower curve used a value of 2.6 GPa. After perforating the ceramic tile, the quasi-steady-state penetration velocities are very similar since the projectile is penetrating RHA. The total depths of penetration are 6.72 cm and 7.10 cm, respectively. The residual depth of penetrations (the depths of penetration into the RHA) are 4.72 and 5.10 cm, respectively. These values are plotted in Fig. 46, for a tile thickness of 2.0 cm, as the filled circles. Similar computations were performed for a tile thickness of 3.0 cm, and these results are plotted in Fig. 46. Three simulations were performed for a tile thickness of 4.0 cm; values of 1.2, 2.6, and 4.8 GPa were used for the cap of the failed material. The penetration velocities as a function of depth of penetration are shown in Fig. 48. The results for the 4.8-GPa value do not differ appreciably from the 2.6 GPa computer run. This is attributed to the fact that the pressure cap is now sufficiently "high" in stress that the pressures within the target, a little ways away from the projectile-target interface, fall beneath the cap; thus, some of the "strength" of the failed material is controlled by the slope $C6$. The residual depths of penetration are plotted in Fig. 46.

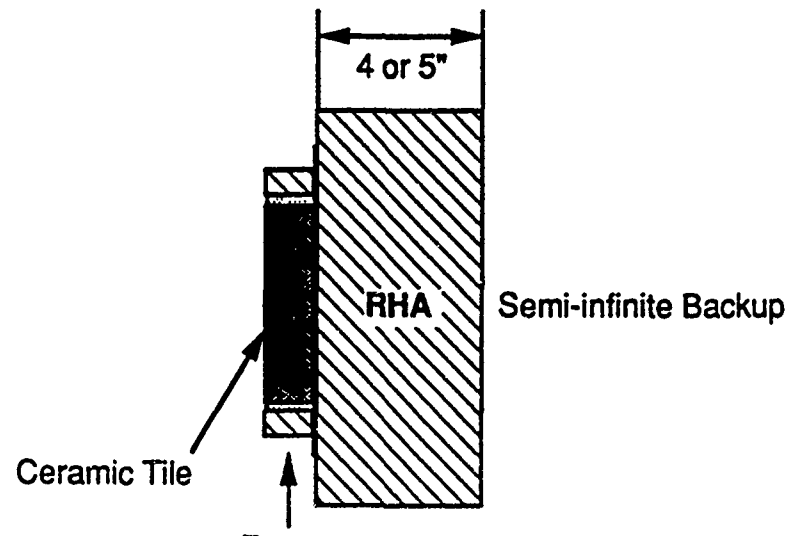
¹¹ It was felt that the intact strength and the tensile strength of 99.5% Al_2O_3 were reasonably known, so these were not changed. Also, since the ceramic was being "overwhelmed" by the projectile, slight changes to $S1$, $S2$, and ϵ_f would have very little effect on the final results. Therefore, it was concluded that these parameters would not be changed during the parametric study.



Frame Configuration
Front View



Frame Configuration
Side View (Cutaway)



Target Assembly Test Setup

Figure 45. Experimental arrangement for depth-of-penetration studies
(from Woolsey, *et al.* [34-36]).

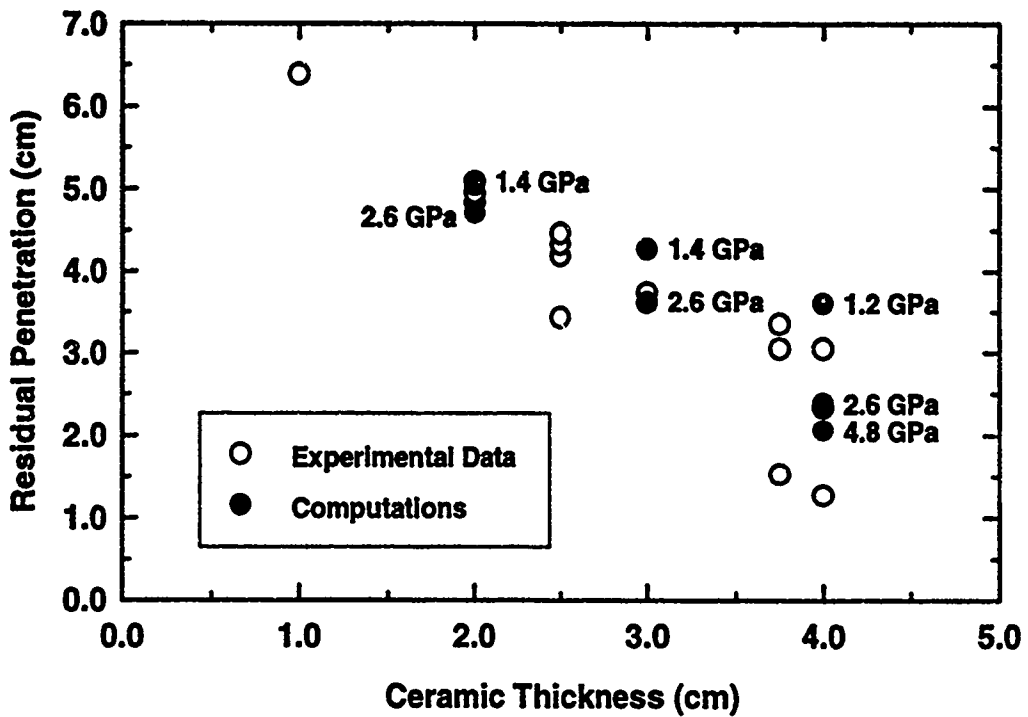


Figure 46. Summary of experimental and computational results for DOP tests.

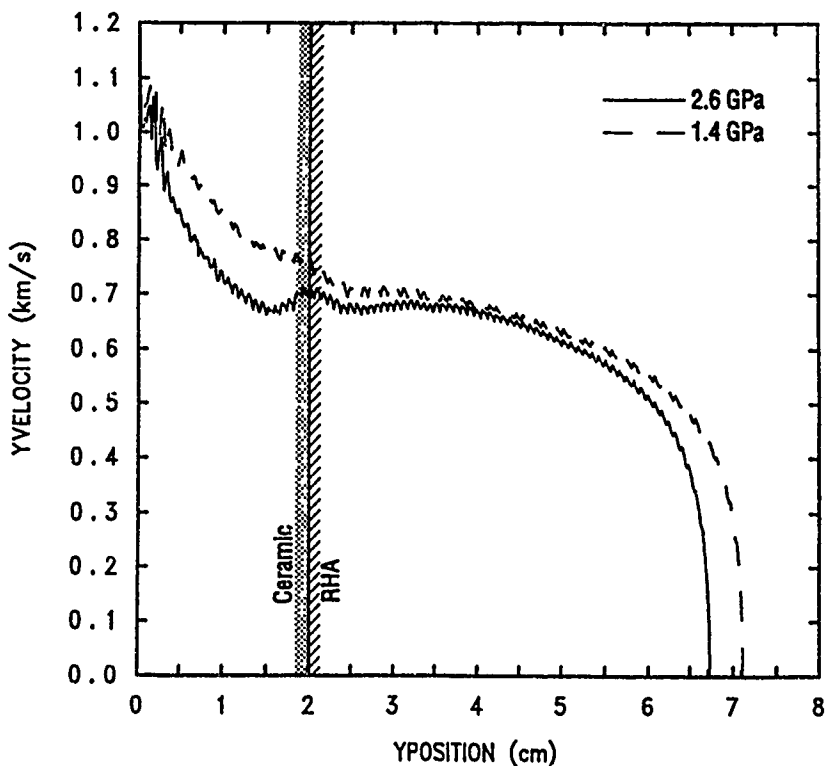


Figure 47. Penetration velocity versus depth of penetration for CTH simulation of DOP tests, tile thickness = 2.0 cm.

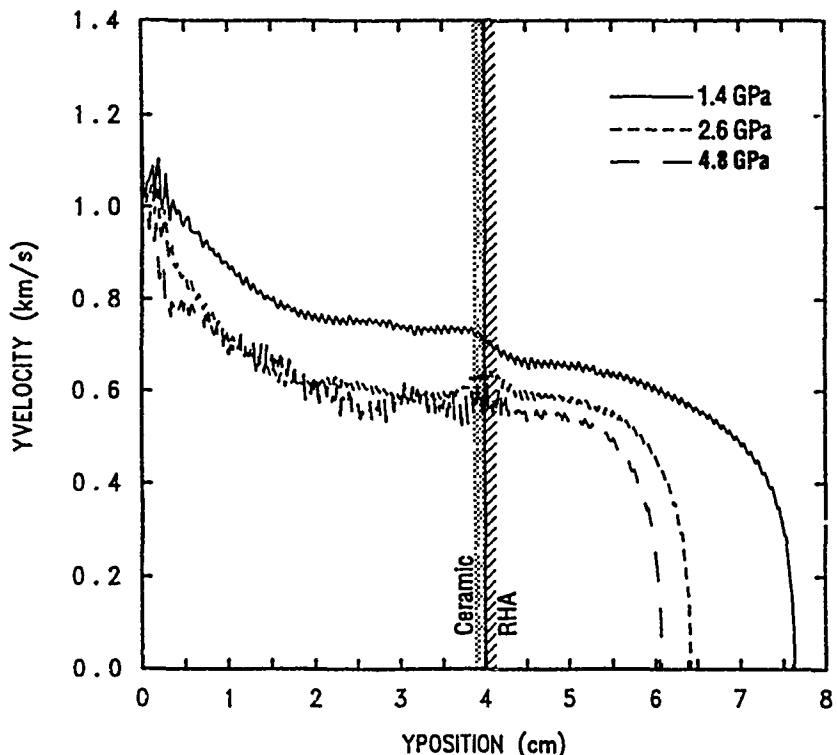


Figure 48. Penetration velocity versus depth of penetration for CTH simulation of DOP tests, tile thickness = 4.0 cm.

As already discussed, the filled circles in Fig. 46 represent the results of the computations; the value used for the flow stress is denoted by each computational point. It is clear from the scatter in the experimental data, particularly for the thicker tiles, that several different values for the failed flow stress might be used. However, it is seen that the value of 1.4 GPa tends to overpredict residual penetration, and the value of 4.8 GPa underpredicts residual penetration. The predictions for residual penetration using 2.6 GPa as the cap for the failed material falls within the experimental scatter of the data, and using this value appears to replicate the experimental data reasonably well over the various tile thicknesses tested. Thus, 2.6 GPa was the value used in the CTH computations for the ceramic laminate target.

6.3.2 PHERMEX Experiments: CTH

Experiments were conducted at Los Alamos National Laboratory using the PHERMEX facility to measure the *in situ* positions of the nose and tail while penetrating the ceramic target [37]. The targets were fairly heavily confined, and the ceramic insert was sufficiently thick to contain the entire penetration. Again, $L/D = 10$, tungsten alloy projectiles were used. The impact velocities were nominally 1.6 km/s.

Four tests were performed; the time delay for pulsing the flash X-ray was changed so as to interrogate penetration at different times during the penetration history. The positions of the nose and tail versus time after impact are shown as squares in Fig. 49 for the experimental data points.

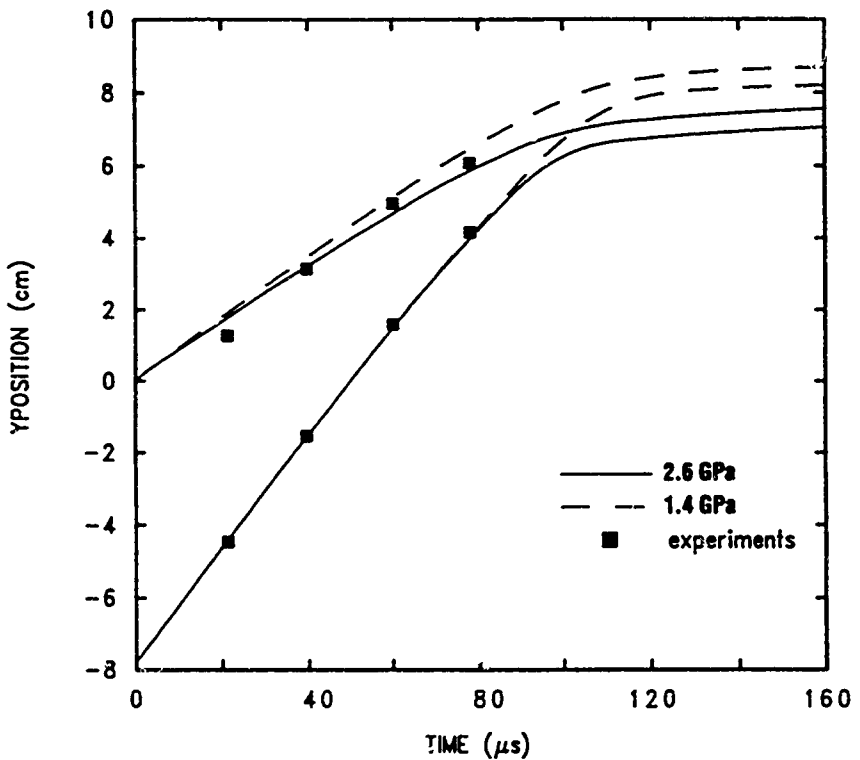


Figure 45. PHERMEX results, and CTH computations, for 99.5% Al_2O_3 .

CTH calculations were performed using the 1.4 and 2.6 GPa values for the cap of the flow stress for the failed material. The dotted lines give the positions of the nose and tail for the 1.4 GPa value, and the solid lines for the 2.6 GPa value.

A few items are worth noting. The computations reasonably predict the position of the tail of the projectile. This observation implies that the strength model for the tungsten-alloy projectile is reasonably accurate. The experimental results for the position of the projectile nose with time suggest that the ceramic is much stronger initially (the penetration positions from the computations lay above the first experimental data point), but that the effective strength of the ceramic decreases with time (or with penetration depth). In an integrated sense, the 1.4 GPa value overpredicts the depth of penetration versus time, and the 2.6 GPa value underpredicts the depth penetration versus time. From the PHERMEX tests, it might be inferred that the cap for the failed material in the J-H model should be an average of the 1.4 and 2.6 GPa values, but further calibration studies using CTH were not performed.

6.3.3 Calibration of the Walker-Anderson Model

The Walker-Anderson model is based on a description of the flow field around a long-rod penetrator. The conceptual framework for the extent of plastic flow is built on ductile cavity expansion, and the application of the model to ceramics should be regarded as an empirical approach with parameters that are adjusted to fit experimental data. Since penetration through ceramic appears to be controlled by the flow stress of the failed material, as discussed above, it was decided to interpret the value of the flow stress used by the model as an effective flow stress for the damaged ceramic. That is, it is the characteristics of the failed ceramic that dominate penetration behavior. Woolsey's experiments and the PHERMEX experiments were again used for comparison purposes.

For Woolsey's experiments, it was found that the 2.6 GPa value for the flow stress led to penetration being underpredicted by the Walker-Anderson model. For example, one set of results is shown in Fig. 50 for a 3.0-cm Al_2O_3 tile. The positions of the nose and tail of the projectile are shown as a function of time for two values of the flow stress: 2.4 GPa and 1.4 GPa. The total depths of penetration (ceramic plus RHA) for two experiments are denoted by the diamonds. It is seen that a value of approximately 1.4 GPa would seem to be more appropriate for the Walker-Anderson model.

Why the difference between CTH and the Walker-Anderson model? There exists a region within the ceramic, for the computational model, where the flow stress is proportional to the pressure. Therefore, the cap value used in CTH does not necessarily represent an "average" value for the flow stress—particularly for higher cap values—as it does in the analytical model.

Figure 51 compares the Walker-Anderson model, using four different values for the effective flow stress of the failed ceramic, to the PHERMEX data points. The parametric study first assumed the strength of the intact ceramic, 6.03 GPa, and then the strength was reduced by approximately 1.5 GPa for each of the subsequent model calculations. The model results pass through the first data point using the strength of the intact material, but afterwards, this value is much too high since it considerably underpredicts the subsequent penetration history. Comparison of the model to the experimental data in Fig. 51 reinforces the earlier observation that the penetration resistance of the ceramic is much higher early in the penetration history, and that later, the strength is degraded. The ability of a value of 1.51 GPa for the effective flow stress to duplicate approximately the last three data points also suggests that the degraded strength of the ceramic might be approximated by a constant value.

Better agreement can be obtained by letting the ceramic be strong during the very early phase of penetration, and then have the strength degrade. This was done in Fig. 52. The intact strength of the 99.5% Al_2O_3 (6.03 GPa) was used at early times, and after a specified time, the strength was degraded to 1.2 GPa. A value of 1.2 GPa provided a better fit to the late time data than did a value of 1.4 GPa. In Fig. 52, the time before strength degradation was varied. Using the intact strength for the first 5 μs provides the best agreement with experiment. For the ceramic laminate target, 5 μs is a very small portion of the total penetration time, so the time dependence was ignored and the ceramic was modeled using only the strength of the failed material. Figure 53 shows the comparison of the Walker-Anderson model with the PHERMEX data using a value of 1.2 GPa for the effective flow stress for the entire penetration history. Agreement is reasonably good.

6.4 Numerical Simulations

The zoning used for the ceramic target, Fig. 43, was similar to the zoning employed for the RHA target. Square 1.27-mm zones were used in the projectile/target interaction regions near the front and rear faces of the target. The length of zones in the axial direction was gradually increased near the mid-depth region of the target to a maximum length of about 3 mm. Outside the projectile/target interaction, the width of zones in the radial direction was increased, with the exception of the region near the ceramic/steel side plate interface, which contained a 7 mm layer of epoxy. The radial zone width across this layer was held fixed at 1.27 mm.

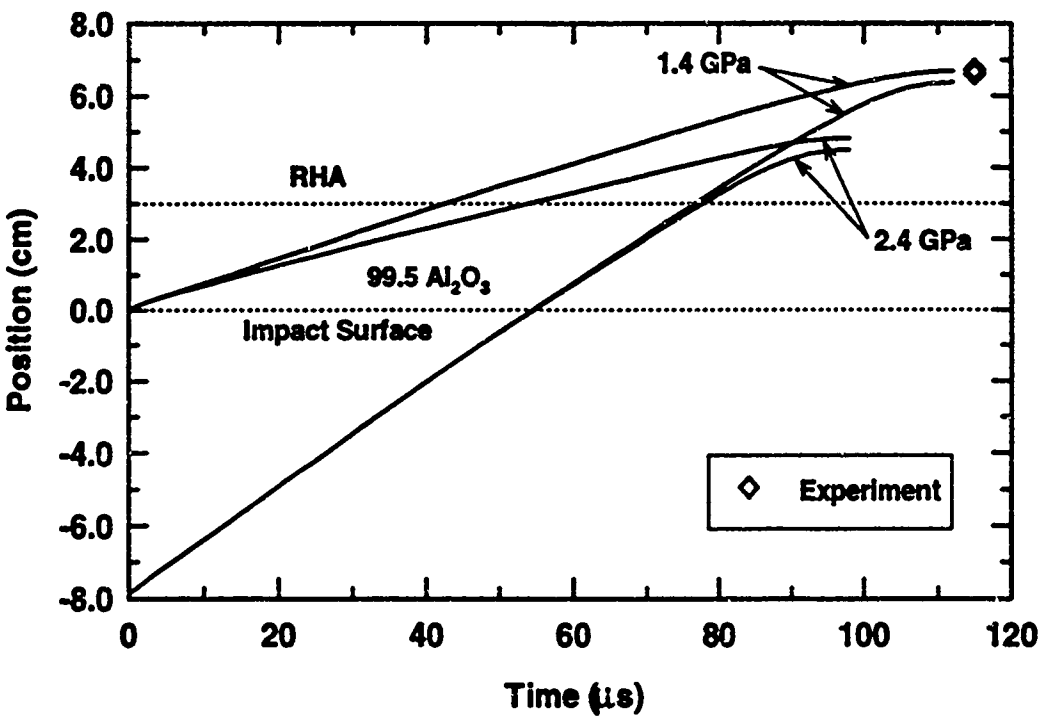


Figure 50. Comparison of the depth of penetration from the Walker-Anderson model for DOP experiments, tile thickness = 3.0 cm.

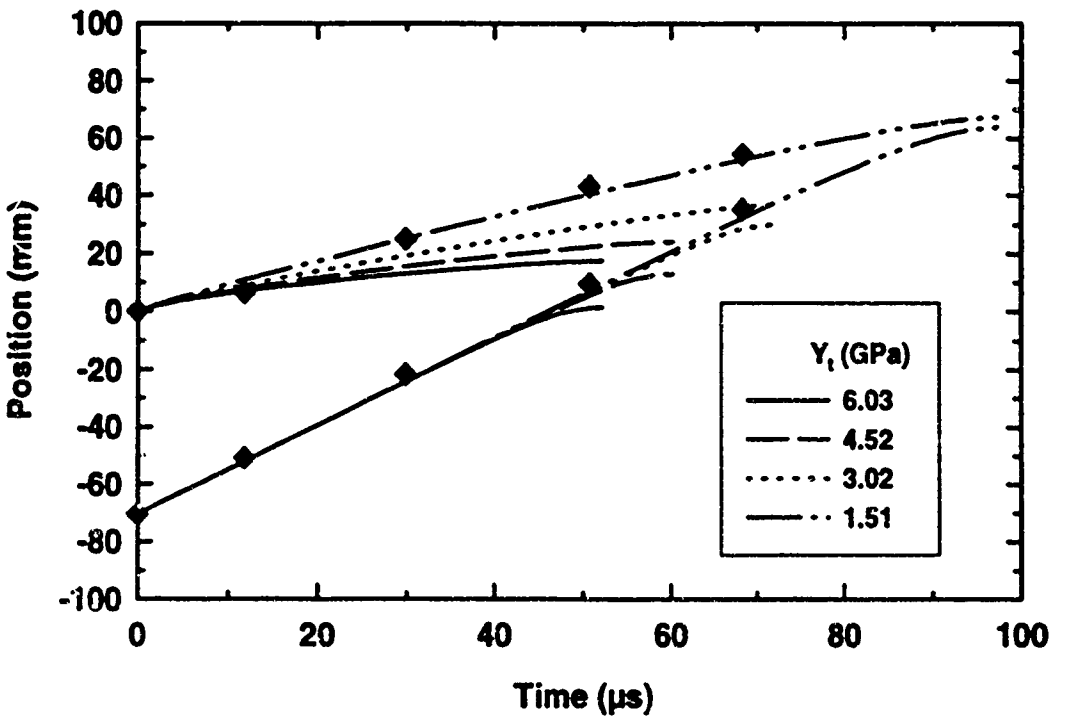


Figure 51. Parametric study for the effective flow stress in the Walker-Anderson model, PHERMEX experiments.

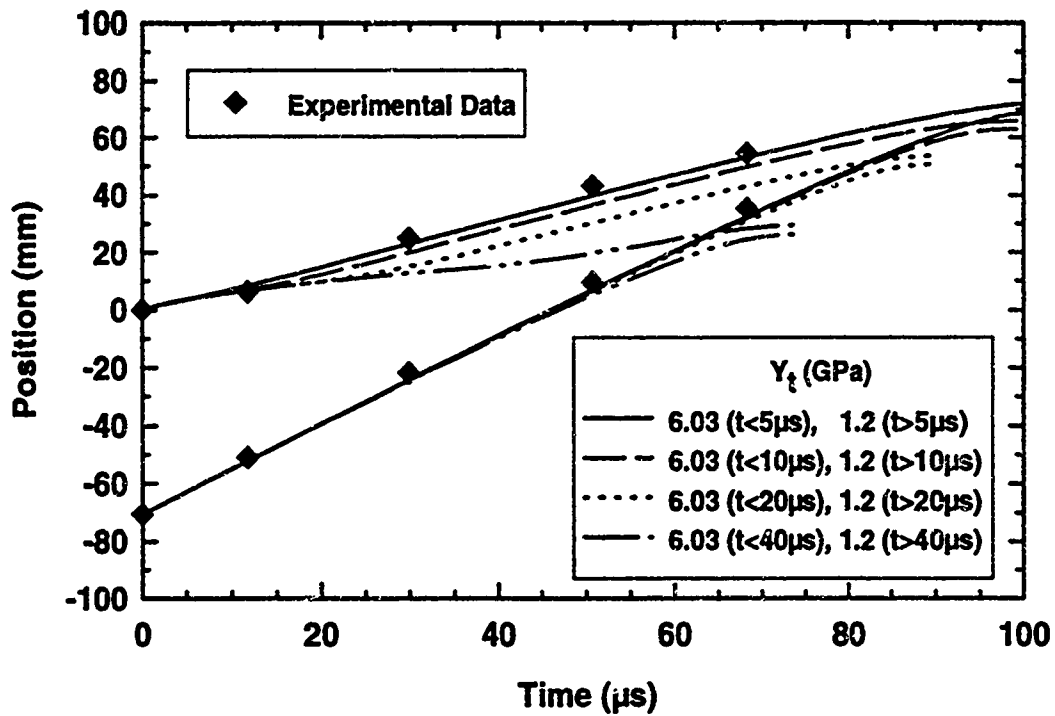


Figure 52. Time-dependent effective flow stress in the Walker-Anderson model, PHERMEX experiments.

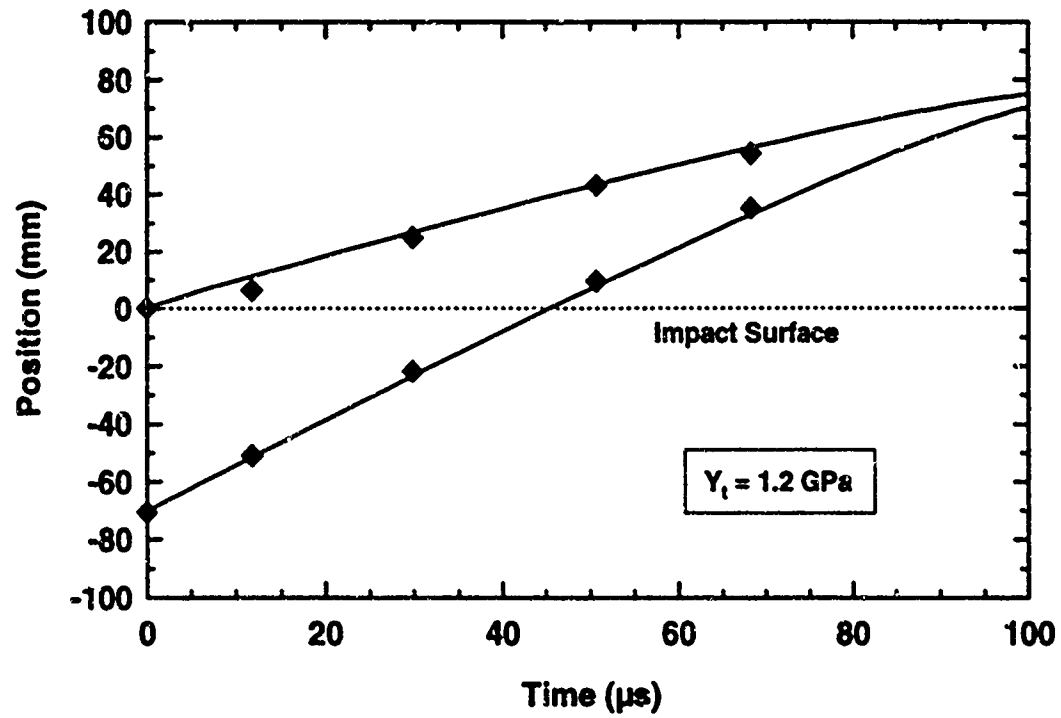


Figure 53. Comparison of the Walker-Anderson model, effective flow stress of 1.2 GPa, with the PHERMEX experiments.

The positions of the nose and tail as a function of time are plotted in Figs. 54 for the two velocities. The original (initial) position of the interfaces are drawn onto the figure. With the values used for the Johnson-Holmquist ceramics model, the projectile was "stopped" within the ceramic element for the 1.775-km/s impact case (the term "stopped" really denotes that the projectile has been completely eroded), and the target was perforated for the 2.600-km/s impact case.

The penetration and tail velocities of the projectiles versus depth of penetration are shown in Fig. 55 for the two cases. For the 2.600-km/s impact, the penetration velocity is barely "perturbed" by the ceramic-steel interfaces. That is, the penetration velocity is approximately constant, independent of whether the projectile is penetrating steel or ceramic. This is not true for the 1.775-km/s impact case; the penetration velocity is higher in the steel cover plate than it is in the ceramic. Comparing Fig. 55 to Fig. 7, it is observed that the quasi-steady penetration velocity in the ceramic element is approximately 0.25 km/s slower than it is through RHA for an impact velocity of 1.775 km/s (as already noted, the penetration velocities for the 2.600-km/s impact case are approximately the same, 1.50 km/s, for the ceramic and steel).

The penetration pressures for the two cases are shown in Fig. 56. These pressures can be contrasted with the penetration pressures for the RHA target, Fig. 8. For example, the penetration pressure is a function of the penetration velocity, target density, and target strength and confinement. For the 1.775-km/s impact case, the penetration pressure does not change substantially between the cover plate and the ceramic element (except near the cover plate-ceramic interface; the ceramic is very strong before it fails). Since the penetration velocity decreases in the ceramic as compared to the RHA, and the ceramic has approximately one-half the density of steel, then the effective strength of the failed ceramic is higher than it is for the steel. Similar conclusions can be drawn from the 2.600-km/s impact calculations.

In Fig. 12, we see only a slight difference in the normalized lengths of the projectiles as a function of depth of penetration for the RHA target. The slower penetration velocity within the ceramic element for the 1.775-km/s impact case results in an erosion rate that is higher than if the material were steel. Therefore, the normalized lengths of the projectiles for the two impact cases as a function of penetration depth, Fig. 57, deviate from each other within the ceramic element.

The computations predicted that the projectile would only penetrate to approximately the ceramic-RHA interface for the 1.775-km/s impact case. At the higher impact velocity, the projectile perforated the ceramic laminate target. Figure 58 shows what is left of the projectile just about the time of perforation of the rear RHA plate. This remnant projectile then penetrates 2.1 cm into the RHA witness pack.

6.5 Analytical Predictions

The Walker-Anderson model was run with two different values for the effective flow stress of the failed ceramic. First, the model was run using 2.4 GPa. Nose and tail positions are plotted versus time for the two impact cases in Fig. 59. The model results are essentially identical to the predictions of CTH using the J-H model: the projectile penetrated to the ceramic-RHA interface for the 1.775-km/s impact case, and the target was perforated for the 2.600-km/s impact case. The normalized lengths of the projectiles as a function of penetration distance are shown in Fig. 60.

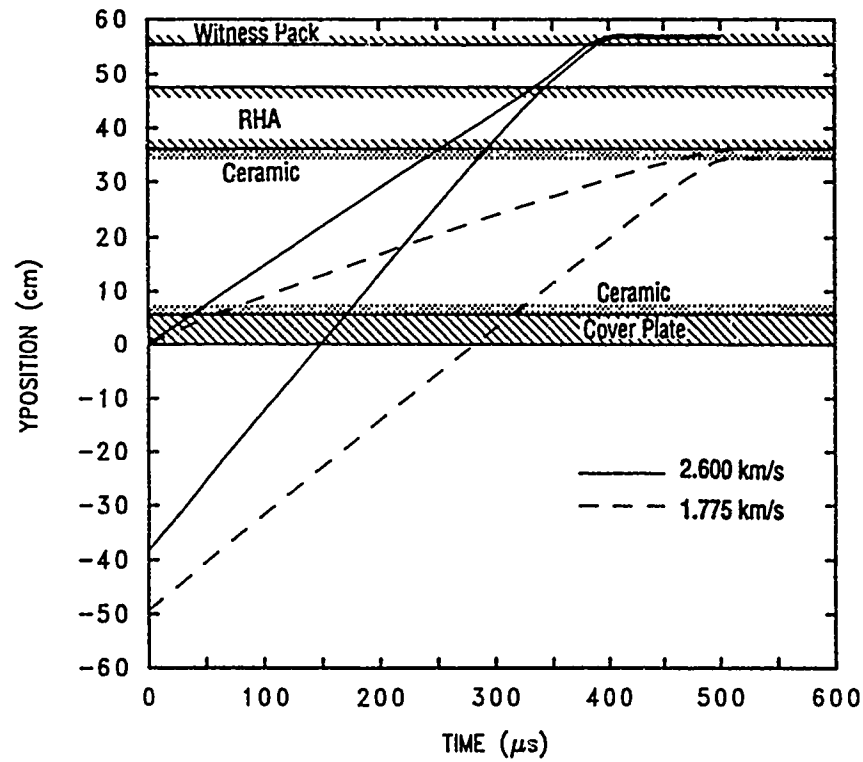


Figure 54. Nose and tail positions versus time, ceramic laminate target—CTH results.

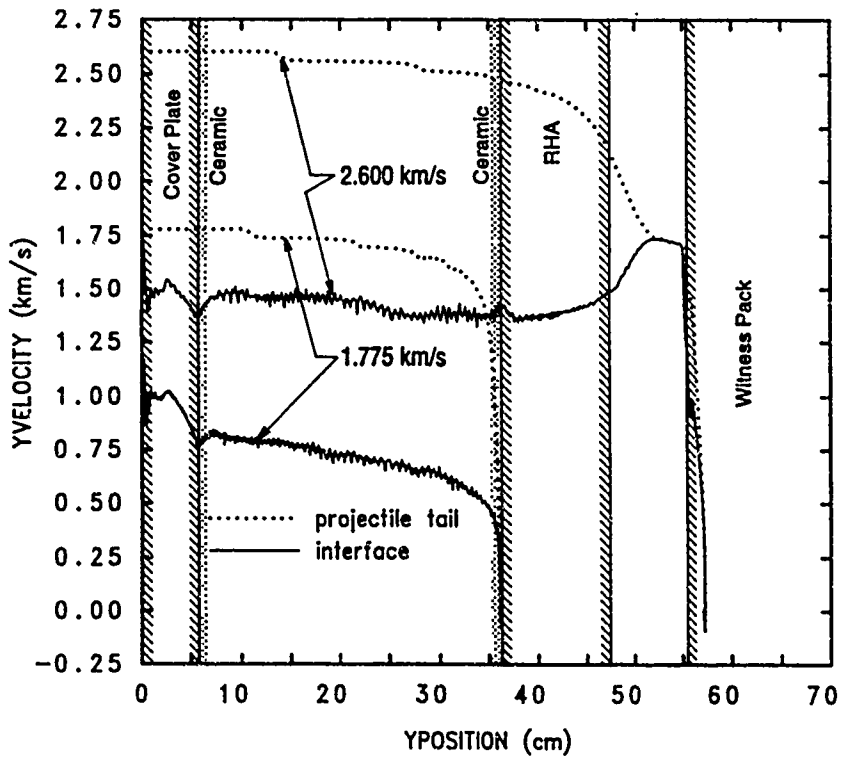


Figure 55. Penetration and tail velocities versus depth of penetration, ceramic laminate target—CTH results.

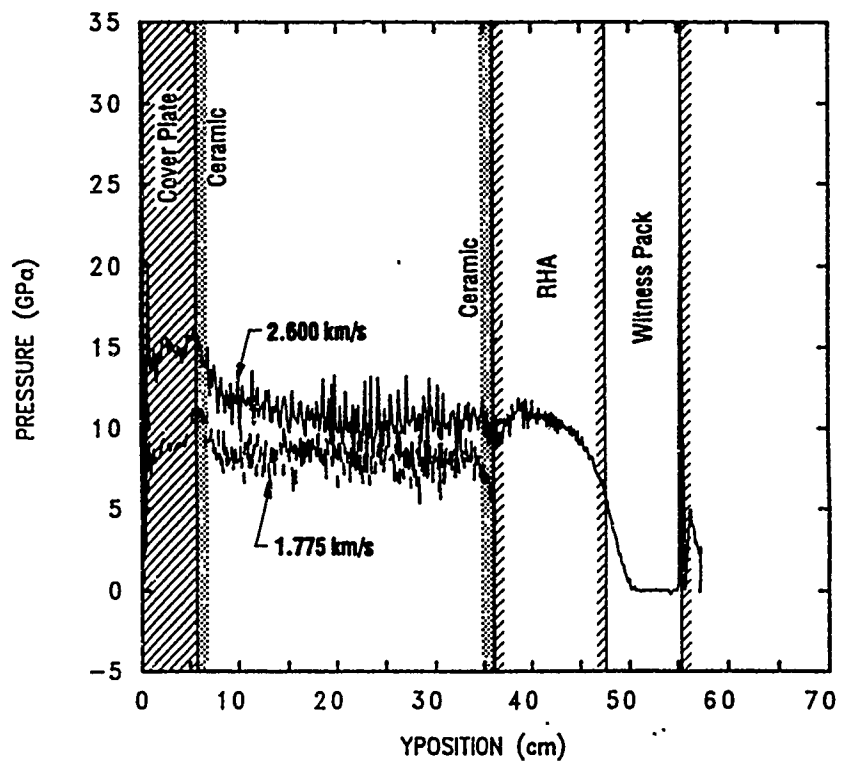


Figure 56. Pressure versus position, ceramic laminate target—CTH results.

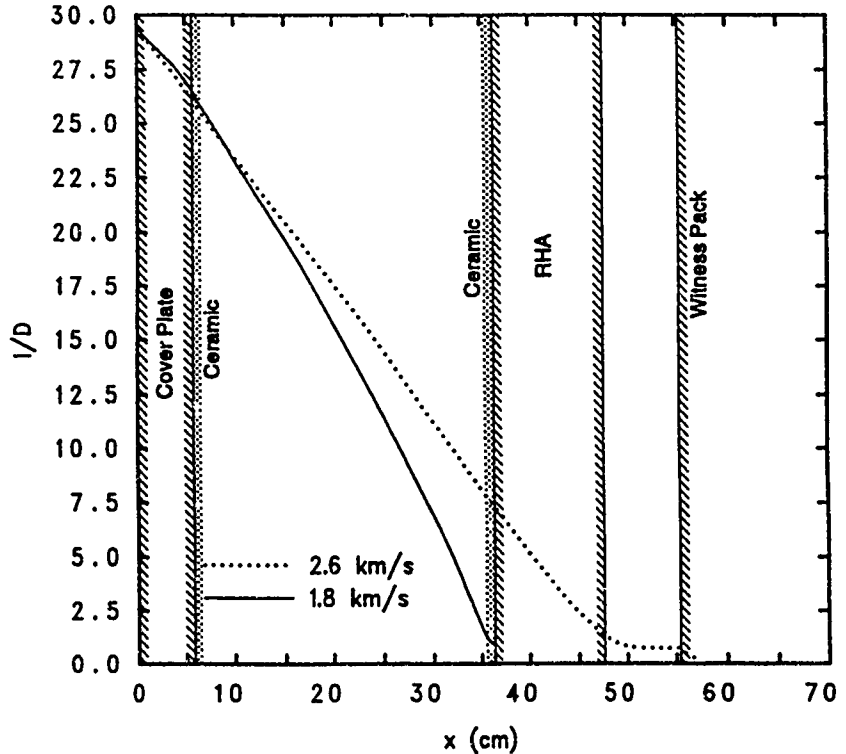


Figure 57. Normalized length of the projectiles versus depth of penetration, ceramic laminate target—CTH results.

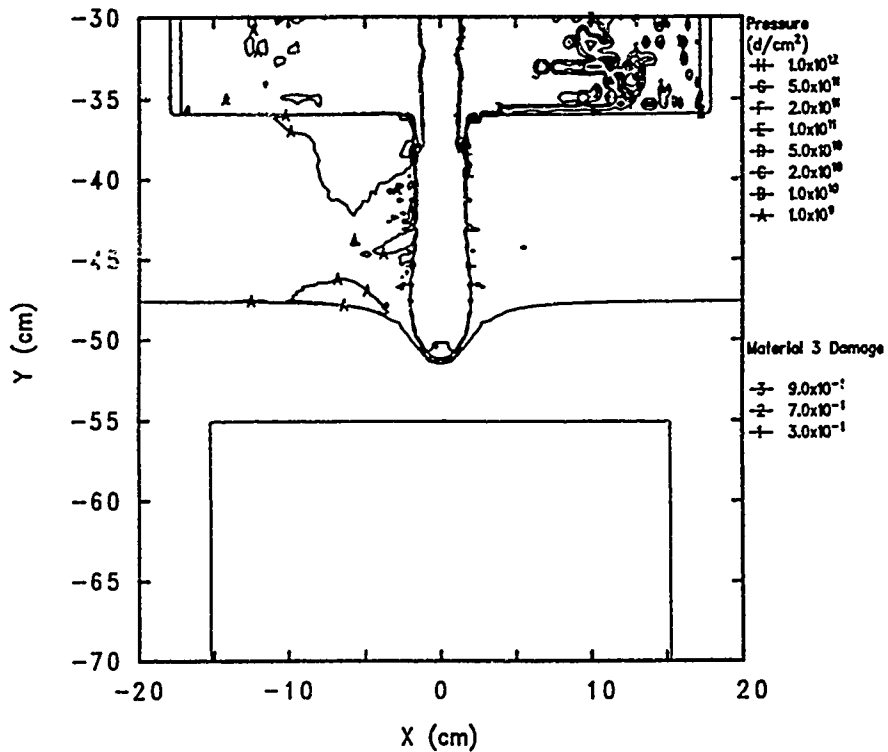


Figure 58. Material interface plot at perforation of the ceramic laminate target, $V_p = 2.600$ km/s.

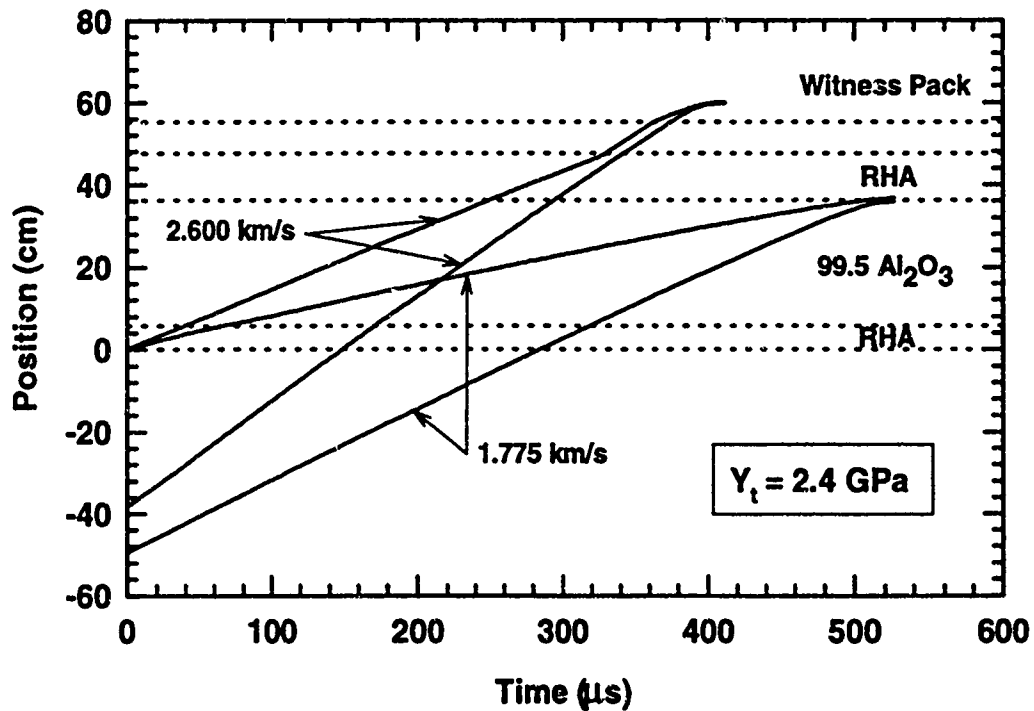


Figure 59. Nose and tail positions versus time, ceramic laminate target—Walker-Anderson results using 2.4 GPa as the effective flow stress for the ceramic.

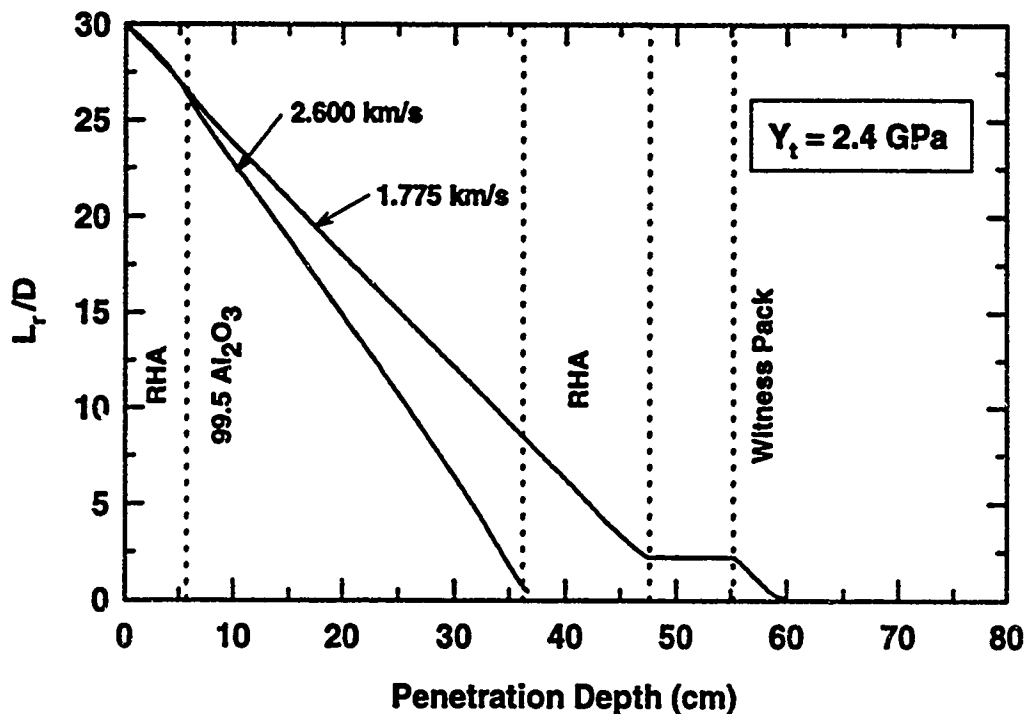


Figure 60. Normalized length of the projectiles versus depth of penetration, ceramic laminate target—Walker-Anderson results using 2.4 GPa as the effective flow stress for the ceramic.

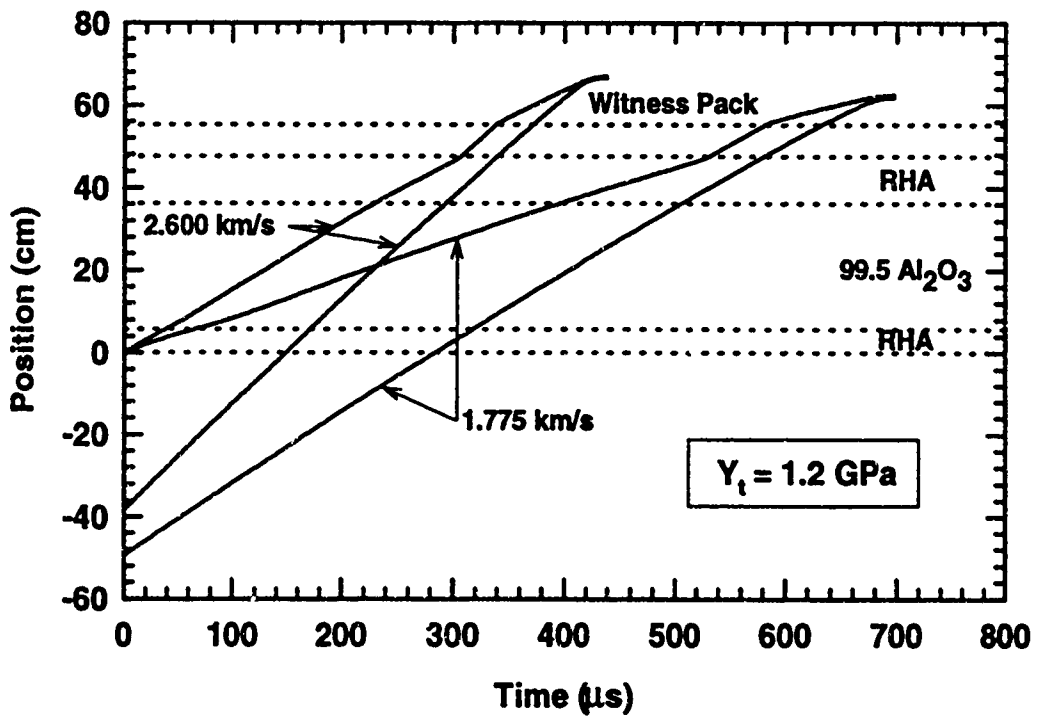


Figure 61. Nose and tail positions versus time, ceramic laminate target—Walker-Anderson results using 1.2 GPa as the effective flow stress for the ceramic.

However, comparison of the model predictions with DOP data from Woolsey, *et al.*, and position-time data taken with the PHERMEX facility at Los Alamos National Laboratory (see Section 6.3.3) indicated that the 2.4 GPa value was too "strong," and that a value of 1.2 GPa was a more appropriate value. The second case therefore used the 1.2 GPa value to represent the flow stress of the failed ceramic material for the ceramic laminate target. The resulting nose and tail positions versus time are given in Fig. 61, and the normalized projectile lengths as a function of penetration are shown in Fig. 62. The model predicts that both projectiles will perforate the ceramic laminate target and penetrate into the witness pack using this lower value for the effective stress, with the 2.600-km/s projectile penetrating slightly deeper than the 1.775-km/s projectile.

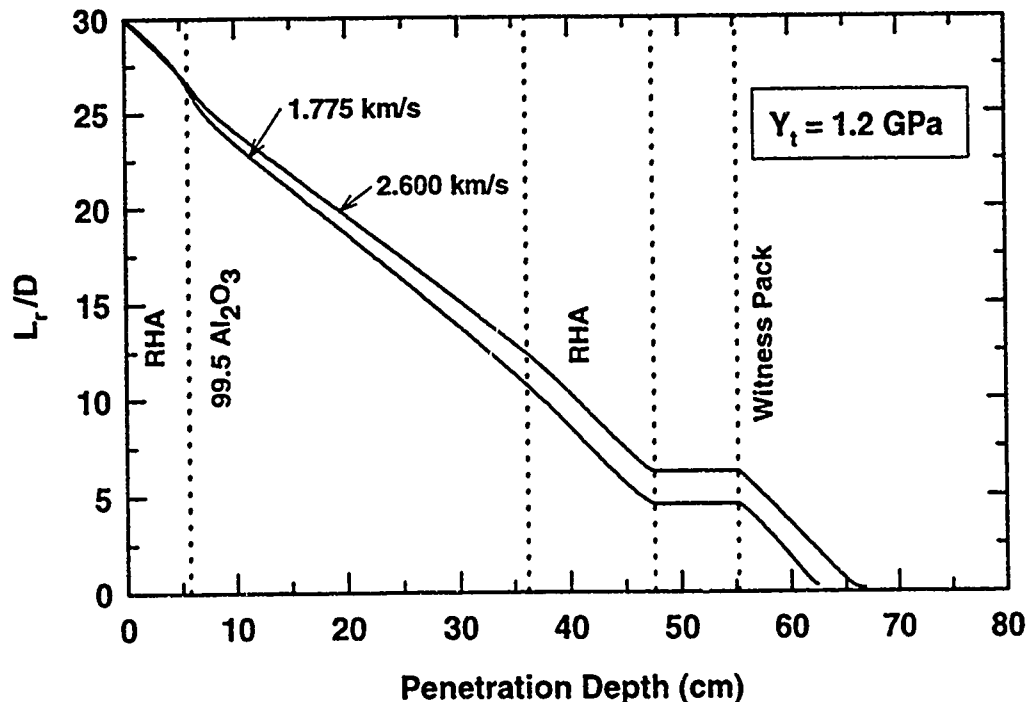


Figure 62. Normalized length of the projectiles versus depth of penetration, ceramic laminate target—Walker-Anderson results using 1.2 GPa as the effective flow stress for the ceramic.

A procedure for analyzing ceramic targets has not been developed for the MITI model. Therefore, the 2.4-GPa value, similar to the Walker-Anderson model, was used to represent an effective flow stress for the failed ceramic material. This value was then input into the MITI model for the pretest predictions.

6.6 Experimental Results and Summary

The experimental and computational results are summarized in Table 10. In the experiments, the ceramic target was defeated at both impact velocities. The calibration of the Johnson-Holmquist parameters in CTH, based on DOP testing, seriously overestimated the effective strength of the ceramic. The use of a constant effective flow stress for the failed ceramic in the Walker-Anderson model closely reproduced the CTH results when 2.4 GPa was used, and it did predict perforation at both impact velocities when 1.2 GPa was used. However, in the experiments, the super-ordnance

velocity projectile penetrated deeper into the witness pack than did the hypervelocity projectile. This is opposite of the analytical model predictions. For the other two targets, both CTH and the Walker-Anderson model predicted the correct trend with impact velocity.

Table 10. Depths of Penetration into Witness Pack: Ceramic-Laminate Target

V_i (km/s)	Penetration into Witness Pack (cm)				
	Experiment	CTH	Walker-Anderson	MITI	
		2.4 GPa	1.2 GPa		
1.73	8.58				
1.77	8.20				
1.775		*	*	7.2	4.7
2.59	7.78				
2.60	7.10				
2.600		1.8	4.7	11.6	8.8

* The projectile penetrated only to the ceramic-RHA interface.

We ask the question: why were the pretest calculations inaccurate? Although the Johnson-Holmquist ceramics model is evolving, and the parameters for 99.5% Al_2O_3 were not obtained by independent experiments, there was an attempt to "calibrate" the model against independent penetration experiments. It is possible to examine the pretest predictions and draw some conclusions.

It is not totally surprising that the pretest predictions for the ceramic target were not particularly accurate since some "discrepancies" between experiments and predictions were apparent during the "calibration" mode. The calibration of the Johnson-Holmquist model, varying only one of the parameters, certainly is overly simplistic. But attempting to perform a multivariable parametric study would have resulted in an excessive number of computer runs. Further, the nature of the DOP experiments would probably have led to a non-unique set of parameters to reproduce the same experimental results. The greatest weakness in attempting to use the DOP tests to calibrate the J-H constitutive parameters was that the impact velocity was the same (approximately 1.5 km/s) for all the tests. Although the tile thickness was varied, the penetration pressure was essentially identical for all the experiments. The experimental data did not permit an evaluation of the pressure-dependent strength of the failed material. The PHERMEX tests could perhaps have been a better discriminator for the calibration of the model constants, although the impact velocity was not sufficiently different (1.6 versus 1.5 km/s), but the experimental data set was very limited. The nature of the PHERMEX experiments did not permit an accurate determination of the total depth of penetration, and so it was not recorded. Examination of the position-time response of the nose of the projectile for the CTH calculations suggests that the stress cap of the failed material might be some appropriate average of the 1.4 and 2.6 GPa.

A second problem with the "calibration" experiments concerns the total thickness of the ceramic tiles. The tiles are relatively thin for the DOP tests, i.e., the tiles had very large lateral dimensions compared to tile thickness. This was not the case for the ceramic laminate target. Although the PHERMEX tests can be classified as a "thick target" test, the data set is extremely limited.

It is well known that the flow stress of powdered (i.e., highly comminuted ceramic) materials is generally pressure dependent. It is not totally surprising that the Walker-Anderson model, which used a constant effective flow stress for the failed ceramic, was not particularly accurate. This is discussed further in the next section.

7.0 CERAMIC LAMINATE TARGET REVISITED

7.1 Further Analytical Modeling

The conflicting results for an effective flow stress that arise from the applications of different models to various data strongly suggests shortcomings in the modeling of ceramic materials. It was decided to re-analyze the derivation of the Walker-Anderson model [10-11] to determine if a more realistic constitutive treatment of ceramics could be incorporated into the model.¹² The next subsection provides a very brief overview of the Walker-Anderson model, and then the following subsections highlight the modifications made to the analytical formulation to account for the pressure-dependent flow behavior of ceramics [38].

7.1.1 Summary of Main Features of Walker-Anderson Model

The analytical approach employed in this penetration model relies primarily on the integration of the conservation of momentum equation for assumed velocity and stress distributions in the projectile and target. The velocity distribution is based on observations from two-dimensional numerical simulations of eroding penetration. The stress distribution is then calculated from the velocity flow fields. For brevity, only a condensed description of the equations in the model will be given here; a more complete description may be found in Refs. [10-11].

Two basic equations were formulated in the model that describe the time evolution of the projectile/target interface and projectile tail velocities. The first equation is derived by integration of the axisymmetric, incompressible axial momentum equation along the centerline. This relation is given by:

$$\rho_p \int_{z_p}^{z_i} \frac{\partial u_p}{\partial t} dz + \rho_i \int_{z_p}^{z_i} \frac{\partial u_i}{\partial t} dz + \frac{1}{2} \rho_i u_z^2 \Big|_{z_p}^{z_i} + \frac{1}{2} \rho_i u_z^2 \Big|_{z_p}^{z_i} - 2 \int_{z_p}^{z_i} \frac{\partial \sigma_{xz}}{\partial x} dz = 0, \quad (21)$$

where u is the velocity, ρ is the density, σ_{xz} is the shear stress, x is the radial coordinate, z is the axial coordinate, and t is time. The subscripts p , i , and t refer to the projectile, interface, and target, respectively. The second equation accounts for deceleration of the projectile tail by elastic waves, and is given by:

$$\dot{v} = -\frac{\sigma_p}{\rho_p(L-s)} \left[1 + \frac{v-u}{s} + \frac{s}{c} \right], \quad (22)$$

where v , σ_p , c , L , and s are the projectile tail velocity, yield strength, elastic wave speed, length, and axial width of the plastic zone, respectively, and u is the interface velocity.

Equation (21) can be solved together with Eqn. (22) to determine u and v if velocity and stress distributions along the centerline are assumed for the target and projectile. The distributions employed were motivated by observations from the results of numerical simulations. The velocity profile in the projectile was specified to be:

12 The work described in this section was initiated after the comparison of the pretest predictions with the experimental results. The motivation of the work was to investigate whether the Walker-Anderson model, by using of a more realistic constitutive model for the failed ceramic, could provide better agreement with the PHERMEX data than the heuristic "matching" of the data that was described in Section 6.3.3.

$$u_z = \begin{cases} u - \frac{v-u}{s}(z-z_i) & (z_i-s) \leq z \leq z_i, \\ v & z_p \leq z \leq (z_i-s) \end{cases}, \quad (23)$$

and in the target:

$$u_z = \begin{cases} \frac{u}{\alpha^2-1} \left[\left(\frac{\alpha R}{r} \right)^2 - 1 \right] & R \leq z \leq \alpha R, \\ 0 & \alpha R \leq z \end{cases}, \quad (24)$$

where R is the crater radius and α is the ratio of the plastic zone radius to the crater radius. The coordinate r is the radius of a spherical region that extends into the target from the projectile/target interface; r is related to z by $r = z - z_i + R$. At the edge of the plastic zone $r = \alpha R$ and $z = z_i + (\alpha - 1)R$. The target material was considered to be perfectly plastic, which allowed the shear stress in the target to be calculated. The contribution to Eqn. (21) from the shear stress in the projectile was assumed negligible. Then, with the use of Eqs. (23) and (24), Eqn. (21) yields:

$$\begin{aligned} \rho_p \dot{v}(L-s) + \dot{u} \left[\rho_p s + \rho_i \frac{R(\alpha-1)}{\alpha+1} \right] + \frac{\rho_p \alpha s^2}{(\alpha^2-1)R} \left(\dot{u} \alpha - \frac{2u \dot{\alpha}}{\alpha^2-1} \right) + \frac{2\rho_i u \dot{\alpha} R}{(\alpha+1)^2} = \\ \frac{1}{2} \rho_p (v-u)^2 - \frac{1}{2} \rho_i u^2 - \frac{7Y_i}{3} \ln \alpha, \end{aligned} \quad (25)$$

where Y_i is the flow stress in the target. Equations (22) and (25) represent first-order coupled equations governing the time evolution of u and v . The initial conditions for these equations are given by the Rankine-Hugoniot shock jump conditions.

7.1.2 Modifications of the Model for Ceramics

In the development of Eqn. (25), the target material was assumed to be perfectly plastic with a constant flow stress. This constitutive model is quite adequate for most metals, but is not suitable for ceramic materials. Experimental studies [30-31] have demonstrated that ceramic materials exhibit increased strength under confinement, but are very weak and brittle when subjected to tensile loads. Furthermore, the strength of the ceramic decreases after the material begins to crack or fail. This phenomenologically observed constitutive behavior was implemented in an approximate manner for the present model by permitting the yield stress to vary with confining pressure, so that $Y = \beta p$, where p is the pressure. This augmentation also tends to replicate the additional strength seen at early times for the intact ceramic, since the pressure is quite large during the initial stages of the penetration process.

To implement this constitutive form for the ceramic material, the last integral in Eqn. (21) was evaluated assuming the flow stress is variable. Using the velocity profiles given in Eqn. (24) and allowing for variable yield stress, this integral becomes:

$$2 \int_z^{\alpha R} \frac{d\sigma_x}{dx} dz = -\frac{7}{3} \int_R^{\alpha R} \frac{Y dr}{r}. \quad (26)$$

The pressure distribution along the centerline in the target must also be determined. This is accomplished through integration of the incompressible axisymmetric axial momentum equation from an arbitrary location inside the plastic zone to the edge of the plastic zone. Application of this procedure yields:

$$p = -\frac{2Y}{3} + \rho_i \int_r^{\alpha R} \frac{\partial u_z}{\partial t} dr - \frac{1}{2} \rho_i u_z^2 + \frac{7}{3} \int_r^{\alpha R} \frac{Y dz}{r}. \quad (27)$$

The assumed constitutive behavior in the ceramic requires $p = Y/\beta$, which when combined with Eqn. (27), gives an integral equation for Y . This integral equation was solved for Y using the condition that $p = 0$ at $r = \alpha R$. Once Y was determined, the integral in Eqn. (26) was evaluated. The algebraic details are quite cumbersome but, nevertheless, straightforward. Substitution of the result into Eqn. (21), making use of the velocity distribution given in Eqn. (24), gives the integrated form of the axial momentum equation for the ceramic:

$$\begin{aligned} \rho_p \dot{v}(L-s) + \dot{u} \left[\rho_p s + \rho_i \frac{R(\alpha-1)}{\alpha+1} \right] + \frac{\rho_p \alpha s^2}{(\alpha^2-1)R} \left(\dot{u} \alpha - \frac{2u \dot{\alpha}}{\alpha^2-1} \right) + \frac{2\rho_i u \dot{\alpha} R}{(\alpha+1)^2} = \\ \frac{1}{2} \rho_p (v-u)^2 - \frac{1}{2} \rho_i u^2 - \frac{2\rho_i \delta u}{\alpha^2-1} \left[\dot{\alpha} R \left(\frac{\delta \alpha^\delta - \alpha}{\delta-1} - 1 \right) \right. \\ \left. + \frac{u}{\alpha^2-1} \left\{ \frac{2\delta \alpha^4}{(2-\delta)(4-\delta)} + \frac{\delta \alpha^\delta}{4-\delta} - \frac{\delta \alpha^{\delta+2}}{2-\delta} - \alpha^2 + 1 \right\} \right] \\ - \frac{\rho_i \delta R}{\alpha^2-1} \left[\frac{2u \alpha \dot{\alpha}}{\alpha^2-1} - \dot{u} \right] \left[\frac{\alpha^2}{\delta-1} + \frac{1}{\delta+1} - \frac{2\delta \alpha^{\delta+1}}{\delta^2-1} \right]. \end{aligned} \quad (28)$$

where $\delta = 7\beta/(3+2\beta)$. When solved together with Eqn. (22), Eqn. (28) yields the time evolution for the velocities u and v .

7.1.3 Determination of α

A critical part of the analysis is the determination of α . The calculation of α is nontrivial, and is intimately coupled with the constitutive model assumed for the target. A recent study employed cavity expansion theory [39] to determine α for materials with a yield strength that varied with pressure. Furthermore, the yield strength of the intact material was assumed to be $Y = Y_0 + \beta_0 p$, where Y_0 is the yield strength of intact material at zero pressure, and β_0 is the slope of the intact yield strength/pressure curve. After steady-state, one-dimensional flow was assumed, an expression for α was derived:

$$\alpha = \left[\frac{2\sqrt{3}G}{2Y_0 + f\beta_0 \rho_i u^2} \right]^{1/2}, \quad (29)$$

where G is the shear modulus. The factor f accounts approximately for the decrease in u across the plastic zone, since it was assumed to be constant in the derivation of Eqn. (29). In the present study f was set to 0.5.

Further complicating the calculation of α is the fact that during the initial stages of penetration the flow is unsteady. Initial values for α should be quite small when compared to steady-state values. In the present study, it was assumed that the edge of the plastic zone is coincident with the shock front at early times; α was set to $(u_s/u)^q$, where u_s is the initial shock velocity. The constant q was adjusted so that the initial pressure in the calculation matched the Hugoniot impact pressure. This initial value was then linearly interpolated to the steady-state value given by Eqn. (29).

It is evident that the shortcomings in the calculation for α are numerous, and is clearly an area where further work is required. Nevertheless, in spite of the obvious deficiencies in this part of the model, the analytical predictions presented in the next section show considerable promise.

7.2 Parametric Studies with Ceramic Model

The modifications made to the Walker-Anderson model are believed to be more representative of the strength behavior in a granular or crushed material. However, the new model still needed to be calibrated because the slope of the flow stress-pressure curve, given by β , is required. The remaining physical properties for the ceramic target material are essentially fixed or were specified (p_0 , G , Y_0 , and β_0); the physical properties of the projectile remained unchanged. Woolsey's experiments and the PHERMEX experiments were again used for calibration purposes.

The model was first compared to results from Woolsey's experiments for 99.5 Al_2O_3 ceramic tiles. The experimental DOP setup was shown previously in Fig. 45. The projectile nose and tail positions as a function of time for two values of β , 0.75 and 1.0, are shown in Fig. 63. The ceramic tile thickness was 3.0 cm. From the results it is apparent that for this tile thickness, $\beta = 1.0$ provides slightly better agreement with the experimental depth of penetration.

However, when the model was compared to the position-time data from the PHERMEX experiments, where much thicker tiles were used, the results indicated that a value of $\beta = 1.0$ was probably too large for thick ceramics. β was varied parametrically and the results compared with the data from the PHERMEX experiments. The projectile nose and tail positions are shown for $\beta = 0.55$, 0.75, and 0.95 in Fig. 64. The experimentally measured positions are also shown on the figure. Although $\beta = 0.95$ provides good agreement to the experiment at early times, the late time agreement is unsatisfactory. The best overall agreement is obtained for $\beta = 0.75$. This value of β was tried for the analytical predictions of the ceramic laminate target experiments.

7.3 Analytical Predictions

Results from the analytic model were compared and contrasted with the experimental data. Shown in Fig. 65 are analytical predictions for projectile tail and interface positions as a function of time for the 1.775-km/s impact using two different values of the pressure-yield slope β , 0.75 and 0.50. Results for the 2.600-km/s impact are shown in Fig. 66 for the same two values of β . Using a value of $\beta = 0.75$, the hypervelocity projectile failed to emerge from the ceramic target (the projectile penetrated to a position close to the rear surface of the target), but at 1.775 km/s the projectile penetrated 6.3 cm into the witness pack. This is in contrast to the results presented in Fig. 59, where the hypervelocity projectile penetrated the target, but the super-ordnance velocity projectile did not. This change in the results is a direct consequence of the pressure-dependent yield

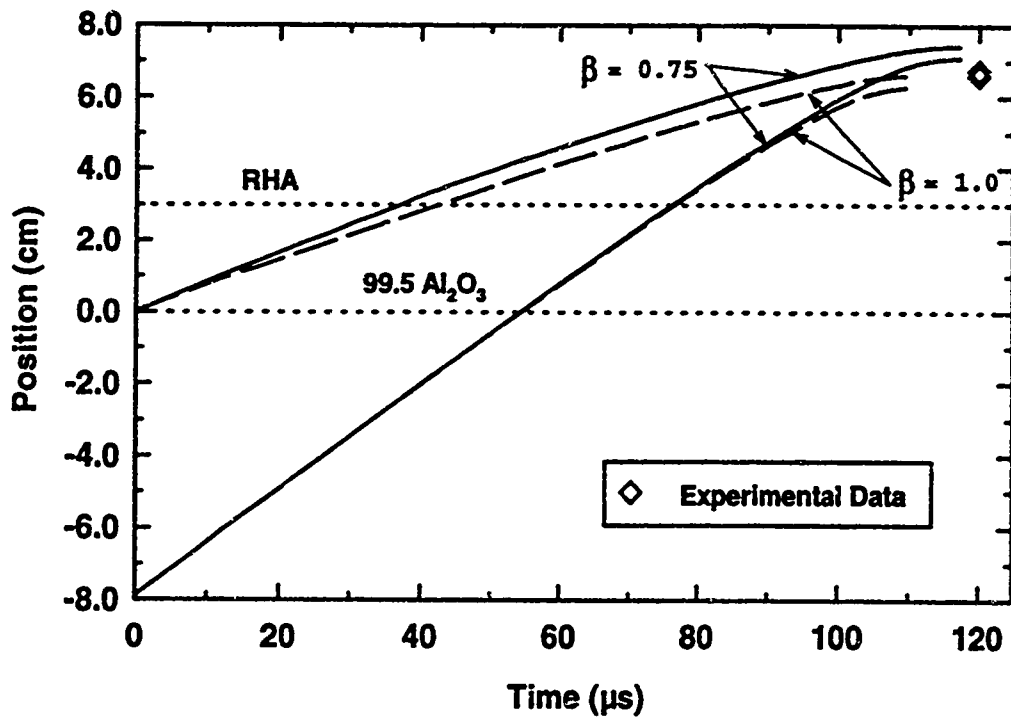


Figure 63. Nose and tail positions versus time and comparison of the final depth of penetration with DOP tests for a 3.0-cm thick, 99.5 Al_2O_3 tile using the pressure-dependent yield function in the Walker-Anderson model.

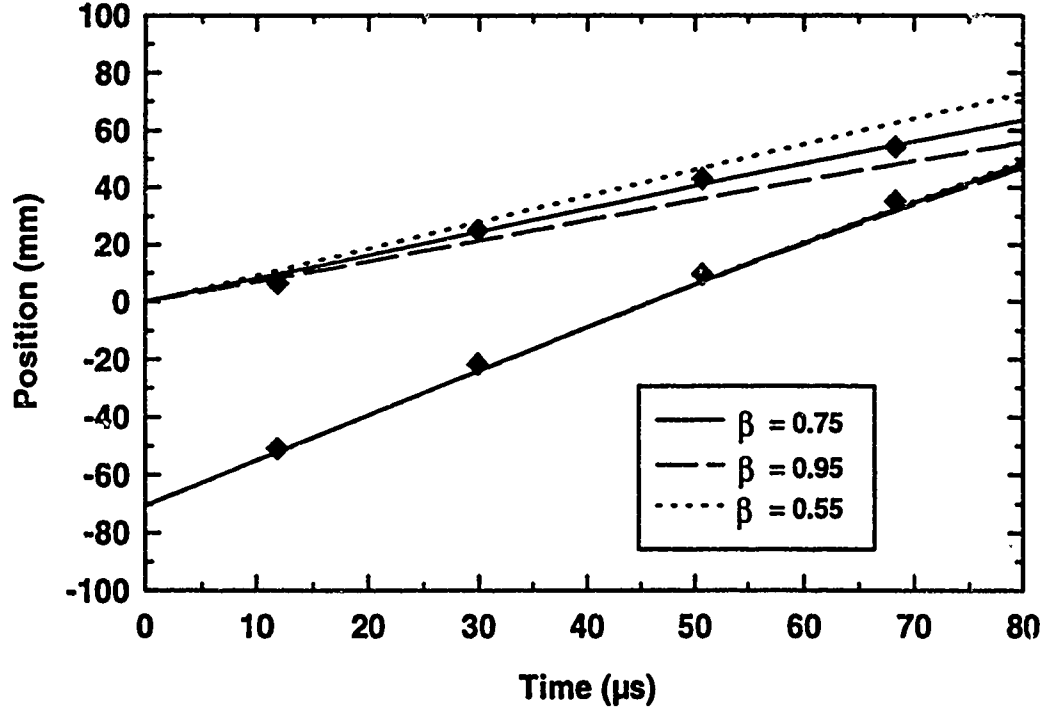


Figure 64. Comparison of the Walker-Anderson model using the pressure-dependent yield function to PHERMEX data for a 99.5 Al_2O_3 ceramic target.

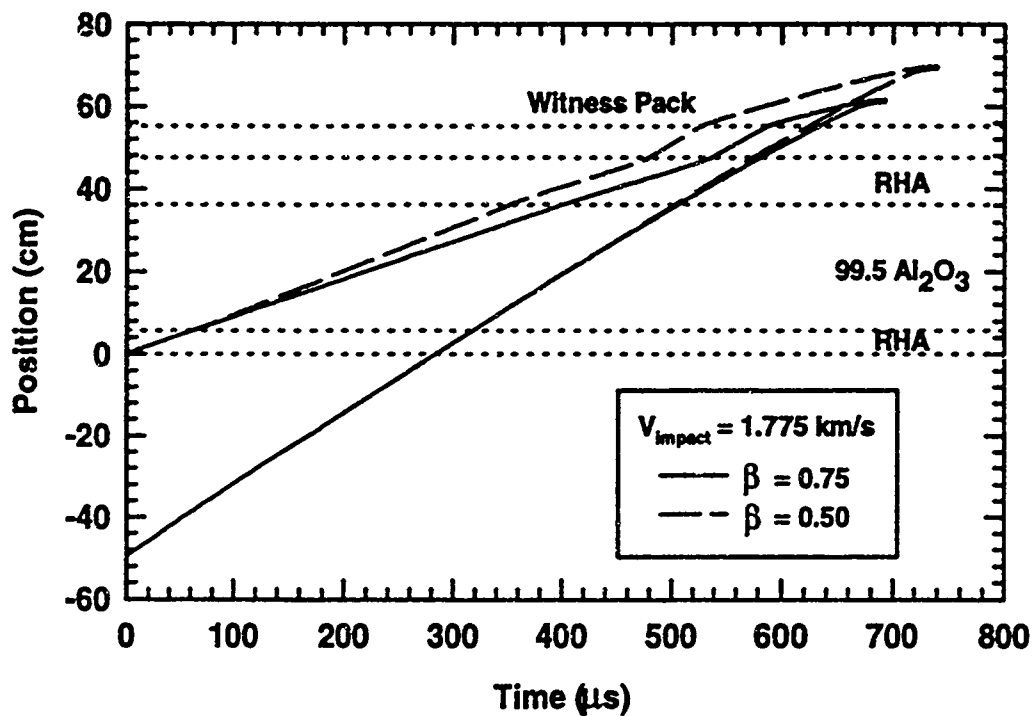


Figure 65. Nose and tail positions versus time for $V_p = 1.775 \text{ km/s}$, ceramic laminate target—Walker-Anderson model using the pressure-dependent yield function.

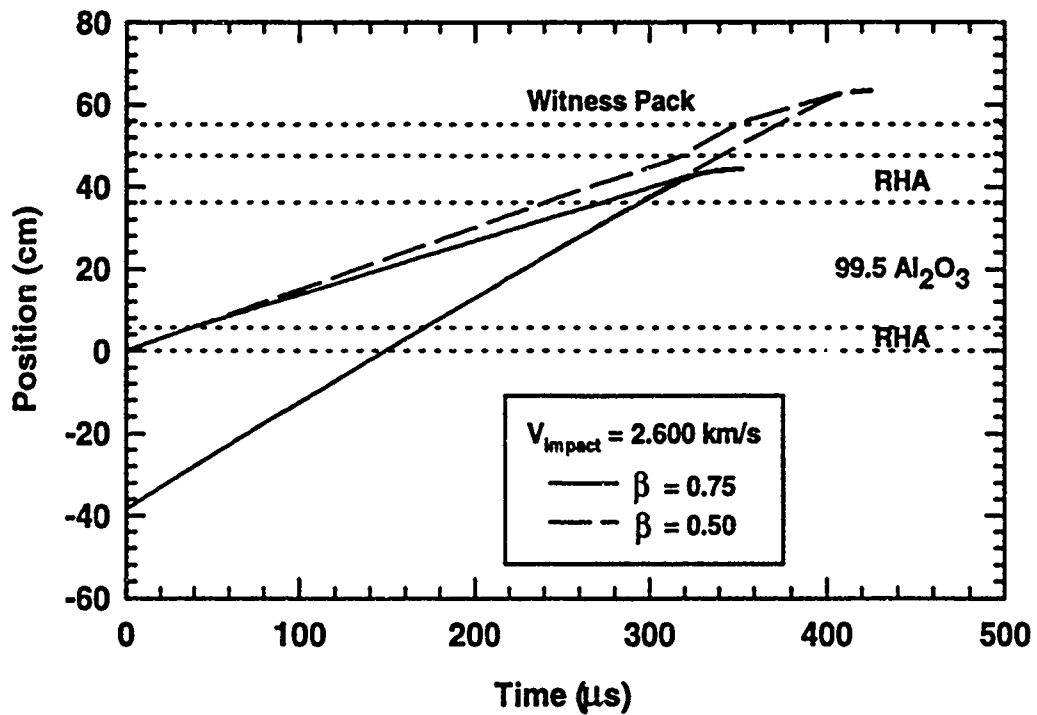


Figure 66. Nose and tail positions versus time for $V_p = 2.600 \text{ km/s}$, ceramic laminate target—Walker-Anderson model using the pressure-dependent yield function.

function since the failed ceramic material has a higher effective flow stress at higher impact velocities because the penetration pressure is correspondingly higher. Using $\beta = 0.5$, i.e., decreasing the "influence" of pressure, the target was defeated at both impact velocities.

7.4 Experimental Results and Summary

The experimental and analytical results are summarized in Table 11. As was previously stated, the projectile defeated the target at both impact velocities in the experiments. Agreement between the model and experiments for the 1.775 km/s projectile is quite satisfactory when $\beta = 0.75$ is used. However, at 2.600 km/s, this value of β seems inappropriate since the model predicted no perforation of ceramic target would occur. Thus it seems that the strength of ceramic in the model is too large to provide the correct result for the hypervelocity projectile. When β was set to 0.50, agreement with the hypervelocity experiment was satisfactory, but the super-ordnance velocity experiment was overpredicted. A possible resolution of this dichotomy is discussed in the next paragraph.

Table 11. Depths of Penetration into Witness Pack: Ceramic Laminate Target Revisited

V_i (km/s)	Penetration into Witness Pack (cm)			
	Experiment	Walker-Anderson 2.4 GPa	Walker-Anderson 1.2 GPa	Modified Walker-Anderson $\beta = 0.75$
1.73	8.58			
1.77	8.20			
1.775		*	7.2	6.3
2.59	7.78			
2.60	7.10			
2.600		4.7	11.6	**
				14.5
				8.2

* The projectile penetrated to the ceramic-RHA interface.

** The projectile did not quite perforate the RHA back plate.

Some interesting conclusions can be identified from the results presented above. First, it is not surprising that the analytic results agree better with the lower velocity experiments, since calibration of the model was also based on results from lower velocity (1.5 and 1.6 km/s) experiments. Second, results from the high velocity predictions seem to indicate that perhaps a cap exists for the pressure-yield surface. This is not unexpected since brittle materials after failure often tend to approach a limiting compressive flow stress independent of confining pressure (this is the behavior for the failed ceramic in the Johnson-Holmquist model, but was not included in the analytical ceramics model). Finally, it is particularly satisfying that the analytic model was able to reproduce the trend indicating that the super-ordnance velocity projectile should penetrate the witness pack more than the hypervelocity projectile. This was not observed in any of the other analytical or numerical predictions.

8.0 SUMMARY AND CONCLUSIONS

The results from pretest predictions for penetration experiments of tungsten alloy projectiles into three generic target types have been documented. Predictions were made using two analytical models (the Walker-Anderson model and the MITI model) and with numerical simulation (using the wave propagation computer code CTH). The targets—a finite-thick RHA target; oblique, high-hard steel, spaced-plate target; and a ceramic laminate target—were purposely designed to be defeated, and penetration of the residual projectile into an RHA witness pack was designated as the metric for comparison. The purpose of this study can be regarded as twofold. First, a pretest prediction of any experiment is always desirable. For these targets, the predictions provide an estimate of the residual projectile length and velocity, as well as the resulting penetration of the residual rod into an RHA witness pack. Furthermore, specific details of the experiment can more readily be analyzed with modeling; for example, some quantities cannot easily be measured in an experiment, such as penetration velocity or projectile erosion rate. Second, a subsequent comparison of these predictions to the actual experimental outcomes provides a quantitative measure of the state-of-the-art predictive capability for these generic target types using hydrocodes and analytical models. Analysis of discrepancies then suggests the most prudent areas for improvement in both the analytical and numerical models.

Agreement between the analytical and numerical predictions with the experimental depth of penetration into the witness pack for the finite-thickness RHA target was exceptional (within a millimeter of penetration). This was not completely unexpected since the analytical models were developed for long-rod penetration into semi-infinite armor steels, and semi-infinite penetration has been studied fairly extensively with CTH. The model predictions, however, did not agree with the specific details of the experiment as well. Analytical predictions for the length and velocity of the residual projectile did not fall within the experimental scatter, particularly for the low velocity projectile. There was a tendency for the models to overpredict the residual velocity and underpredict the residual length of the projectile, particularly for the super-ordnance velocity impact case. These represent compensating errors in the impact against the witness pack. Possible sources of error suggested for these variations included an inadequate treatment of breakout effects for the target, and improper constitutive properties for the projectile. However, regardless of the sources of errors, the results indicate a need for improvements in modeling of perforation physics of steel targets, even though the materials in this target were the best understood of the three target types considered.

Predictions for an array of spaced, oblique, high-hard steel armor plates were also made using the two analytical models and CTH. The pretest calculations overpredicted the depths of penetration into the witness pack, although, in general, the computations and the analytical models predicted the correct ordering of the penetration, i.e., the super-ordnance velocity projectile penetrated deeper into the witness pack than the hypervelocity projectile. Although a certain amount of this discrepancy might be attributed to projectile pitch and yaw in the experiment, which was not modeled in the predictions, the largest single source of error is probably an accumulation of the errors resulting from inadequate breakout modeling for the plates; the same source of the error identified for the finite-thickness RHA target. In CTH, material failure is currently treated using a simple tensile failure model that can allow unrealistic large strains to accrue before material separation. Similarly,

the breakout modeling of the Walker-Anderson and MITI models are overly simplistic. This problem illustrates the need for improvement in breakout mechanics of both the numerical and analytical models.

Predictions for the ceramic target were made using both analytical models and CTH. In the experiments, the ceramic target was defeated at both impact velocities. In the numerical simulations, however, the projectile did not perforate the target at the super-ordnance velocity. Apparently, the calibration of the Johnson-Holmquist parameters, based on DOP testing, considerably overestimated the effective strength of the ceramic. In the analytical predictions, the use of a constant effective flow stress for the failed ceramic closely reproduced the CTH results when 2.4 GPa was used, and it did predict perforation at both impact velocities when 1.2 GPa was used. However, in the experiments, the super-ordnance velocity impact penetrated deeper into the witness pack than did the hypervelocity impact. This is opposite of the analytical model predictions. In a separate result, the analytical model was improved by adding a pressure dependence to the flow stress in the target. The analytical model was able to reproduce the trend indicating that the super-ordnance velocity projectile should penetrate the witness pack more than the hypervelocity projectile. This was not observed in any of the other analytical or numerical predictions. However, the slope of the pressure-flow stress function had to be varied with impact velocity to replicate the experimental results accurately. These results demonstrate the need for improved constitutive models in ceramic materials, for use both in numerical simulations and analytical predictions. A fundamental understanding of the dynamic penetration behavior of ceramic materials will be necessary before an adequate predictive capability can be attained.

Lastly, one of the objectives and motivations for the pretest predictions was to perform an assessment of how accurately the targets could be analyzed. The analysis of RHA targets was extremely accurate using the analytical models or CTH. More work needs to be performed in perforation physics and ceramics constitutive modeling before either CTH or analytical models can predict the response of these target types with the fidelity of the RHA target predictions. It has also been shown that the computational resources required to perform an analysis of an oblique, spaced-plate target are simply too great to permit parametric studies at the present time. A better ability to model perforation is required so that analytical models can be applied accurately to spaced targets.

With the validation demonstrated here, mass-velocity trade-off calculations, to include assessments of the performance of advanced penetrator concepts, can be made using CTH for RHA targets. Although the analytical models could also be used, many of the advanced penetrator concepts have more complicated geometries, particularly in cross-section, than simple cylindrical rods. The analytical models are incapable of assessing differences in performance due to changes in geometric design (aside from simple length or diameter effects).

9.0 ACKNOWLEDGEMENTS

The authors thank John P. Riegel, III, for performing the pretest predictions using the MITI model. This work was performed under contract DAAL03-92-K-0001, administered by the U. S. Army Research Office. The authors would like to thank Dr. Stephan J. Bless and Dr. Thomas M. Kiehne for their support and encouragement during the conduct of this study. The three-dimensional computations were performed on the CRAY 2 at the U. S. Army Tank and Automotive Command, and we sincerely thank Dr. Jim Thompson at TACOM for his assistance and support in providing access to the CRAY 2. The authors also would like to thank Ms. Janet Banda for her assistance in preparing this report.

10.0 REFERENCES

1. B. R. Sorensen, K. D. Kimsey, G. F. Silsby, D. R. Scheffler, T. M. Sherrick, and W. S. deRosset, "High Velocity Penetration of Steel Targets," *Int. J. Impact Engng.*, 11(1), pp. 107-119 (1990).
2. S. Bless, R. Subramanian, and T. Kiehne, "Performance of L/D = 30 Tungsten Rods Against RHA at 1.8 and 2.6 km/s," Report No. IAT.R.0026A, Institute for Advanced Technology, The University of Texas at Austin, April (1994).
3. S. Bless, R. Subramanian, and T. Kiehne, "Performance of L/D = 30 Tungsten Rods Against Spaced Plate, Ceramic, and Reactive Armor at 1.8 and 2.6 km/s," Report No. IAT.R.0032, Institute for Advanced Technology, The University of Texas at Austin, May (1994).
4. J. M. McGlaun, S. L. Thompson, and M. G. Elrick, "CTH: A Three-Dimensional Shock Wave Physics Code," *Int. J. Impact Engng.*, 10 (1-4), 351-360 (1990).
5. W. W. Predebon, C. E. Anderson, Jr., and J. D. Walker, "Inclusion of Evolutionary Damage Measures in Eulerian Wavecodes," *Comput. Mech.*, 7(4), 221-236 (1991).
6. S. Silling, "Stability and Accuracy of Differencing Methods for Viscoplastic Models in Wavecodes," *J. Comp. Phys.*, 104, 30-40 (1993).
7. G. R. Johnson and W. H. Cook, "Fracture Characteristics of Three Metals Subjected to Various Strains, Strain Rates, Temperatures, and Pressures," *Engng. Fracture Mech.*, 21(1), 31-48 (1985).
8. G. R. Johnson and T. J. Holmquist, "A Computational Constitutive Model for Brittle Materials Subjected to Large Strains, High Strain Rates, and High Pressures," *Shock Waves and High-Strain Rate Phenomena in Materials*, pp. 1075-1081, M. A. Meyers, L. E. Murr, and K. P. Staudhammer (eds), Marcel Dekker, NY (1992).
9. D. Yaziv, P. A. Cox, and J. P. Riegel, III, "Modified Integral Theory of Impact to Model Long Rod Penetration at Normal and Oblique Incidence," *Shock Compression of Condensed Matter—1991*, S. C. Schmidt, R. D. Dick, J. W. Forbes, and D. G. Tasker (eds), Elsevier, 963-966 (1992).
10. J. D. Walker and C. E. Anderson, Jr., "A Nonsteady-State Model for Penetration," *Proc. 13th Int. Symp. on Ballistics*, Vol. 3, 9-16 (1992).
11. J. D. Walker and C. E. Anderson, Jr., "A Time-Dependent Model for Long-Rod Penetration," *Int. J. Impact Engng.*, accepted for publication (1994).
12. C. E. Anderson, Jr. and J. D. Walker, "An Examination of Long-Rod Penetration," *Int. J. Impact Engng.*, 11(4), pp. 481-501 (1991).
13. C. E. Anderson, Jr., S. A. Mullin, and C. J. Kuhlman, "Computer Simulations of Strain-Rate Effects in Replica Scale Model Penetration Experiments," *Int. J. Impact Engng.*, 13(1), 35-52 (1993).
14. V. Hohler and A. J. Stilp, "Long Rod Penetration Mechanics," in *High Velocity Impact Dynamics*, Chapter 5, J. A. Zukas (ed), John Wiley & Sons, 321-404 (1990).

15. V. Hohler and A. J. Stilp, in *A Penetration Mechanics Database*, by C. E. Anderson, Jr., B. L. Morris, and D. L. Littlefield, SwRI Report 3593/001, prepared for DARPA, Southwest Research Institute, San Antonio, TX (1992).
16. C. E. Anderson, Jr., J. D. Walker, and G. E. Hauer, "Target Resistance for Long-Rod Penetration into Semi-Infinite Targets," *Nucl. Engng. And Design*, 138, 93-104 (1992).
17. C. E. Anderson, Jr., D. L. Littlefield, and J. D. Walker, "Long-Rod Penetration, Target Resistance, and Hypervelocity Impact," *Int. J. Impact Engng.*, 14(1-4), 1-12 (1993).
18. M. J. Forrestal and V. K. Luk, "Dynamic Spherical Cavity-Expansion in a Compressible Elastic-Plastic Solid," *J. Appl. Mech.*, 55, 275-279 (1988).
19. M. J. Forrestal, V. K. Luk, and N. S. Brar, "Perforation of Aluminum Armor Plates with Conical-Nose Projectiles," *Mechanics of Materials*, 10, 97-105 (1990).
20. M. J. Forrestal, N. S. Brar, and V. K. Luk, "Penetration of Strain-Hardening Targets with Rigid Spherical-Nose Rods," *J. Appl. Mech.*, 58, 7-10 (1991).
21. A. Tate, "A Theory for the Deceleration of Long Rods after Impact," *J. Mech. Phys. Solids*, 15, 387-399 (1967).
22. C. E. Anderson, Jr., J. D. Walker, S. J. Bless, and Y. Partom, "On the L/D Effect for Long-Rod Penetrators," submitted for publication (1994).
23. C. E. Anderson, Jr., J. Lankford, S. A. Royal, and J. P. Riegel, III, "Large Aspect Ratio Penetration and Erosion Phenomenology," submitted for publication (1993).
24. V. Hohler and A. Stilp, "Hypervelocity Impact of Projectiles with L/D from 1 to 32," *Int. J. Impact Engng.*, 5(1-4), 323-331 (1987).
25. D. R. Christman and J. W. Gehring, "Analysis of High-Velocity Projectile Penetration Mechanics," *J. Appl. Phys.*, 37(4), 1579-1587 (1966).
26. P. H. Deitz and A. Ozolins, "Computer Simulations of the Abrams Live-Fire Field Testing," BRL-MR-3755, U. S. Army Ballistic Research Laboratory, Aberdeen Proving Ground, MD, May (1989).
27. C. E. Anderson, Jr., D. L. Littlefield, S. J. Bless, and R. Subramanian, "The Penetration Performance of Short L/D Projectiles," *Joint AIRAPT/APS Conference on High Pressure Science and Technology*, Colorado Springs, CO, June 28-July 2 (1993).
28. C. E. Anderson, Jr., B. L. Morris, and D. L. Littlefield, *A Penetration Mechanics Database*, SwRI Report 3593/001, Southwest Research Institute, San Antonio, TX (1992) (AD No: A246351)
29. W. Herrmann and J. S. Wilbeck, "Review of Hypervelocity Penetration Theories," *Int. J. Impact Engng.*, 5(1-4), 307-322 (1987).
30. G. R. Johnson, R. A. Stryk, O. A. Souka, T. J. Holmquist, J. Lankford, C. E. Anderson, and J. Walker, "EPIC-3 Improvements and Ceramic Model Development," (Revision 1) Report MBAL40, Honeywell, Inc., Brooklyn Park, MN, February (1990).

31. G. R. Johnson, T. J. Holmquist, J. Lankford, C. E. Anderson, and J. Walker, "A Computational Constitutive Model and Test Data for Ceramics Subjected to Large Strains, High Strain Rates, and High Pressures," Report MDAL09, Honeywell, Inc., Brooklyn Park, MN, August (1990).
32. G. R. Johnson and T. J. Holmquist, "Development and Evaluation of Computational Constitutive Models," Report H36099, Alliant Techsystems, Inc., Hopkins, MN, January (1993).
33. J. D. Walker and C. E. Anderson, Jr., "Implementation of the Johnson-Holmquist Ceramics Model into CTH," SwRI Report 4522/109, Southwest Research Institute, San Antonio, TX, January (1992).
34. P. Woolsey, S. Mariano, and D. Kokidko, "Alternative Test Methodology for Ballistic Performance Ranking of Armor Ceramics," *Fifth Annual TACOM Armor Coordinating Conference*, Naval Postgraduate School, Monterey, CA, March (1989).
35. P. Woolsey, D. Kokidko, and S. Mariano, "Progress Report on Ballistic Test Methodology for Armor Ceramics," *TACOM Combat Vehicle Survivability Symposium*, Gaithersburg, MD, March (1990).
36. P. Woolsey, "Residual Penetration Ballistic Testing of Armor Ceramics," *Combat Vehicle Survivability Symposium*, Gaithersburg, MD, April (1991).
37. S. R. Skaggs, private communication, 1992.
38. D. L. Littlefield, C. E. Anderson, Jr., and S. R. Skaggs, "Analysis of penetration of steel and Al_2O_3 targets," *Joint ARIAPT/APS Conference on High Pressure Science and Technology*, Colorado Springs, CO, June 28-July 2 (1993).
39. Y. Partom, "Ceramic Armor Resistance to Long-Rod Penetration (R_p) and its Dependence on Projectile Velocity," Report No. IAT.R.0017, Institute for Advanced Technology, The University of Texas at Austin, March (1993).

